T.C.
DOKUZ EYLÜL ÜNİVERSİTESİ
İZMİR ULUSLARARASI
BİYOTIP VE GENOM
ENSTİTÜSÜ

IDENTIFICATION AND FUNCTIONAL CHARACTERIZATION OF ESSENTIAL GENES INVOLVED IN THE DEVELOPMENT OF MALIGNANT PLEURAL MESOTHELIOMA USING CRISPR/CAS9-BASED NEGATIVE SELECTION SCREENING

ECE ÇAKIROĞLU

MOLECULAR BIOLOGY AND GENETICS

PHD THESIS

İZMİR-2023

Thesis Code: DEU.HSI.PhD-2016850041

T.C.
DOKUZ EYLÜL ÜNİVERSİTESİ
İZMİR ULUSLARARASI BİYOTIP VE
GENOM ENSTİTÜSÜ

IDENTIFICATION AND FUNCTIONAL CHARACTERIZATION OF ESSENTIAL GENES INVOLVED IN THE DEVELOPMENT OF MALIGNANT PLEURAL MESOTHELIOMA USING CRISPR/CAS9-BASED NEGATIVE SELECTION SCREENING

MOLECULAR BIOLOGY AND GENETICS

PHD THESIS

ECE ÇAKIROĞLU

Advisor: Assoc. Prof. Dr. Şerif Şentürk

(This thesis was supported by The Scientific and Technological Research Council of Turkey (TUBITAK) with grant number 117Z227)

Thesis Code: DEU.HSI.PhD-2016850041

T.C.
DOKUZ EYLÜL ÜNİVERSİTESİ

İZMİR ULUSLARARASI BİYOTIP VE GENOM ENSTİTÜSÜ

DOKTORA TEZ SAVUNMA SINAVI TUTANAĞI

Dokuz Eylül Üniversitesi İzmir Uluslararası Biyotıp ve Genom Enstitüsü, Genom Bilimleri ve Moleküler Biyoteknoloji Anabilim Dalı, Moleküler Biyoloji ve Genetik Doktora Programı 2016850041 numaralı öğrencisi Ece Çakıroğlu, "Identification and Functional Characterization of Essential Genes Involved in the Development of Malignant Pleural Mesothelioma Using CRISPR/Cas9-Based Negative Selection Screening" konulu Doktora tezini 26.01.2023 tarihinde yapılan savunma sınavı sonucunda başarılı/[redacted] olmuştur.

BAŞKAN
Doç. Dr. Serif Şentürk

JÜRİ ÜYESİ
Dr. Öğr. Üyesi Yavuz Oktay

JÜRİ ÜYESİ
Doç. Dr. Özden Yalçın Özuysal

JÜRİ ÜYESİ
Doç. Dr. Kasım Diril

JÜRİ ÜYESİ
Doç. Dr. Hasan Akbaba

TABLE OF CONTENTS

TABLE OF CONTENTS I

LIST OF TABLES V

LIST OF FIGURES VII

ABBREVIATIONS XIII

ACKNOWLEDGEMENT XV

ABSTRACT 1

ÖZET 2

1. AIM OF THE STUDY 3

2. INTRODUCTION 3

2.1. Malignant Pleural Mesothelioma 3

2.2. Treatment Strategies of Malignant Pleural Mesothelioma 4

2.3. Identified Genomic Alterations in MPM 6

2.3.1. Loss of Function Mutations 7

2.3.2. Gain of Function Mutations 9

2.3.3. MPM-Related Novel Mutations 10

2.3.4. Deregulations in Cellular Signaling Cascades and Molecular Processes 10

2.4. Functional Genomic Studies in MPM 12

2.5. BUB1 13

3. MATERIALS AND METHODS 16

3.1. Type of the Research 16

3.2. Place and Time of Research 16

3.3. Research Material 16

3.3.1. Cell Lines and Cell Culture Consumables 16

3.3.2. Vectors 17

3.3.3. Molecular Cloning and PCR Reagents 21

3.3.4. Oligonucleotides 21

3.3.5. Bacterial Strains and Reagents 23

3.3.6. Conventional Genomic DNA Isolation Reagents and Buffer Recipe. 23

3.3.7. Western Blot Reagents, Buffer Recipes, and Antibodies 24

3.3.8. Bromodeoxyuridine (BrdU) Incorporation Assay Reagents 27

3.3.9. Senescence-Associated β-galactosidase (SA-β-Gal) Assay Reagents 27

3.4. Methods 29

3.4.1. Cell Culture 29

3.4.2. Construction of gRNA, and Overexpression Vectors 29

3.4.2.1. gRNA Vector Construction 29

3.4.2.2. Overexpression Vector Construction 31

3.4.3. Transformation 32

3.4.4. Colony PCR 32

3.4.5. Mini and Midi Culture and Plasmid Isolation 33

3.4.6. Stable Cas9 Expressing Monoclonal Cell Line Generation 33

3.4.7. T7 Endonuclease I (T7E1) Assay 35

3.4.8. Conventional Genomic DNA Isolation 35

3.4.9. Pooled Library Amplification 36

3.4.10. NGS Confirmation of Amplified Library 38
3.4.10.1. Preparation of Sequencing Library 38
3.4.10.2. Analysis of NGS Results 39
3.4.11. Puromycin Dose Curve 39
3.4.12. Virus Production and Infection 40
3.4.12.1. Virus Production 40
3.4.12.2. Virus Infection 40
3.4.12.3. Virus Production and MOI Calculation with Brunello Library 40
3.4.13. Doubling Time Calculation 41
3.4.14. Whole Genome CRISPR-Cas9 Screen and Preparation of Sequencing Library ... 41
3.4.14.1. MeT-5A Cell Line 41
3.4.14.2. H2052 Cell Line 42
3.4.14.3. H2452 Cell Line 42
3.4.14.4. H28 Cell Line 42
3.4.15. Analysis of Screen Results 44
3.4.16. Competition Assay 44
3.4.17. Establishment of BUB1 Knockout Cells 44
3.4.18. Western Blot 45
3.4.18.1. Protein Isolation 45
3.4.18.2. Determination of Protein Concentration 45
3.4.18.3. Running of Protein Samples 46
3.4.19. Colony Formation Assay 46
3.4.20. Soft Agar Assay 47
3.4.21. MTT Assay 47
3.4.22. Bromodeoxyuridine (BrdU) Incorporation Assay 47
3.4.23. Senescence Associated Beta-Galactosidase Assay (SA-β-Gal) 48
3.4.24. Cell Cycle and Apoptosis Assay 48
3.4.25. Immunofluorescence 49
3.4.26. Migration and Invasion Assays 49
3.4.27. Wound Healing Assay 50

3.4.28. In vivo Tumor Formation Assay 50
3.4.29. Public Data Set Analysis 50
3.4.30. Study Plan and Calendar 52
3.4.31. Data Evaluation 52
3.4.32. Limitations of the Study 52
3.4.33. Ethics Committee Approval 53

4. RESULTS 53

4.1. Selection of Cell Line Models 53

4.2. Establishment and Characterization of Stable Cas9-Expressing Monoclonal Cells 54 4.3. Library Amplification and NGS Confirmation 59

4.4. Puromycin Kill Curve and Selection Dose Calculation 61

4.5. Large Scale Virus Production 62

4.6. MOI Calculation 62

4.7. Whole Genome CRISPR-Cas9 Screen 64

4.8. Illumina Platform Compatible gRNA PCR Library Preparation and Next Generation Deep Sequencing 64

4.9. The Analysis of Whole Genome CRISPR-Cas9 Screen 67

4.10. Selection of Candidate Genes 72

4.11. Validation of Candidate Genes 76

4.12. *BUB1* is a Common Cancer Essential Gene 79

4.13. Generation of Polyclonal *BUB1* Knockout Cells 84

4.14. *BUB1* Knockout Attenuates MPM Cell Proliferation and 2D Colony Formation 85

4.15. *BUB1* Knockout Decreases 3D Anchorage Independent Growth of MPM Cells 88

4.16. Multiple Mechanisms Underlie the Proliferation Reduction upon *BUB1* Knockout 89

4.16.1. BUB1 Knockout Causes Cell Cycle Arrest in the G2 Phase 89

4.17. *BUB1* Knockout Decreases Migration and Invasion Capacity of MPM Cells ... 92

4.18. *BUB1* Knockout Reduces *In vivo* Tumor Engraftment Potential of MPM Cells 94

4.19. BUB1 Overexpression Increases Proliferation and 2D Colony Formation Capacity of MPM Cells 95

4.20. BUB1 Overexpression Increases 3D Anchorage Independent Growth of MPM Cells 97

4.21. BUB1 Overexpression Enhances Motility and Migration Capacity of MPM Cells 98

4.22. BAY-1816032 Inhibits Cell Proliferation 100

5. DISCUSSION 104

6. CONCLUSION AND FUTURE PERSPECTIVES 110

7. REFERENCES 111

8. APPENDIX 126

LIST OF TABLES

Table 1. Cell culture consumables. 16
Table 2. Vector list. 17
Table 3. List of enzymes, buffers, and other PCR reagents 21
Table 4. List of oligonucleotides used for gRNA cloning. 21
Table 5. List of PCR primers 22
Table 6. P5 and P7 primer list. 22
Table 7. Bacterial strains. 23
Table 8. List of reagents and consumables used for bacterial transformation studies. 23
Table 9. List of reagents used for DNA isolation. 23
Table 10. Lysis buffer recipe. 23
Table 11. List of reagents used for RIPA buffer preparation. 24
Table 12. Recipe of RIPA buffer. 24
Table 13. List of reagents used for SDS-PAGE gel preparation. 25
Table 14. 5 ml SDS-PAGE separating gel recipe. 25
Table 15. Stacking gel recipe 25
Table 16. Buffer recipes. 25
Table 17. Other reagents and consumables. 26
Table 18. Antibody list. 26
Table 19. Reagent list used for BrdU assay. 27
Table 20. Reagent list used for SA-β-Gal Assay. 27
Table 21. Solution recipes. 27
Table 22. List of other reagents. 28
Table 23. Kits. 28

Table 24. List of devices and softwares. 29
Table 25. Obtained infection rates calculated by proportioning number of infected and puromycin selected cells to uninfected control group in mini scale (6 well plate). 63
Table 26. Obtained infection rates calculated by proportioning number of infected and puromycin selected cells to uninfected control group in midi scale (100 mm dish). .....
63 Table 27. DNA concentrations of each time point/group of screen samples.
..... 64
Table 28. Concentration of the sequence libraries extracted from agarose gels 66
Table 29. List of genes that scored in common in three MPM cell lines but co-scoring with MeT-5A cell line based on gRNA score. 73
Table 30. List of genes that scored in common in three MPM cell lines but co-scoring with MeT-5A cell line based on gene score. 75
Table 31. The gene list that emerges as the intersection of two strategies. 75
Table 32. Evaluation criteria for genes. 78
Table 33. Tumor formation capacity of H2052 gRen and BUB1 g3 cells. 95

LIST OF FIGURES

Figure 1. Etiological factors and the most common genetic changes involved in the development of MPM. (Created with Biorender.com) 4
Figure 2. Summary of drugs tested in clinical trials and the gene/molecular pathways they target (Created with Biorender.com). 5
Figure 3. Molecules and molecular pathways altered in MPM development. (Adopted from Cakiroglu ve Senturk, 2020 (5)) 7
Figure 4. Spindle checkpoint control of BUB1. (Adopted from Yu and Zhanyun, 2005 (124)).
.....
14
Figure 5. The noncheckpoint kinetochore control of BUB1. (Adopted from Yu and Zhanyun, 2005 (124)). 15
Figure 6. lentiCas9-EGFP vector map. 17
Figure 7. lentiGuide-Hygro-dTomato vector map. 18
Figure 8. lentiGuide-Puro vector map. 18

Figure 9. pECPV (plentiCRISPRv2.1_EFS-Cas9-P2A-Venus) vector map. 19
Figure 10. lentiCRISPRv2 vector map. 19
Figure 11. pHIV-ZsGreen vector map. 20
Figure 12. pBI-GFP-Bub1-wt vector map. 20
Figure 13. Images of MeT-5A, H2052, H2452 and H28 cell lines under light microscope (10x magnification). Scale bar represents 100 µm. 54
Figure 14. FACS distribution graphics of MeT-5A, H2052, H2452, and H28 cell lines infected with lentiCa9-EGFP vector. Cells with high GFP expression, indicated by P3, were selected and sorted. 55
Figure 15. Western blot results of Cas9 protein levels tagged with Flag antibody in parental and sorted cells. 56
Figure 16. Flow cytometry analysis of GFP levels of Cas9 expressing MeT-5A, H2052, H2452, and H28 clones. 56
Figure 17. Western blot results of Cas9 protein levels tagged with Flag antibody in five clones with the highest GFP expression for each cell line. 57
Figure 18. Competition assay results of MeT-5A-Cas9, H2052-Cas9, H2452-Cas9, and H28Cas9 cells. While percentage of dTomato positive cells infected with gRen showed slight changes, this value decreased significantly over time in cells infected with RPA3 gRNA. 58
Figure 19. Agarose gel images of EGRF amplicons digested with T7E1 enzyme. While a ~950 bp intact band was detected in gRen cells, a ~950 bp intact band, as well as ~300 bp and ~600 bp bands were detected in cells targeted with EGFR gRNA consistent with mismatches resulted from indels. 59
Figure 20. Colonies obtained as a result of transformation of library plasmid DNA with Endura bacterial cells. 59
Figure 21. Lorenz curve of amplified (A) and original (B) Brunello libraries. 61
Figure 22. Images of MeT-5A, H2052, H2452, and H28 cell lines stained with crystal violet after different doses of puromycin treatment for 72 h. 62
Figure 23. Photographed flow of large-scale virus production and collection. 62
Figure 24. Depictured flow of the screen process. 64

Figure 25. Agarose gel image of sequence library samples. After PCR reaction conducted with P5 and P7 primers an amplicon of ~354 bp is expected. In our images, in addition to the expected band size, a higher length and fainter band is visible. Considering the agarose gel images in various studies of the Feng Zhang laboratory at MIT, which is accepted as the pioneering reference in this field, ready-to-run PCRs can contain diffuse contamination above the relevant band length. These bands mostly disappear by gel extraction, yet do not interfere with NGS. 66
Figure 26. Image of gRNA read distributions obtained by count_spacers.py analysis after deep sequencing. Genes whose distributions shift to the left side of the figure represent depleted genes, and genes that shift to the right side of the figure represent enriched genes. NGS Reads (Log2) indicates the representation of each gRNA. ..... 67 Figure 27. Graph showing the distributions of gRNAs and the positions of gRNAs targeting common essential genes (orange dots) in this distribution. 68
Figure 28. Graph showing the distributions of T14 gRNA scores relative to T0 gRNA scores, and the locations of gRNAs targeting common essential genes (orange dots) and non-targeting gRNAs in this distribution. 69
Figure 29. Significantly depleted and enriched gRNA distributions obtained by RRA analysis. Log2 fold changes negative values indicate depleted genes, and positive values indicate enriched genes. 70
Figure 30. Biological processes and molecular functions involving the genes with the highest depletion score after CRISPR screen obtained by KEGG analysis. 71
Figure 31. DAVID annotations showing the molecular functions in which the top 200 genes with the highest depletion score clustered. 72
Figure 32. Competition assay results of MeT-5A, H2052, H2452, and H28 cells. The percentage of Venus positivity of Day 0 samples of each group was normalized to 100 and percentage of other days were normalized accordingly. 77
Figure 33. Survival analysis results of *ATG9A, BUB1, CDK2, TMEM41B* and *VPS37A* genes in the TCGA MPM dataset. 78
Figure 34. *BUB1* gene effect scores of different project data from DepMap portal. .....
79 Figure 35. BUB1 expression levels of different tumor tissues compared with their

matching normal samples. Data was extracted from GEPIA by using TCGA matched normal and GTEx data. ANOVA was used for statistical analysis (log2FC cutoff 1, q value cutoff 0.01). ..... 80 Figure 36. BUB1 expression levels of different tumor tissues along with mesothelioma. Data was extracted from GEPIA by using only tumor data. ANOVA was used for statistical
analysis (log2FC cutoff 1, q-value cutoff 0.01). 81
Figure 37. BUB1 expression levels of different cancer cell lines compared to MPM cell lines. Data was extracted from CCLE RNA-Seq expression data. (RPKM: reads per kilobase). .....
81 Figure 38. BUB1 expression levels of tumor tissues from different GSE datasets compared with their matching normal samples. Data was extracted from GEO dataset. **p<0.01, ***p<0.001, Student's t-test. 82
Figure 39. Competition assay results of H2052, H2452, and H28 cells. While percentage of Venus positive cells infected with gRen showed slight changes, this value decreased over time in cells infected with BUB1 gRNAs. The percentage of Venus positivity of Day 0 samples of each group was normalized to 100 and percentage of other days were normalized accordingly. .....
83
Figure 40. Western blot results of control and *BUB1* knockout H2052, H2452, and H28 cell lines. 84
Figure 41. Immunofluorescence (IF) staining of control and BUB1 in knockout H2052, H2452, and H28 cell lines (40X magnification). 85
Figure 42. Cell proliferation profiles of control and *BUB1* knockout H2052, H2452, and H28 cell lines. MTT measurements were performed every 2 days starting 2 days after cell seeding (Day 0). Day 0 measurements were normalized to 100 and percentage of other days were normalized accordingly. Mean ±SD, n=4, ***p<0.001, Student's t-test. 86
Figure 43. BrdU incorporation of control and *BUB1* knockout H2052, H2452, and H28 cell lines. DAPI and BrdU stained cells were counted and the percentage of BrdU-positive cells was calculated by proportioning the number of cells stained with BrdU to the number of cells stained with DAPI. 20X magnification, scale bar represents 50 μm. Mean ±SD, n=6, **p<0.01, ***p<0.001, Student's t-test. 87

Figure 44. Colony formation assay results of *BUB1* knockout H2052, H2452, and H28 cell lines. Relative intensity was calculated by proportioning the intensities of knockout cells to gRen cells. Mean ±SD, n=3, **p<0.01, ***p<0.001, Student's t-test. ..... 88 Figure 45. Soft agar images showing the effect of *BUB1* knockout on 3D anchorage independent growth of H2052, H2452, and H28 cells. Colonies with diameter greater than 35 μm were counted. 10X magnification, scale bar represents 100 μm. Mean±SD, n=4, ***p<0.001, Student's t-test. ..... 88 Figure 46. Cell cycle distribution of *BUB1* knockout H2052, H2452, and H28 cells. Mean ±SD, n=3, two-way ANOVA multiple comparison. ..... 89 Figure 47. Gene set enrichment analysis of transcription factors important for the G1/S transition, E2F and MYC, in BUB1 low and high MPM samples. ..... 90 Figure 48. SA-β-Gal staining results of control and *BUB1* knockout H2052, H2452, and H28 cells. All cell population as well as SA-β-Gal stained cells were counted and the percentage of SA-β-Gal staining was calculated by proportioning the number of stained cells to the total number of cells. 10X magnification, scale bar represents 100 μm. Mean ±SD, n=5, *p<0.05, **p<0.01, ***p<0.001, Student's t-test. ..... 91 Figure 49. Flow cytometry analysis of apoptosis of control and *BUB1* knockout H2052, H2452, and H28 cells. Percentage of apoptotic cells was calculated as the sum of early (Q3) and late (Q2) apoptosis. The images that best represent the average are given. Mean ±SD, n=3, *p<0.05, **p<0.01, ***p<0.001, ns: not significant, Student's t-test. ..... 92 Figure 50. Migration assay results of control and *BUB1* knockout H2052, H2452, and H28 cells. 10X magnification, scale bar represents 100 μm. The data is presented as mean ±SD (n=6). *p<0.05, **p<0.01, ***p<0.001, Student's t-test. ..... 93 Figure 51. Invasion assay results of control and *BUB1* knockout H2052, H2452, and H28 cells. 10X magnification, scale bar represents 100 μm. Mean ±SD, n=6, **p<0.01, ***p<0.001, Student's t-test. ..... 94 Figure 52. Western blot results of excised tumor samples. gRen and BUB1 g3 samples were run on nonconsecutive lanes. ..... 95 Figure 53. Western blot results of control (empty vector) and BUB1 overexpressing H2052,

and H2452 cell lines. 95
Figure 54. BrdU incorporation of control and BUB1 overexpressing H2052, and H2452 cells. DAPI and BrdU stained cells were counted, and the percentage of BrdU-positive cells was calculated by proportioning the number of cells stained with BrdU to the number of cells stained with DAPI. 20X magnification, scale bar represents 50 µm. Mean ±SD, n=6, **p<0.01, ***p<0.001, Student's t-test. 96
Figure 55. Colony formation assay results of control and BUB1 overexpressing H2052, and H2452 cells. Relative intensity was calculated by proportioning the intensities of overexpression cells to Empty cells. Mean ±SD, n=3, *p<0.05, Student's t-test. .....
97 Figure 56. Soft agar images showing the effect of BUB1 overexpression on 3D anchorage independent growth of H2052, and H2452 cells. Colonies with diameter greater than 35 µm were counted. 10X magnification, scale bar represents 100 µm. Mean ±SD, n=4, *p<0.05, **p<0.01, Student's t-test. 97
Figure 57. Wound healing assay results of control and BUB1 overexpressing H2052, and H2452 cells. Wound areas were imaged and measured at T0 and different time points and the % closure was calculated relative to T0. 10X magnification, scale bar represents 100 µm. Mean ±SD, n=6, *p<0.05, **p<0.01, ***p<0.001, ns: not significant, two-way ANOVA multiple comparison. 98
Figure 58. Migration assay results of control and BUB1 overexpressing H2052, and H2452 cells. 10X magnification, scale bar represents 100 µm. Mean ±SD, n=6, *p<0.05, ***p<0.001, Student's t-test. 99
Figure 59. Gene set enrichment analysis of target genes regulating the EMT phenotype in BUB1 low and high MPM samples. 100
Figure 60. The 50% inhibitory concentrations (IC50) of BAY-1816032 in H2052, H2452, and H28 cell lines. 100
Figure 61. Colony formation assay results of control and BAY-1816032 treated H2052, H2452, and H28 cells. Relative intensity was calculated by proportioning the intensities of treated cells to control cells. Mean ±SD, n=3, ***p<0.001, Student's t-test. .....
101 Figure 62. Soft agar images showing the effect of BAY-1816032 on 3D anchorage

independent growth of H2452 cells. Colonies with diameter greater than 35 μm were counted. 10X magnification, scale bar represents 100 μm. Mean ±SD, n=4, **p<0.01, ***p<0.001, Student's t-test. 102
Figure 63. Cell cycle distribution of H2052, H2452, and H28 cells treated with BUB1 inhibitor. 102
Figure 64. Flow cytometry analysis of apoptosis of control and BUB1 inhibitor treated H2052, H2452, and H28 cells. Percentage of apoptotic cells was calculated as the sum of early (Q3). 103

ABBREVIATIONS

MPM	Malignant pleural mesothelioma
FDA	Food and Drug Administration
CGH	Comparative Genomic Hybridization
NF2	NF2, Moesin-Ezrin-Radixin Like (MERLIN) Tumor Suppressor
CDKN2A	Cyclin Dependent Kinase Inhibitor 2A
BAP1	BRCA1 Associated Protein 1
TP53	Tumor Protein P53
CDKIs	Cyclin-Dependent Kinase Inhibitors
LP-WGS	Low-Pass Whole Genome Sequencing
NGS	Next-Generation Sequencing
COSMIC	Catalog of Somatic Mutations in Cancer
ICGC	International Cancer Genome Consortium
TCGA	The Cancer Genome Atlas
EGFR-TKIs	EGFR Tyrosine Kinase Inhibitors
VEGF	Vascular Endothelial Growth Factor
PKC	Protein Kinase C
KIF	Kinesin Family Proteins

MSAC	Mitotic Spindle Assembly Checkpoint
BUB1	Budding Uninhibited By Benzimidazoles
FACS	Fluorescence Activated Cell Sorting
CFU	Colony Formation Unit
BCA	Bicinchoninic Acid
BrdU	Bromodeoxyuridine
SA-β-Gal	Senescence Associated Beta-Galactosidase
GEO	Gene Expression Omnibus
EMT	Epithelial-Mesenchymal Transition
DEGs	Differentially Expressed Genes
NES	Normalized Enrichment Scores
FDR	False Discovery Rates
T7E1	T7 Endonuclease I
CFU	Colony Formation Unit
AUC	Area Under the Curve
MOI	Multiplicity of Infection
CCLE	Cancer Cell Line Encyclopedia
RPKM	Reads per Kilobase
PI	Propidium Iodide
IC50	The 50% Inhibitory Concentrations
CCND1	Cyclin D1
NPIPA5	Nuclear Pore Complex Interacting Protein Family member A5
PIKFYVE	Phosphoinositide Kinase, FYVE-Type Zinc Finger Containing

USP17L25	Ubiquitin Specific Peptidase 17 Like Family Member 25
ATG9A	Autophagy Related 9A
VPS37A	VPS37A subunit of ESCRT-I
ESCRT	Endosomal Sorting Complex Required for Transport
TMEM41B	Transmembrane Protein 41B
CDK2	Cyclin Dependent Kinase 2

ACKNOWLEDGEMENT

First, I would like to thank my supervisor, Assoc. Prof. Şerif Şentürk, for his mentorship and academical contributions.

Also, I would like to thank my thesis monitoring committee members, Yavuz Oktay and Assoc. Prof. Özden Yalçın Özuysal for their valuable comments and contributions. I thank Assoc. Prof. Gökhan Karakülah, Ahmet Bursalı and Sude Eriş for bioinformatical analysis, Ceren Ülker for tumor injections and Mazhar Adlı for his advices during screen process. I thank TÜBİTAK-BİDEB 2211/C National PhD Scholarship Program in the Priority Fields in Science and Technology for their bursary support during my PhD.

My special thanks go to my labmates Bengisu Uluata Dayanç, Zeynep Güngör, Merve Uysal, Sude Eriş, Minenur Kalyoncu, and Buse Akdemir and my former labmates Aslı Kurden Pekmezci, Dilara Demirci Özata, Özlem Şilan Coşkun Deniz, and Fatma Aybüke Mazı. We became sisters more than being labmates and technicaly support each other in this lab. My former labmates, even though we haven't worked together for a long time, we are still there for each other. I also thank my buddies Özgün Özalp and Tuğba Uysal Kılıç for their support and Emrah Şengöz for always listening to me when I feel down.

I am grateful to my sister from another mother, Değer Özerdem Tezcan, for always being with me unconditionally and being one of my pillars in this life. I also thank her for making me the aunt of an adorable boy.

Last and foremost, I would like to thank my mother Kadriye Şengün and my aunts Aysel and Fatma Şengün for their endless love and patience.

IDENTIFICATION AND FUNCTIONAL CHARACTERIZATION OF ESSENTIAL GENES INVOLVED IN THE DEVELOPMENT OF MALIGNANT PLEURAL MESOTHELIOMA USING CRISPR/CAS9-BASED NEGATIVE SELECTION SCREENING

Ece Çakıroğlu, Dokuz Eylul University Izmir International Biomedicine and Genome Institute, ece.cakiroglu@ibg.edu.tr

ABSTRACT

Today, the identification of ideal cancer models and high-throughput screening methods has provided the appropriate environment for the discovery of new therapeutic targets. On the other hand, there are only few studies characterizing the genes playing an important role in malignant pleural mesothelioma (MPM), a rare cancer with increasing incidence rates and limited therapy options.

In this project, whole genome CRISPR/Cas9 negative-selection method was utilized in order to identify and functionally characterize essential genes playing critical roles in MPM cell survival. Firstly, preliminary studies were conducted on three different MPM cell lines and one non-tumorigenic mesothelial cell line to obtain clonal sublines showing permanent Cas9 nuclease expression. In the second step, the lentiviral plasmid-based genomic gRNA pooled library to be used in the screening was recovered and amplified. Subsequently, a negative functional screening was performed. Genomic DNA was extracted from the T0 and T14 cultures and the gRNA region was amplified by PCR. The barcoded PCR samples were sequenced with next generation sequencing and the representation for each gRNA and simultaneously their corresponding target genes were quantified. At this point, BUB1, a druggable mitotic checkpoint serine/threonine kinase, was identified as an essential gene for MPM cell survival and its role on phenotypic changes (cell death, cell cycle arrest, etc.) were studied in terms of proliferation, apoptosis, senescence, migration and invasion. The findings suggest that BUB1 may serve as a potential therapeutic target for MPM.

Keywords: malignant pleural mesothelioma, CRISPR/Cas9, whole-genome screening, genefunction- phenotype

MALİGN PLEVRAL MEZOTELYOMA GELİŞİMİNDE ROL OYNAYAN ESANSİYEL GENLERİN CRISPR/CAS9 BAZLI NEGATİF SEÇİLİM TARAMA YÖNTEMİYLE TANIMLANMASI

Ece Çakıroğlu, Dokuz Eylül Üniversitesi İzmir Uluslararası Biyotıp ve Genom Enstitüsü, ece.cakiroglu@ibg.edu.tr

ÖZET

Günümüzde, ideal kanser hücre modellerinin ve yüksek-çıktılı fonksiyonel genomik tarama yöntemlerinin tanımlanması yeni tedavi hedeflerinin keşfedilmesi için uygun ortamı sağlamıştır. Öte yandan, MPM sağkalımında rol oynayan genleri nitelendirmeye yönelik pek az başarılı çalışma bulunmaktadır.

Bu projede, MPM sağkalımında etkin rol oynayan esansiyel genlerin tanımlanması ve fonksiyonel olarak karakterize edilmesi için CRISPR/Cas9 tüm genom negatif-seçilim tarama yöntemi kullanılmıştır. İlk aşamada; 3 farklı MPM hücre hattı ve 1 tümörojenik olmayan mezotel hücre hattında kalıcı Cas9 ifadesi gösteren alt-hücre hatları elde edilmiştir. İkinci aşamada ise, taramada kullanılacak lentiviral plazmid-bazlı gRNA havuz kütüphanesi çoğaltılmıştır. Ardından, negatif-seçilim tarama gerçekleştirilmiştir. T0 ve T14 kültürlerinden genomik DNA çıkartılıp gRNA bölgesi PCR yöntemiyle çoğaltılmıştır. Barkodlanan PCR örnekleri, yeni nesil derin dizileme ile okunmuş ve sonucunda her bir gRNA ve aynı zamanda hedefledikleri genler için temsiliyet hesaplanmıştır. Son olarak, bir mitotik kontrol noktası serin/treonin kinazı olan BUB1 geni MPM hücre sağkalımı için esansiyel olarak tanımlanmış ve fenotipik değişikler (hücre ölümü, hücre döngüsü, vb.) üzerine etkisi hücre çoğalması, apoptoz, senesens, migrasyon ve invazyon yönünden araştırılmıştır. Elde edilen bulgular, BUB1'in MPM'de potansiyel tedavi hedefi olabileceğini göstermektedir.

Anahtar Kelimeler: malign plevral mezotelyoma, CRISPR/Cas9, tüm genom tarama, genişlev-fenotip ilişkisi

1. AIM OF THE STUDY

Malignant pleural mesothelioma (MPM) is a rare cancer associated with an increasing incidence. Existing treatment options are limited to chemotherapy and/or multimodal therapy. Despite such an aggressive therapy regimen, MPM has poor prognosis and low survival rates. Several genes and pathways have been associated with MPM so far, yet the absence of a defined dependency or vulnerability hinders targeted treatment alternatives. The aim of this study is to elucidate and functionally characterize the genes that are essential for MPM cell survival using genome-wide CRISPR/Cas9 screening strategy.

2. INTRODUCTION

2.1. Malignant Pleural Mesothelioma

Malignant pleural mesothelioma (MPM) is the cancer of the pleura, the lining that protects the chest cavity (Figure 1). Despite being categorized as a rare cancer, MPM accounts for around 80% of all mesotheliomas and is also one of the highly lethal and most aggressive cancers, with more than 26000 recorded deaths globally in 2020 (1). Also, according to the latest statistics, ~3000 new patients were diagnosed in the United States (2) and ~30000 new patients were diagnosed worldwide (1). While occupational asbestos exposure is the main etiological cause of MPM, environmental exposure can also occur through the inhalation of asbestos fibers in the air or in contaminated soil and asbestos exposure accounts for 80% of identified cases (3,4). Despite the implementation of strict regulations and bans on the use of asbestos in western nations, MPM prevalence is predicted to rise globally over the next few decades. This is due to the long latency period of the disease, which is estimated to be around 40 years after exposure to asbestos fibers. Besides, MPM is an ongoing global health issue because of the increasing usage, importation and exporting of asbestos in many developing countries (3–6). Other known causes of MPM include exposure to the fibrous mineral erionite, radiation, and simian virus 40 (4). In addition to these exposures, there are also rare familial forms of the disease that are thought to be caused by genetic predisposition and have been described in many countries around the world, particularly in the United States and Turkey, mainly in the Cappadocia region (5,7–10).

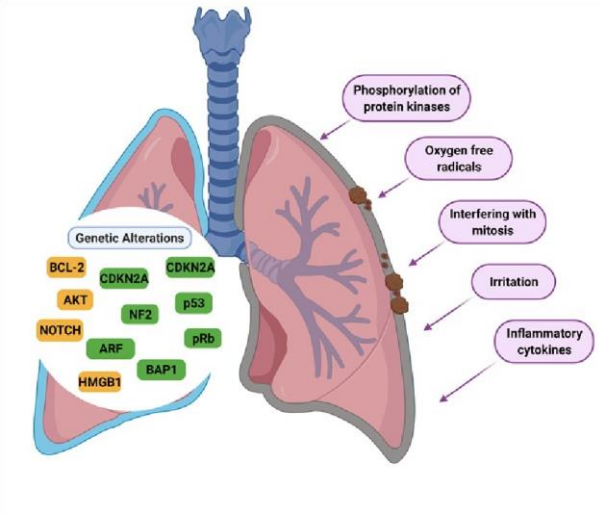


Figure 1. Etiological factors and the most common genetic changes involved in the development of MPM. (Created with Biorender.com)

Epithelioid MPMs are the most common subtype, accounting for approximately 50-70% of cases. These tumors are characterized by a predominantly epithelial cell pattern, which resembles the normal mesothelial cells of the pleura. Epithelioid MPMs tend to present with pleural effusions, and patients with this subtype generally have better survival rates than those with sarcomatoid or biphasic MPMs. Sarcomatoid MPMs, which account for approximately 10-20% of cases, have a spindle cell morphology and are associated with a worse prognosis than epithelioid MPMs. These tumors tend to present as a pleural mass, rather than pleural effusions, and are more aggressive than the other subtypes. Biphasic MPMs, which make up approximately 20-35% of cases, contain both epithelial and sarcomatoid components (11,12).

2.2. Treatment Strategies of Malignant Pleural Mesothelioma

In general, MPM is characterized by an invasive character, late diagnosis, and low survival rates. MPM generally has a poor prognosis with an average survival time of 1 year from diagnosis and has no definitive treatment (12). Despite recent advances in medical oncology, MPM remains resistant to multimodal therapeutic approaches including the combination of chemotherapy, radiation, and surgical resection (13,14). The latest drug officially approved in 2020 by the FDA for the treatment of MPM is the Nivolumab in combination with Ipilimumab (15). This drug combination is the first FDA-approved drug regimen for MPM in ~16 years after injectable pemetrexed, a folic acid-like chemotherapeutic agent, which was approved in

2004. In addition, there is not a standard treatment for secondline therapy. Today, a holistic and effective MPM treatment is still under investigation (14,16,17). Targeted studies with small chemical inhibitors ((PI3K / mTOR (LY3023414) and aurora kinase A (alisertib)), mesothelin targeting monoclonal antibody-drug components (anetumab ravtansine and BMS-986148), monoclonal antibodies targeting the immune control point (pembrolizumab, avelumab, tremelimumab), antiangiogenic drugs (bevacizumab, nintedanib, cediranib), and cellular therapies are being studied widely (16,18–20). As of today, there are about 75 ongoing clinical trials that have been initiated in recent years (21) (Figure 2). These studies are mostly clinical trials that examine the efficiency of known chemotherapeutic agents in combination with the aforementioned drugs on progression-free survival. However, the lack of significant improvements in overall survival and severe side effects remain as critical issues (22). Additionally, for some of these studies, transition to the next phase is considered risky. Taken together, current treatment options are considered to be insufficient in the primary treatment of MPM or in preventing its progression.

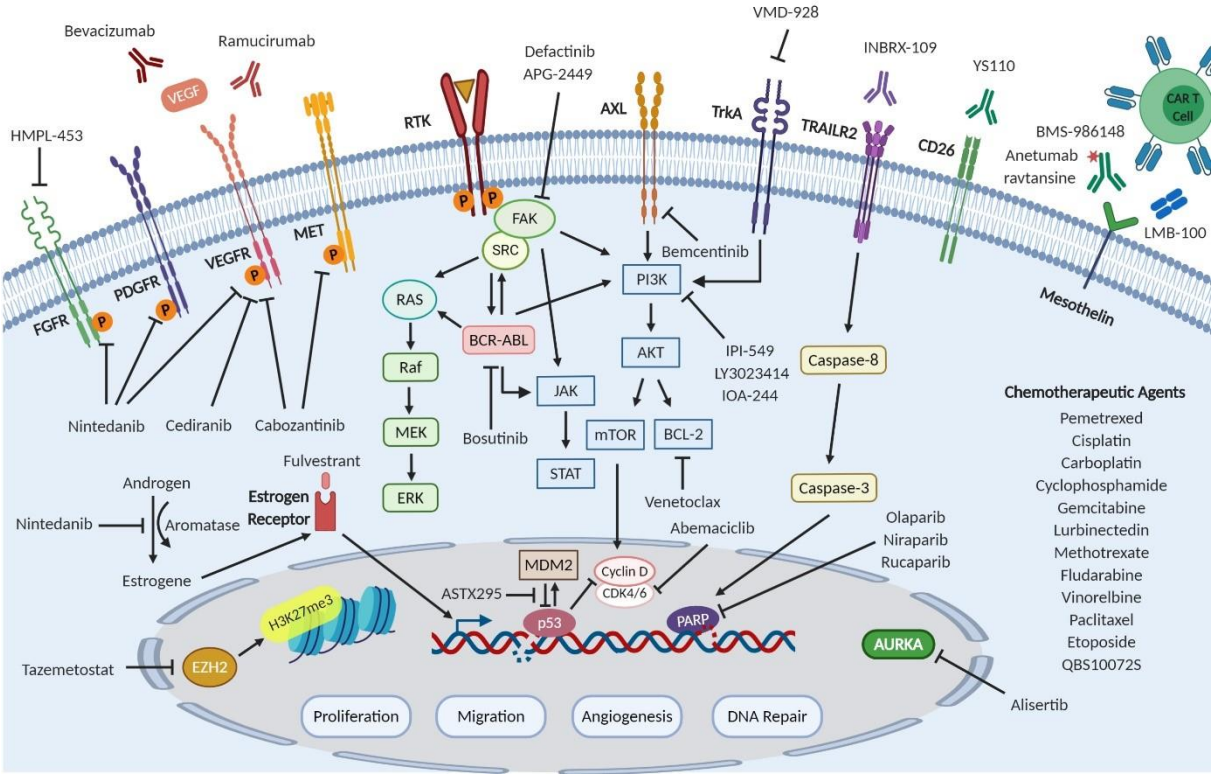


Figure 2. Summary of drugs tested in clinical trials and the gene/molecular pathways they target (Created with Biorender.com).

Although many molecular pathways have been identified in MPM to date, there isn't any defined targeted therapy for this deadly disease yet. Clinical trials conducted to target these molecular pathways have shown limited effectiveness (13,16). MPM is a heterogeneous cancer with complex molecular changes underlying it. To date, genomic analyzes have revealed many genetic, epigenetic, and transcriptomic irregularities in MPM.

2.3. Identified Genomic Alterations in MPM

The main mechanisms involving the MPM tumorigenesis process are the acquisition of changes that promote oncogenic transformation, cellular proliferation, and invasion. Recent comprehensive genomic studies have significantly contributed to the biology of MPM (Figure 3). Due to the rarity of tumors and therefore the limited number of samples, the chromosomal alterations identified in genetic and genomic studies, although highly informative, often represent recurrent mutations. These genetic alterations are often point mutations affecting multiple regions of the genome and/or loss-of-function mutations triggered by copy number changes (23–26). In contrast to other cancers, which are often characterized by the acquisition of oncogenic function gains, MPM carcinogenesis is mostly driven by genomic losses.

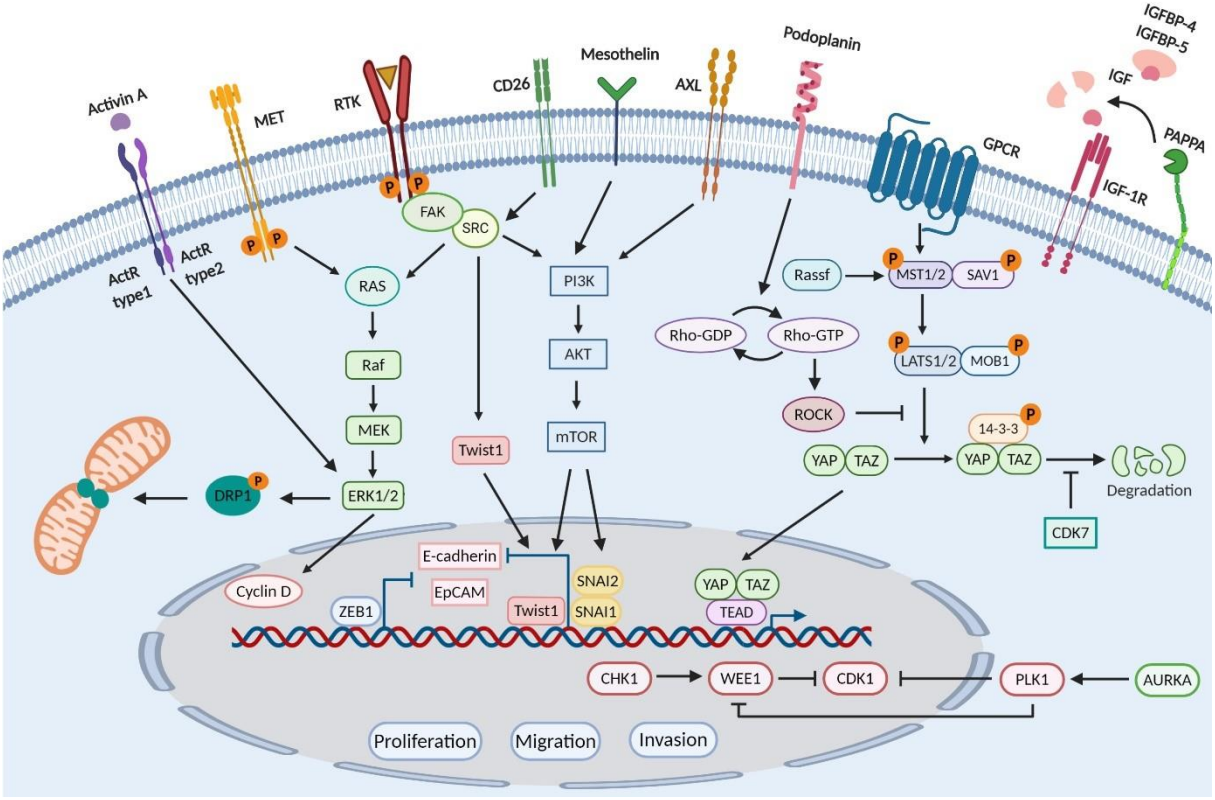


Figure 3. Molecules and molecular pathways altered in MPM development. (Adopted from Cakiroglu ve Senturk, 2020 (5))

2.3.1. Loss of Function Mutations

Karyotype and comparative genomic hybridization (CGH) studies have confirmed that the loss of chromosomal regions 1p, 3p, 6q, 9p, 13q, 15q, and 22q are common in MPM (5,27,28) and are often associated with inactivating mutations in tumor suppressor genes *NF2* (NF2, Moesin-Ezrin-Radixin Like (MERLIN) Tumor Suppressor), *CDKN2A* (Cyclin Dependent Kinase Inhibitor 2A), *BAP1* (BRCA1 Associated Protein 1), and *TP53* (Tumor Protein P53) which play important roles in regulating cell growth and division, and their inactivation can lead to uncontrolled cell proliferation and increased risk of malignant transformation (24–26,29).

BAP1, one of the most frequently mutated genes in MPM, is affected in more than half of MPM tumors (30). *BAP1* plays a critical role in regulating a number of cellular processes including cell cycle progression, cellular proliferation, differentiation, energy metabolism, ferroptosis, and Ca2+-signaling mediated apoptosis (31–34). *BAP1* loss of function is usually caused by somatic mutations, splice variants, gene fusions, and copy number changes (25,35,36). Recently, heterozygous germline mutations in the *BAP1* gene, which lead to the loss of function of both alleles, have been associated with a rare cancer predisposition syndrome called "BAP1 cancer syndrome". Individuals with BAP1 cancer syndrome are at increased risk of developing several types of cancer, including MPM and uveal melanoma (37–40).

Similarly, the *CDKN2A* gene, which encodes the tumor suppressor proteins p16INK4a and p14ARF (41) is one of the most frequently inactivated tumor suppressor genes in MPM. Approximately 50% of MPM cases exhibit inactivation of the *CDKN2A* gene (24). In addition, complete genetic loss of the INK4 locus, which is characterized by co-deletion of *CDKN2A* and *CDKN2B*, is also observed in MPM, although less frequently. (28). *CDKN2B* encodes the tumor suppressor protein p15INK4B which also plays a role in regulating the cell cycle by inhibiting the activity of cyclin-dependent kinases. (41). The cyclin-dependent kinase inhibitors (CDKIs) p16INK4A and p15INK4B are highly homologous proteins that share similar structural and functional characteristics. They prevent the progression of the cell cycle and the cellular proliferation by inhibiting CDK4/6 activity, which results in

hypophosphorylation and functional activation of pRb (42). *CDKN2A* and *CDKN2B* codeletion causes shorter survival rates in MPM. Recent studies indicate that cell cycle-targeted therapies, particularly CDK4/6 inhibitors, may be beneficial for MPM patients with loss of function of p16INK4A and p15INK4B (5,43–45).

NF2 inactivation is the other most frequent genetic change in MPM, and it was originally identified in nearly 50% of all MPM tumors in the mid-1990s (29). The *NF2* gene encodes a protein called Merlin that acts as a tumor suppressor by regulating cell proliferation and contact inhibition. Various experimental evidence suggests that loss of function of the *NF2* gene in MPM often leads to uncontrolled cell proliferation and invasion through the hyperactivation of the focal adhesion kinase (FAK) and c-Src signaling pathways (46,47).

In addition to the loss of *BAP1*, *CDKN2A*, and *NF2* genes, the *TP53* gene, which is a well-defined tumor suppressor, is also frequently inactivated in MPM. Inactivation of the *TP53* gene was found to be associated with lower survival rates in patients with MPM. This indicates that TP53 mutations are associated with a more aggressive phenotype in MPM (48). A new molecular subtype of MPM with recurrent *TP53* mutations, co-mutations in the *SETDB1* gene, which encodes for a transcription suppressor histone methyltransferase, and genomic near-haploidization was recently identified by Hmeljak et al (48).

Other, less common, recurrent gene mutations are seen in the *LATS2* and *SETD2* genes. *LATS2* is a tumor suppressor gene that is involved in the regulation of cell growth and division. Alterations in the *LATS2* gene have been identified as an MPM-specific molecular event. These alterations usually occur as a result of large deletions and point mutations and often found in conjunction with inactivation of the *NF2* gene (49). *SETD2* tumor suppressor gene, as well as other SETD family members, is frequently inactivated in MPM through a variety of recurrent mechanisms including gene fusions, splicing alterations, and nonsynonymous mutations (50,51). Although the exact functional consequences of SETD2 inactivation in MPM are not fully understood, recent research has shed some light on the potential impact of this inactivation on cellular processes. A study by Park et al. found that SETD2 methylates microtubules during mitosis and cytokinesis, and that loss of this function leads to defects in mitotic spindle formation, impaired DNA repair, and genomic instability. Taken together, this may partly explain the high frequency of aneuploidy observed in MPM (52).

2.3.2. Gain of Function Mutations

Although less frequently, recurrent chromosomal gains have been reported in MPM. Specifically, gains in copy number have been observed in regions 1q, 5p, 7p, 8q, and 17q. The first recurrent oncogenic gain-of-function change reported in MPM is *TERT* gene copy number gains and promoter mutations, which are generally observed in ~10-15% of all cancer types (53,54). In addition to the previously reported recurrent chromosomal gains in MPM, a recent study using low-pass whole genome sequencing (LP-WGS) which analyzed a set of 21 MPM cases with matching normal samples have identified novel copy number gains in the *CD79B* and *MDM4* genes (51). Considering their oncogenic role in other cancers, fully understanding the functional implications of these alterations and how they contribute to the pathogenesis of MPM may make them important targets for MPM therapy. A highly comprehensive genomic study conducted by Bueno et al., identified recurrent gains in the *RPTOR* gene in MPM. *RPTOR* is a gene that encodes the regulatory-associated protein of mTOR, which is a key regulator of cell growth and proliferation. Dysregulation of mTOR signaling has been implicated in the development and progression of various types of cancers, including colorectal cancer, where RPTOR has been shown to have oncogenic functions (50). Although this suggests that dysregulation of mTOR signaling may also play a role in the pathogenesis of this disease, further research is needed to confirm the role of *RPTOR* in MPM biology. Similarly, dysregulated amplification of the *MYC* gene, which is also reproducible in asbestosinduced mouse MPM models, has been reported in a small fraction (< 5%) of human MPM cases (55,56).

2.3.3. MPM-Related Novel Mutations

Genomics studies have been completely transformed by high-throughput next-generation sequencing (NGS) technologies, which also make it possible to characterize somatic mutations in cancer in high resolution. Furthermore, the development of publicly available resources including the Catalog of Somatic Mutations in Cancer (COSMIC), the Cancer Genome Atlas (TCGA) and, the International Cancer Genome Consortium (ICGC) has been promoted by the advent of these technologies (57–59). In silico analyzes have been conducted by several research groups on TCGA and other open access datasets to advance our understanding of MPM biology. These analyzes identified new genetic variations and confirmed previous

findings (33,34,37,38,40,60,61). The data obtained indicate that the recurrent novel variations are related to cellular processes such as RNA metabolism, histone methylation, DNA repair, and angiogenesis. In addition, important molecular changes that affect PI3K-Akt, Hippo, Wnt, PDGF and FGF signaling pathways have also been identified (50,62,63). Genes mutated in these pathways include *APC, ARID1A, BMPR1A, CHEK2, DVL1, EPHB1, FBXW7, KDR, MAP2K1, PDGFRA, PTEN, RB1, SMARCA4, SMARCB1, HRAS,* and *WRN* (5,50,63–68) which have also been shown to be altered in lung adenocarcinomas (69), colorectal cancers (70–73), and breast cancers (74). In addition, oncogenic mutations in the *ABL1, EP300, PIK3CA, PIK3C2B, PTPN11* and *SETDB1* genes (5,48,50,62–64) and novel gains in regions covering the *RHEB, KDM5A, AXIN2, RICTOR, TRIO* and *DVL1* genes have been identified (5,51,64).

2.3.4. Deregulations in Cellular Signaling Cascades and Molecular Processes

Growth factor signaling pathways are frequently deregulated in MPM and contribute to carcinogenesis. Deregulation of autocrine and paracrine signaling (28), particularly the dysregulation of receptor tyrosine kinase (RTK) signaling, is a common mechanism that contributes to carcinogenesis in MPM. Activation of RTKs can result in abnormal activation of downstream signaling pathways, including the PI3K/Akt/mTOR and MAPK pathways (48,75,76). These pathways are critical signaling pathways involved in the regulation of various biological processes, including transcription, translation, cell proliferation, growth, and migration and frequently deregulated in MPM, leading to the abnormal activation of downstream targets, which contribute to the development and progression of this disease. Independent studies have shown that Akt and mTOR phosphorylation levels are positively correlated in more than half of MPM cases. The PI3K/Akt/mTOR pathway is regulated by a number of positive and negative regulators, including PTEN which is a tumor suppressor gene that negatively regulates the pathway (77–79). Additionally, both older and more recent studies have shown that the MAPK cascade has increased intracellular signaling molecule activity (48,80,81). Malignant and nonmalignant cells were failed to be distinguished based on the activation status of this pathway, which brought attention to complex regulation of MPM (75,81). In light of the current state of our understanding of MPM, it is difficult to adopt treatment strategies, and further research is needed to highlight the function of the MAPK pathway in the pathophysiology of MPM.

Additionally, MPM has been linked to increased EGFR signaling pathway activation (82–84). However, unlike in lung cancer, where EGFR mutations and expression are associated with a better response to EGFR inhibitors, in MPM, EGFR mutation and expression status have been correlated with a higher overall survival rate. This may partly explain why the firstgeneration EGFR tyrosine kinase inhibitors (EGFR-TKIs), Erlotinib and Gefitinib, did not show significant responses in Phase II clinical trials in MPM patients. (85,86). Therefore, the findings show that EGFR-TKIs would not be considered therapeutically significant in MPM when targeting the EGFR pathway.

Pathological angiogenesis, a hallmark of cancer, is a crucial mechanism in the proliferation, invasion, and metastasis of cancer cells (87). Correspondingly, deregulated angiogenesis has been associated with the aggressive behavior of the cancer cells and resistance to chemotherapy in MPM (88,89). The VEGF family proteins and their receptors (VEGFRs) play a crucial role in angiogenesis, and increased expression of these proteins and their receptors have been found in MPM. Additionally, downstream signaling mediators of the VEGF/VEGFR signaling axis, such as Akt and PKC (protein kinase C), have been implicated in the regulation of MPM cell survival and proliferation (90). Similarly, the FGF and PDGF pathways, which are also involved in angiogenesis, have been linked to MPM tumorigenesis through autocrine and paracrine signaling mechanisms (91).

Chromosomal segregation, a crucial process for the accurate distribution of genetic material during cell division and thus genome stability, is disturbed in MPM and leads to frequent acquisition of genome-wide copy number changes. Several molecular networks are involved in regulating spindle organization and chromosomal segregation during cell division including the condensin complex, kinesin family proteins (KIFs), cyclins, and the MSAC (mitotic spindle assembly checkpoint) pathway (5,92–95). Despite the absence of mutations, these molecular networks exhibit significant deregulations. In particular, genes encoding the condensin complex subunits *CNAP1*, *NCAPD3*, and *BRRN1*, kinesin family genes (*KIF14*, *KIF23*, *KIFC1*, and *KIF4A*), and cyclins (*CCNA2*, *CCNB1*, *CCNB2*, and *CCNL2*) were significantly elevated in MPM (96). In addition, elevated expression of crucial elements of the MSAC pathway, including BUB1 and MAD2L1 (97), as well as other MSAC components *AURKA*, *AURKB*, and Survivin, also known as *BIRC5*, which are involved in centrosome maturation and cytokinesis progression, has been linked to poor prognosis in MPM (97). These

findings suggest that microtubule network and the MSAC pathway hold promise as a potential therapeutic strategy for MPM.

2.4. Functional Genomic Studies in MPM

Functional genomic studies aim to reveal the relationship between genetic abnormalities and the underlying biological processes that contribute to the development and progression of the disease and to translate the obtained findings into clinical applications. Although there are relatively few functional genomic studies in MPM, the existing literature has successfully validated the functional outcomes of several genetic abnormalities that are significantly related with wide range of biological processes, including cell division, transcription, signal transduction, and migration. To date, RNAi-based studies identified potential target genes as receptor tyrosine kinases (*AXL*, *EPHB2*, and *MET*) (98–100), serine/threonine kinases (*activin A*) (101), transcription factors (*ZEB1, ERβ, SP1*, and *WT1*) (102–105), *MSLN* (106), *YAP* (107,108), *PAPPA* (109), *ADAR2* (110) , *SMG6* (111), VDAC1 (112), *FTL* (113), *IGF2BP3* (114), and *SmgGDS* (115).

The first large-scale loss-of-function RNAi screening in MPM cells was performed by Sudo et al (116). This was followed by studies by Linton et al (117), Okonska et al (118), and Dell'Anno et al (119). According to these studies, although more potential candidate genes were found, the role of *COPA*, *CDK1*, *NDC80, PLK1, EIF4G1*, and *RAN* genes in MPM was clarified and these genes were identified as potential drug targets. Additionally, a kinomewide CRISPR negative selection screen showed *WEE1* deletion/inhibition sensitizes MPM cells to cisplatin/pemetrexed treatment (120) and a recent CRISPR based whole genome screen identified *KAP1* as a novel non-genetic dependency of MPM (121).

Despite all the studies conducted to date, more data is needed to fully understand the biological basis of MPM.

2.5. BUB1

BUB1 (Budding uninhibited by benzimidazoles) gene encodes an enzyme-structured serine-threonine kinase protein that functions at the mitotic checkpoint in the cell cycle (122). BUB1 basically consists of three main regions: a conserved N-terminal region that contains the

kinetochore localization domain; an intermediate, non-conserved region that is required for protein recruitment; and a C-terminal region that contains a catalytic serine/threonine kinase domain (123). During mitosis, BUB1 localizes to the kinetochores and phosphorylates members of the mitotic checkpoint complex. This activates spindle control and signaling during cell division (122) ensuring that the chromosomes are properly aligned before the cell progresses to anaphase. BUB1 is also required for the proper localization of Mad1 and Mad2 to the kinetochore. After localization, Mad1 triggers a conformational change of Mad2, facilitating its binding to Cdc20. This inhibits the anaphase promoting complex/cyclosome (APC/C) by providing the formation of an effective mitotic checkpoint complex containing BubR1-Bub3-Mad2-Cdc20 (124). In addition, BUB1 can also inhibit APC/C by directly phosphorylating Cdc20 through its kinase activity (Figure 4).

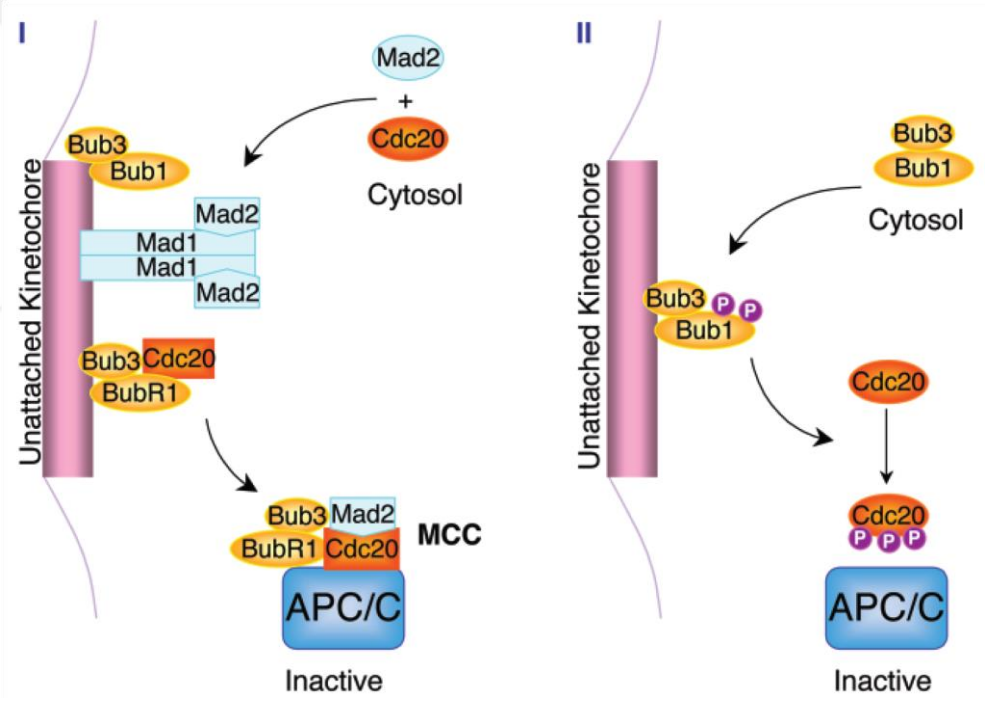


Figure 4. Spindle checkpoint control of BUB1. (Adopted from Yu and Zhanyun, 2005 (124)).

Also, BUB1 kinase phosphorylates histone H2A at threonine 120 (H2A-T120) to create binding sites for shugoshin proteins, including Shugoshin 1 (Sgo1), at the centromeres of duplicated chromosomes during mitosis (125). Sgo1 is a key player in the maintenance of sister chromatid cohesion by protecting the cohesin complex at the centromeres from being cleaved by the protease separase, which is required for the separation of sister chromatids during anaphase. BUB1-mediated phosphorylation of H2A-T120 is necessary for the proper

localization and stability of Sgo1 at the centromeres, and defects in this process can lead to chromosomal instability and aneuploidy. Therefore, BUB1 plays a critical role in ensuring accurate chromosome segregation and genomic stability by regulating the centromeric localization and function of Sgo1 (124) (Figure 5). BUB1 may also be involved in the DNA damage response (126).

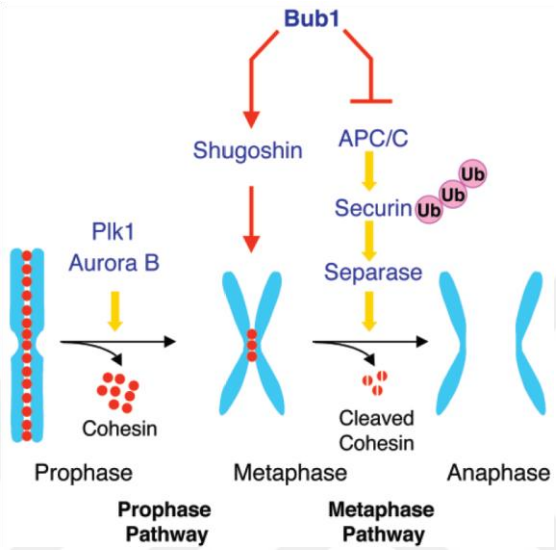


Figure 5. The noncheckpoint kinetochore control of BUB1. (Adopted from Yu and Zhanyun, 2005 (124)).

Experimental evidence suggested that high expression of *BUB1* increased cell proliferation, while silencing by shRNA decreased proliferation of liver cancer cells (127). In addition, association of *BUB1* expression with poor prognosis was also shown in breast cancer and pancreatic ductal adenocarcinoma and silencing of BUB1 not only reduced cancer stem cell potential, but also prevented xenograft formation *in vivo* (128,129). Similarly, *BUB1* expression in osteosarcoma cells was shown to be associated with poor prognosis, and silencing of BUB1 with shRNA suppressed cell proliferation and tumor growth as well as migration and invasion (130).

There are several selective BUB1 kinase inhibitors (BAY-1816032, BAY-320, BAY-524, and 2OH-BNPP1) functioning by inhibiting the catalytic domain of human BUB1 identified (125,131,132). The studies showing the effects of these inhibitors on cancer cells are limited yet promising. Inhibition of kinase activity of BUB1 using inhibitors suppressed the proliferation of bladder cancer cells *in vitro* and *in vivo* (133) as well as proliferation, migration and invasion of osteosarcoma cells (130). In addition, BUB1 inhibitor

(BAY1816032) increased the response of various cancer cells to taxane class compounds and PARP inhibitors (125).

3. MATERIALS AND METHODS

3.1. Type of the Research

This research study is descriptive and experimental.

3.2. Place and Time of Research

This study was performed in Senturk Functional Cancer Genomics Laboratory in Izmir Biomedicine and Genome Center between January 2018 and January 2023.

3.3. Research Material

3.3.1. Cell Lines and Cell Culture Consumables

Non-tumorigenic mesothelial cell line MeT-5A (CRL-9444) and malignant pleural mesothelioma cell lines NCI-H2052 (H2052) (CRL-5915), NCI-H2452 (H2452) (CRL-5946), and NCI-H28 (H28) (CRL-5820) were purchased from ATCC. HEK293T cell line was a kind gift from Dr. Nuri Ozturk (Gebze Technical University, Kocaeli, Turkey) (134).

Table 1. Cell culture consumables.

Product	Catalog no.	Vendor
RPMI-1640	21875034	Gibco
DMEM	41965039	Gibco
FBS	10500064	Gibco
FBS	SV301060.03	Hyclone
Penicillin-Streptomycin (10,000 U/ml)	15140122	Gibco
Trypsin-EDTA (0.25%), phenol red	25200-056	Gibco
TrypLE™ Express Enzyme (1X), no phenol red	12604013	Gibco
PBS (10X)	70011036	Gibco
DMSO	472301	Sigma Aldrich
Polyethilenimine (PEI)	23966	Polysciences
0.45 µl SFCA filter	431220	Corning
Polybrene	H9268-5G	Sigma Aldrich

Puromycin	ant-pr-1	Invivogen
5-layer flask	353144	Corning
Matrigel® Basement Membrane Matrix, LDEV-free	356234	Corning
Permeable Support for 24-well Plate with 8.0 µm Transparent PET Membrane, Sterile	353097	Falcon
Noble Agar, Ultrapure, Thermo Scientific	10907-100gr	Alfa Aesar
Polystyrene Round Bottom Tube w/cell-strainer cap	352235	Falcon

3.3.2. Vectors

Table 2. Vector list.

Product	**Catalog no.**	**Vendor**
psPAX2	#12260	Addgene
pMD2.G	#12259	Addgene
lentiCas9-EGFP	#63592	Addgene
lentiGuide-Hygro-dTomato	#99376	Addgene
lentiGuide-puro	#52963	Addgene
plentiCRISPRv2.1_EFS-Cas9-P2AVenus (pECPV)	Senturk, S. et al., 2017 (135)	Cloned by Serif Senturk
lentiCRISPRv2	#52961	Addgene
pHIV-ZsGreen	#18121	Addgene
pBI-GFP-Bub1-wt	#16624	Addgene
Human CRISPR Knockout Pooled Library	#73178	Addgene

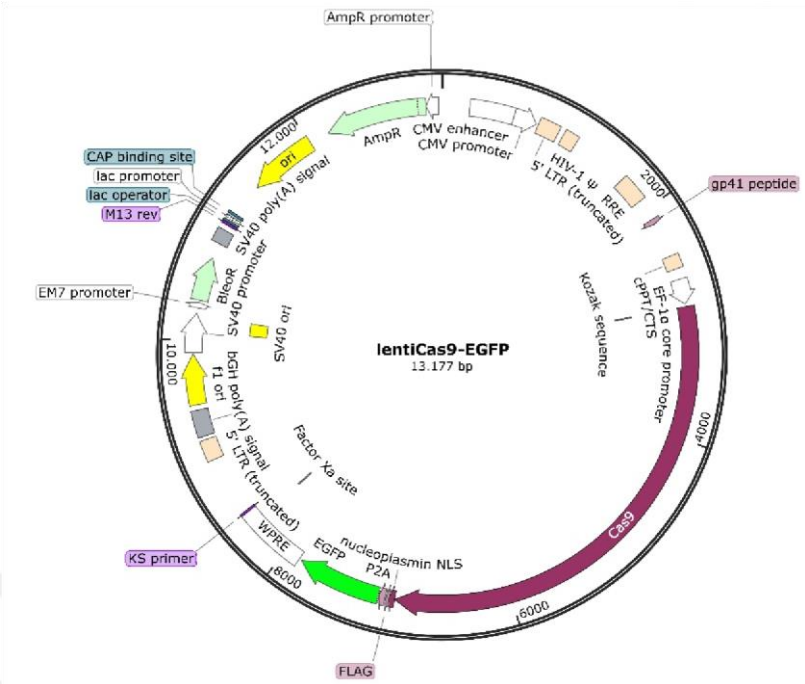


Figure 6. lentiCas9-EGFP vector map.

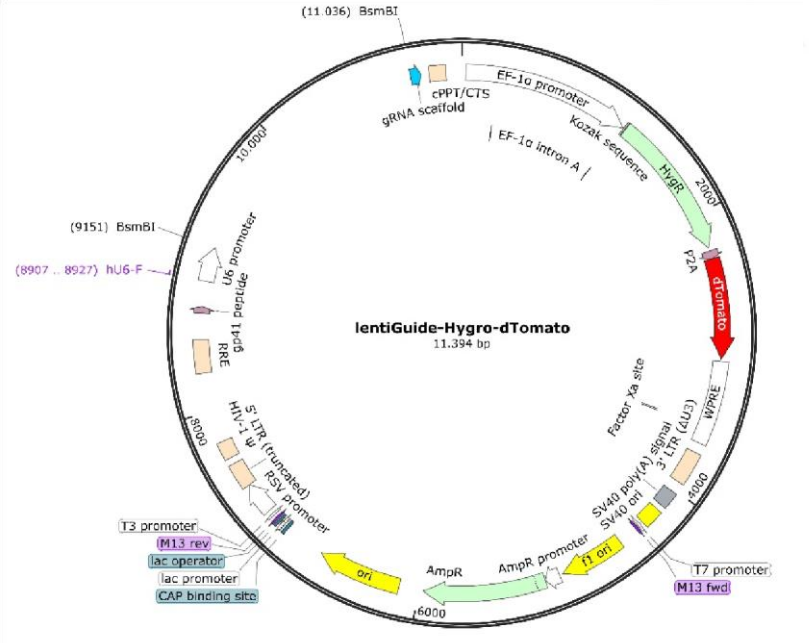


Figure 7. lentiGuide-Hygro-dTomato vector map.

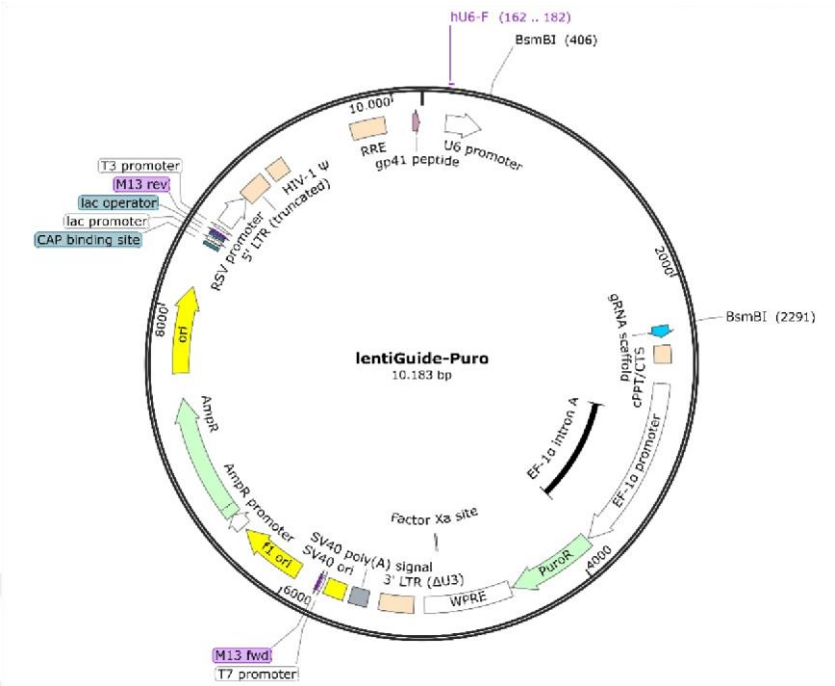


Figure 8. lentiGuide-Puro vector map.

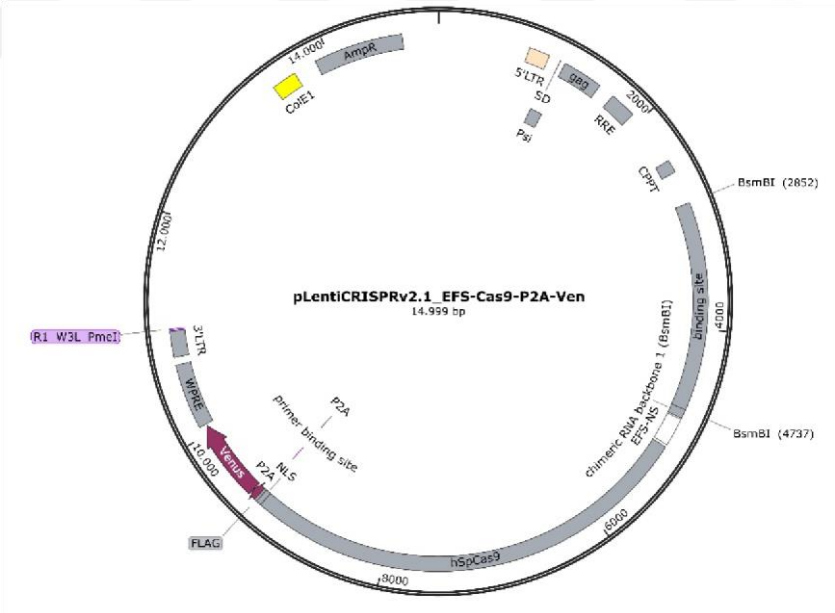


Figure 9. pECPV (plentiCRISPRv2.1_EFS-Cas9-P2A-Venus) vector map.

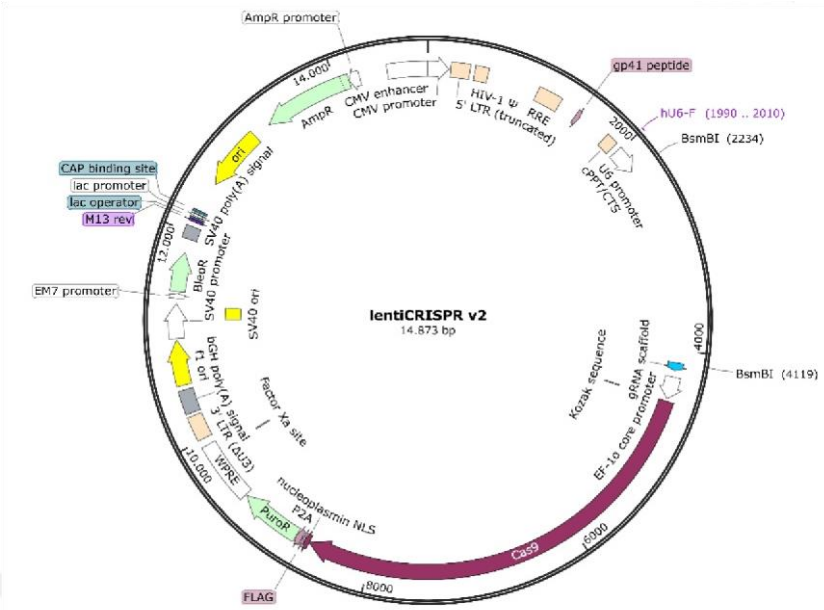


Figure 10. lentiCRISPRv2 vector map.

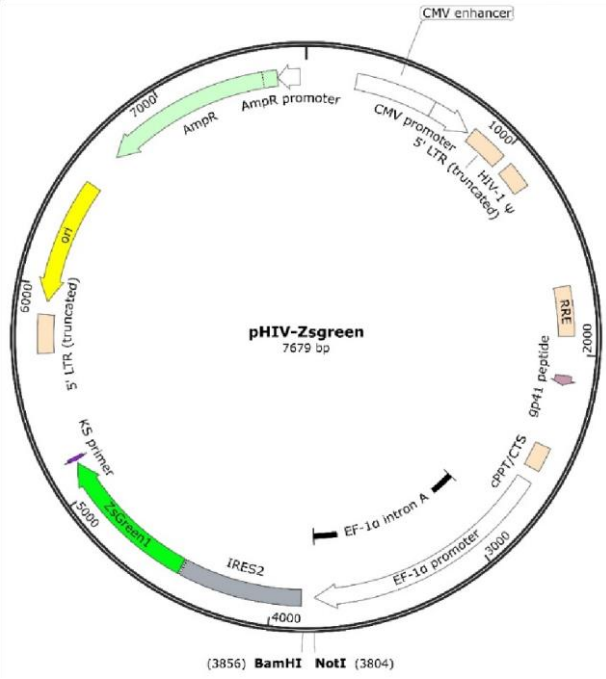


Figure 11. pHIV-ZsGreen vector map.

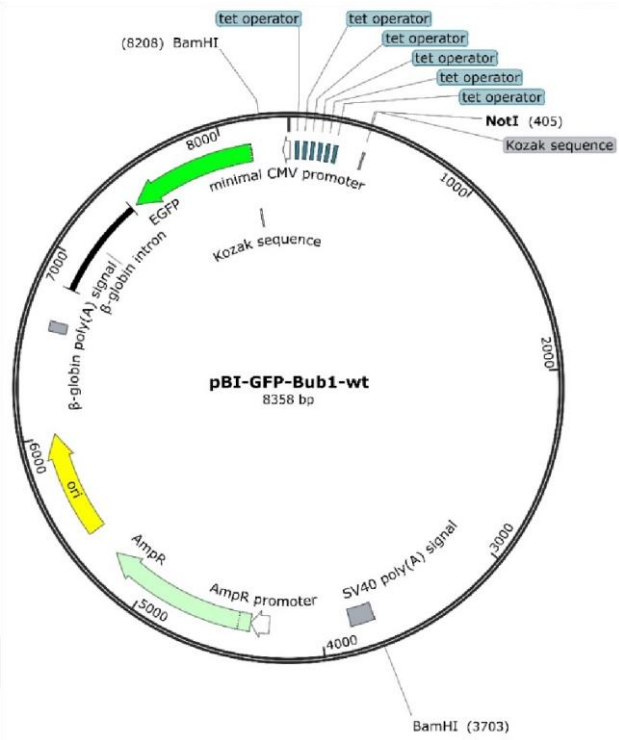


Figure 12. pBI-GFP-Bub1-wt vector map.

3.3.3. Molecular Cloning and PCR Reagents

Table 3. List of enzymes, buffers, and other PCR reagents

Product	Catalog no.	Vendor
FastDigest BsmBI	FD0454	Thermo Scientific
10X FastDigest Buffer		
Fast AP (Alkalyne phosphatase)	EF0651	Thermo Scientific
T4 DNA Ligase	M0202L	NEB
T4 PNK	M0236L	NEB
T4 Ligation Buffer (10X)	B0202L	NEB
BamHI-HF	R3136S	NEB
NotI-HF	R3189S	NEB
CutSmart Buffer	B7204S	NEB
Dream Taq Polymerase	EP0702	Thermo Scientific
10X Taq Buffer		
T7 Endonuclease I (T7EI)	M0302S	NEB
10X NEB Buffer		
Phusion Polymerase (2U/µl)	M0530S	NEB
Q5 High-Fidelity DNA Polymerase	M0491S	NEB

Q5 Reaction Buffer	B9027S	NEB
Deoxynucleotide (dNTP) Solution Mix	N0447S	NEB
NEBNext High-Fidelity 2X PCR Master Mix	M0541L	NEB

3.3.4. Oligonucleotides

Table 4. List of oligonucleotides used for gRNA cloning.

Primer	Sequence (5'-3')
Ren g.208 (gRen)_F	CACCGGTAGCGCGGTGTATTATACC
Ren g.208 (gRen)_R	AAACGGTATAATACACCGCGCTACC
RPA3 g.44_F	CACCGGATGAATTGAGCTAGCATGC
RPA3 g.44_R	AAACGCATGCTAGCTCAATTCATCC
EGFR g.60_F	CACCGTCCTCCAGAGCCCGACTCGC
EGFR g.60_R	AAACGCGAGTCGGGCTCTGGAGGAC
ATG9A g1_F	CACCGCCGTTTCCAGAACTACATGG
ATG9A g1_R	AAACCCATGTAGTTCTGGAAACGGC
VPS37A g1_F	CACCGAGCCGAAATACAGAAAGATG
VPS37A g1_R	AAACCATCTTTCTGTATTTCGGCTC
BUB1 g1_F	CACCGCAAGGAGAAGCTTATTCGTG
BUB1 g1_R	AAACCACGAATAAGCTTCTCCTTGC
BUB1 g3_F	CACCGTCAGAGAGGAATTCAAAACC
BUB1 g3_R	AAACGGTTTTGAATTCCTCTCTGAC
BUB1 g5_F	CACCGCCCGCCCAGGCAATGTACAG
BUB1 g5_R	AAACCTGTACATTGCCTGGGCGGGC
BUB1 g6_F	CACCGAACAGACTCCATGTTTGCAG
BUB1 g6_R	AAACCTGCAAACATGGAGTCTGTTC

Table 5. List of PCR primers

Primer	Sequence (5'-3')
hU6_F	GAGGGCCTATTTCCCATGATT
EGFR_F	TTGGCTCGACCTGGACATAG
EGFR_R	GGGGAAAGTGAGGGAAGAAA

Table 6. P5 and P7 primer list.

Primer	Sequence (5'-3')
P5 0 nt stagger	AATGATACGGCGACCACCGAGATCTACACTCTTTCCCTACACGAC GCTCTTCCGATCTTTGTGGAAAGGACGAAACACCG

P5 1nt stagger	AATGATACGGCGACCACCGAGATCTACACTCTTTCCCTACACGAC GCTCTTCCGATCTCTTGTGGAAAGGACGAAACACCG
P5 2 nt stagger	AATGATACGGCGACCACCGAGATCTACACTCTTTCCCTACACGAC GCTCTTCCGATCTGCTTGTGGAAAGGACGAAACACCG
P5 3 nt stagger	AATGATACGGCGACCACCGAGATCTACACTCTTTCCCTACACGAC GCTCTTCCGATCTAGCTTGTGGAAAGGACGAAACACCG
P5 4 nt stagger	AATGATACGGCGACCACCGAGATCTACACTCTTTCCCTACACGAC GCTCTTCCGATCTCAACTTGTGGAAAGGACGAAACACCG
P5 6 nt stagger	AATGATACGGCGACCACCGAGATCTACACTCTTTCCCTACACGAC GCTCTTCCGATCTTGCACCTTGTGGAAAGGACGAAACACCG
P5 7nt stagger	AATGATACGGCGACCACCGAGATCTACACTCTTTCCCTACACGAC GCTCTTCCGATCTACGCAACTTGTGGAAAGGACGAAACACCG
P5 8nt stagger	AATGATACGGCGACCACCGAGATCTACACTCTTTCCCTACACGAC GCTCTTCCGATCTGAAGACCCTTGTGGAAAGGACGAAACACCG
P7 index1	CAAGCAGAAGACGGCATACGAGATGCTGAGAAGTGACTGGAGTT CAGACGTGTGCTCTTCCGATCTTCTACTATTCTTTCCCCTGCACTGT
P7 index2	CAAGCAGAAGACGGCATACGAGATTAGTTCGGGTGACTGGAGTTC AGACGTGTGCTCTTCCGATCTTCTACTATTCTTTCCCCTGCACTGT
P7 index3	CAAGCAGAAGACGGCATACGAGATTAACTCGGGTGACTGGAGTT CAGACGTGTGCTCTTCCGATCTTCTACTATTCTTTCCCCTGCACTGT
P7 index4	CAAGCAGAAGACGGCATACGAGATTACAGAGGGTGACTGGAGTT CAGACGTGTGCTCTTCCGATCTTCTACTATTCTTTCCCCTGCACTGT
P7 index5	CAAGCAGAAGACGGCATACGAGATGCACGATTGTGACTGGAGTT CAGACGTGTGCTCTTCCGATCTTCTACTATTCTTTCCCCTGCACTGT
P7 index6	CAAGCAGAAGACGGCATACGAGATATTGGAGGGTGACTGGAGTT CAGACGTGTGCTCTTCCGATCTTCTACTATTCTTTCCCCTGCACTGT
P7 index7	CAAGCAGAAGACGGCATACGAGATATACTCGGGTGACTGGAGTT CAGACGTGTGCTCTTCCGATCTTCTACTATTCTTTCCCCTGCACTGT
P7 index8	CAAGCAGAAGACGGCATACGAGATCGGTTCGGGTGACTGGAGTT CAGACGTGTGCTCTTCCGATCTTCTACTATTCTTTCCCCTGCACTGT

3.3.5. Bacterial Strains and Reagents

Table 7. Bacterial strains.

Product	Catalog no.	Vendor
One Shot™ Stbl3™ Chemically Competent E. coli	C737303	Invitrogen
Endura™ ElectroCompetent Cells	60242-1	Lucigen

Table 8. List of reagents and consumables used for bacterial transformation studies.

Product	Catalog no.	Vendor
Tryptone	1553.03	AppliChem
Yeast extract	MB16401	Nzytech

Sodium chloride	M106404.1000	Merck
LB Broth with agar	L2897	Sigma Aldrich
Ampicillin	A0166	Sigma Aldrich
Electroporation cuvettes	1652089	BioRad
Bioassay dish	240835	ThermoFisher

3.3.6. Conventional Genomic DNA Isolation Reagents and Buffer Recipe.

Table 9. List of reagents used for DNA isolation.

Product	Catalog no.	Vendor
Tris	T1503-1KG	Sigma Aldrich
EDTA	E5134-500G	Sigma Aldrich
SDS	8170341000	Merck
RNase A	1263MG050	Neofroxx
Monarch Proteinase K	T2002	NEB

Table 10. Lysis buffer recipe.

Reagent	Stock	Working	5 ml
Tris-Cl pH 8	0.8 M	10 mM	312.5 µl
EDTA pH 8	0.5 M	0.1 M	5 ml
SDS	125 mg	0.5%	25 µl
Proteinase K	20 mg/ml	100 µg/ml	250 µl
RNase A	50 mg/ml	20 µg/ml	150 µl
dH_2O			Up to 25 ml

3.3.7. Western Blot Reagents, Buffer Recipes, and Antibodies

Table 11. List of reagents used for RIPA buffer preparation.

Product	Catalog no.	Vendor
Triton X-100	T8787-100ml	Sigma Aldrich
Na deoxycholate	30970-25G	Sigma Aldrich
SDS	8170341000	Merck
Tris	T1503-1KG	Sigma Aldrich
EDTA	E5134-500G	Sigma Aldrich
EGTA	E3889-10G	Sigma Aldrich
β-glycerolphosphate	50020-100G	Sigma Aldrich
NaF	S6776-100G	Sigma Aldrich
PMSF	LSG36978-5G	Sigma Aldrich

Na Vanadate	sc-3540A	Santa Cruz
Leupeptin	1273-25mg	Neofroxx
Aprotinin	1278-25mg	Neofroxx
Pepstatin	P5318-5MG	Sigma Aldrich

Table 12. Recipe of RIPA buffer.

Reagent	Stock	Working	5 ml
Triton X-100	10%	1%	500 µl
Na deoxycholate	10%	0.5%	250 µl
SDS	20%	0.1% (mild)	25 µl
Tris-Cl pH 7.4	1 M	50 mM	250 µl
NaCl	5 M	150 mM	150 µl
EDTA pH 8	0.5 M	1 mM	50 µl
EGTA	0.1 M	1 mM	50 µl
β-glycerolphosphate	0.5 M	10 mM	100 µl
NaF	0.5 M	10 mM	200 µl
PMSF	0.1 M	1 mM	50 µl
Na Vanadate	0.1 M	1 mM	50 µl
Leupeptin	5 mg/ml	10 µg/ml	10 µl
Aprotinin	5 mg/ml	10 µg/ml	10 µl
Pepstatin	1 mg/ml	10 µg/ml	50 µl
dH_2O		Up to 5 ml	

Table 13. List of reagents used for SDS-PAGE gel preparation.

Product	Catalog no.	Vendor
ProtoGel (30%)	EC-890	National Diagnostics
Protogel stacking buffer	EC-893	National Diagnostics
APS	1610GR100	BioFroxx
TEMED	T22500-100	Sigma Aldrich

Table 14. 5 ml SDS-PAGE separating gel recipe.

Component	6%	8%	10%	12%	15%
Protogel (ml)	1	1.35	1.65	2	2.5
dH_2O (ml)	3.375	3.025	2.725	2.375	1.875
Main gel buffer (ml)	0.625				
10% APS (µl)	25				

TEMED (µl)	5

Table 15. Stacking gel recipe

Component	2 ml	3 ml	4 ml	5 ml	6 ml	7 ml	8 ml	9 ml	10 ml
Protogel (ml)	0.25	0.375	0.5	0.625	0.75	0.875	1	1.125	1.25
dH_2O (ml)	1.25	1.875	2.5	3.125	3.75	4.375	5	5.625	6.25
Protogel stacking buffer	0.5	0.75	1	1.25	1.5	1.75	2	2.25	2.5
10% APS (µl)	12.5	18.75	25	31.25	37.5	43.75	50	56.25	62.5
TEMED (µl)	2.5	3.75	5	6.25	7.5	8.75	10	11.25	12.5

Table 16. Buffer recipes.

Buffer	Component	Amount
Main gel buffer	Tris	72.684 g
	SDS 10%	16 ml
	dH_2O	Up to 200 ml
	pH	8.8
Running buffer (10X)	Tris	250 mM
	SDS	1%
	Glycine	1.9 M
	dH_2O	Up to 1 L
	pH	~8.3
Transfer buffer (10X)	Tris	250 mM
	Glycine	1.9 M
	dH_2O	Up to 1 L
	pH	~8.3
	Methanol	20%
TBS (10X)	Tris	24 g
	NaCl	88 g
	dH_2O	Up to 1 L
	pH	7.6

Table 17. Other reagents and consumables.

Product	Catalog no.	Vendor
BLUeye Prestained Protein Ladder	PM007-0500	GeneDirex
Skim Milk Powder	70166-500G	Sigma Aldrich

Albumin Fraction V (pH 7.0)	1126GR100	BioFroxx
Tween-20	BP337-100	Fisher BioReagents
Ponceau S	P3504-10G	Sigma Aldrich
Acetic acid	27225-2.5L-R	Sigma Aldrich
Nitrocellulose membrane (0.2 µl)	GE10600004	GE Healthcare

Table 18. Antibody list.

Product	Working Dilution	Catalog no.	Vendor
BUB1	1/1000	ab195268	Abcam
FlagMonoclonal ANTI-FLAG® M2 antibody produced in mouse	1/1000	F1804	Sigma Aldrich
β-actin	1/1000	3700T	Cell Signaling Technology
α-tubulin	1/1000	SC-32293	SantaCruz
Anti-mouse IgG (H+L) (DyLight™ 680 Conjugate)	1/10000	5470P	Cell Signaling Technology
Anti-rabbit IgG (H+L) (DyLight™ 800 4X PEG Conjugate)	1/20000	5151P	Cell Signaling Technology

3.3.8. Bromodeoxyuridine (BrdU) Incorporation Assay Reagents

Table 19. Reagent list used for BrdU assay.

Product	Catalog no.	Vendor
5-Bromo-2'-deoxyuridine	B5002	Sigma Aldrich
Hydrocloric acid fuming 37%	1003172500	Merck
BrdU (Bu20a) Mouse mAb	5292	Cell Signalling Technology
Dnk pAb to Mouse IgG Alexa Flour 488	ab150105	Abcam
Anti-mouse IgG (H+L) Alexa Fluor® 594 Conjugate	8890S	Cell Signalling Technology
DAPI	1322MG005	Neofroxx
Microscope Cover Glasses 18 mm	111580	Marienfeld
Microscope Cover Glasses 12 mm	111520	Marienfeld

3.3.9. Senescence-Associated β-galactosidase (SA-β-Gal) Assay Reagents

Table 20. Reagent list used for SA-β-Gal Assay.

Product	Catalog no.	Vendor
Glutardialdehyde Solution	820603.1000	Merck
Formaldehyde solution	F1635	Honeywell
Citric Acid Monohydrate	9100461000	Isolab
Sodium phosphate dibasic dihydrate	4272	Sigma
Potassium hexacyanoferrate (II) trihydrate (ferro)	LC-10061.1	Neofroxx
Potassium hexacyanoferrate (III) (ferri)	LC-6423.3	Neofroxx
Sodium Chloride	1064041000	Merck
Magnesium chloride hexahydrate	LC-5041.4	Neofroxx
PBS (1X)	10010-015	Gibco
X-Gal	1168GR001	Neofroxx

Table 21. Solution recipes.

Buffer	Component	Amount
200 mM citric acid	Citric acid monohydrate	1.92 g
	dH_2O	50 ml
1 M Sodium phosphate dibasic dihydrate	Sodium phosphate dibasic dihydrate	8.9 g
	dH_2O	50 ml
	Citric acid (0.2 M)	7.37 ml
200 mM citric acid/Na phosphate buffer	Sodium phosphate dibasic dehydrate (1 M)	5.052 ml
	dH_2O	27.578 ml
1 M NaH_2PO_4	NaH_2PO_4	6 g
	dH_2O	50 ml
100 mM potassium ferrocyanide	Potassium hexacyanoferrate (II) trihydrate	1.69 g
	dH_2O	40 ml
100 mM potassium ferricyanide	Potassium hexacyanoferrate (III) (ferri)	1.317 g
	dH_2O	40 ml
2M NaCl	NaCl	2.92 g
	dH_2O	50 ml
100 mM $MgCl_2$	MgCl	0.48 g
	dH_2O	50 ml
40 mg/ml X-gal	X-gal	5 mg
	Dimethyl formamide	125 µl
Fixative Solution (10 ml)	Glutardialdehyde solution (25%)	80 µl
	Formaldehyde (37%)	500 µl

	PBS (1X)	9420 µl
Staining Solution (10 ml)	Citric acid/Na phosphate buffer (200 mM)	2 ml
	Potassium ferrocyanide (100 mM)	500 µl
	Potassium ferricyanide (100 mM)	500 µl
	NaCl (2 M)	750 µl
	$MgCl_2$ (100 mM)	200 µl
	X-gal (40 mg/ml)	250 µl
	dH_2O	5.8 ml

Table 22. List of other reagents.

Product	Catalog no.	Vendor
Gel Loading Dye, Purple (6X)	B7024S	NEB
1 kb DNA Ladder	N3232S	New England Biolabs
100 bp DNA Ladder	G193	ABM
Crystal violet	C6158	Sigma Aldrich
MTT	1334GR001	Neofroxx
Propidium iodide	81845	Sigma Aldrich
BAY-1816032	HY-103020	MedChemExpress

Table 23. Kits.

Product	Catalog no.	Vendor
NucleoSpin Gel and PCR Clean-up kit	740609.50	MN
NucleoSpin® Plasmid Mini Kit	740588.50	MN
NucleoBond Xtra Midi Plus Kit	740412.10	MN
EZ-10 Spin Column Plasmid DNA Miniprep Kit	BS614.0612R0C	BioBasic
HiSpeed Plasmid Maxi Kit	12662	Qiagen
Mycoplasma PCR Detection Kit	G238	ABM
QIAamp Blood Maxi Kit	51192	Qiagen
Pierce™ BCA Protein Assay Kit	23227	ThermoFisher
FITC Annexin V Apoptosis Detection Kit with PI	6 40914	Biolegend

Table 24. List of devices and softwares.

Device/Software	Vendor
BD LSRFortessa™ flow cytometer	BD Biosciences
BD FACSAria™ III Cell Sorter	BD Biosciences
FlowJo v10.8.0 software	
CKX41 Inverted microscope	Olympus

BX61 Fully Motorized Fluorescence Microscope	Olympus
ImageJ 1.53e software	
GraphPad Prism 8.0 software	
Multiskan™ GO Microplate Spectrophotometer	ThermoFisher
LI-COR Odyssey Imaging System	LI-COR
Nanodrop	

3.4. Methods

3.4.1. Cell Culture

MeT-5A, H2052, H2452, and H28 cell lines were cultured in RPMI-1640 medium supplemented with 10% fetal bovine serum (FBS) and 1% penicillin/streptomycin. HEK293T cell line was cultured in high glucose Dulbecco's Modified Eagle's Medium (DMEM) supplemented with 10% FBS and 1% penicillin/streptomycin. All cell lines were maintained in a humidified incubator at 37°C with 5% CO_2. Regular mycoplasma testing was performed with Mycoplasma PCR Detection Kit.

3.4.2. Construction of gRNA, and Overexpression Vectors

3.4.2.1.gRNA Vector Construction

Digestion and Dephosphorylation of Plasmids:

Plasmid	5 µg
FastDigest BsmBI	3 µl
Fast AP (Alkalyne phosphatase)	3 µl
10X FastDigest Buffer	6 µl
dH_2O	Up to 60 µl

Plasmid was digested at 37°C for 2 h following the protocol provided above. Digested plasmids were run on 0.8% agarose gel and extracted from the gel by the NucleoSpin Gel and PCR Clean-up kit.

Phosphorylation and Annealing of Oligos:

Oligo1 (100 µM	1 µl

Oligo2 (100 µM)	1 µl
10X T4 ligation buffer	1 µl
T4 PNK	0.5 µl
dH_2O	Up to 10 µl

Thermocycler parameters:

37°C 30 min

95°C 5 min and ramp down to 25°C at 5°C/min

Forward and reverse gRNA sequences were phosphorylated and annealed following the protocol and conditions provided above. Annealed products were diluted 1/20 to be used in the ligation step.

Ligation:

BsmBI digested plasmid	50 ng
Diluted oligo duplex	2 µl
T4 ligation buffer	1 µl
T4 ligase	1 µl
dH_2O	up to 10 µl

Digested plasmids were ligated with the annealed gRNA duplexes at 25°C for 2 h following the protocol provided above.

3.4.2.2.Overexpression Vector Construction

BUB1 coding sequence (CDS) was extracted from pBI-GFP-Bub1-wt and cloned into pHIV-Zsgreen lentiviral overexpression vector following the protocol provided below.

Digestion and Dephosphorylation of Plasmids:

Plasmid	2 µg
BamHI	0.4 µl

NotI	0.4 µl
CutSmart buffer	2 µl
dH_2O	up to 20 µl

Plasmid was digested at 37°C for 2 h following the protocol provided above. Digested plasmids were run on 1.2% agarose gel and extracted from the gel by the NucleoSpin Gel and PCR Clean-up kit.

Ligation:

Digested plasmid	50 ng
Insert	64.8 ng
T4 ligation buffer	1 µl
T4 ligase	0.5 µl
dH_2O	up to 10 µl

BamHI and NotI digested BUB1 CDS fragment and pHIV-Zsgreen vector were ligated at 25˚C for 2 h, following the protocol provided above. Insert and vector ratio to be used was calculated according to the below formula with the vector being 50 ng in the reaction: $3x(\frac{}{}\ xvector\quad mass)$

3.4.3. Transformation

In total 50 ng of plasmid or total amount of ligation product was added onto 50 µl of Stbl3 competent E. coli strain and incubated on ice for 30 min. Bacteria-plasmid mixture was then incubated at 42˚C water bath for 90 s and immediately put on ice for 2 min. After heat-shock, 1 ml of LB medium was added onto the mixture and incubated at 37˚C for 1 h for recovery. After ~30 s of centrifugation at 11.000 *g* supernatants were discarded while keeping ~100 µl to resuspend the pellet. Then, samples were spread on pre-warmed LB agar plates with 100 µg/ml Ampicillin and incubated overnight (16-18 h) at 37°C.

3.4.4. Colony PCR

Colony PCR was performed to confirm gRNA cloning efficiency following the protocol provided below. Bacterial colonies selected with pipette tips were used as template.

10X Taq Buffer	2 µl
dNTPs	0.4 µl
Forward primer (U6)	0.4 µl
Reverse primer (gRNA-reverse)	0.4 µl
Taq polymerase	0.1 µl
dH_2O	up to 10 µl

Thermocycler parameters:

Step	Temperature	Time	Number of Cycles
Initial denaturation	94°C	5 min	1
Denaturation	94°C	30 s	30
Annealing	60°C	30 s	
Extension	72°C	2 min	
Final extension	72°C	5 min	1

PCR products were run on 2% agarose gel.

3.4.5. Mini and Midi Culture and Plasmid Isolation

For mini culture, colonies were picked and grown in 5 ml LB medium with 100 µg/ml Ampicillin at 37°C, 225 rpm overnight (16-18 h). MN NucleoSpin® Plasmid kit or Bio Basic EZ-10 Spin Column Plasmid DNA Miniprep Kit protocol was followed.

For midi culture, colonies grown in mini culture were transferred into 150 ml LB with 100 µg/ml Ampicillin and incubated at 37°C, 225 rpm overnight (16-18 h). NucleoBond Xtra Midi Plus Kit protocol was followed.

3.4.6. Stable Cas9 Expressing Monoclonal Cell Line Generation

Stably Cas9 expressing cell lines were obtained by virally transducing cells with lentiCas9-EGFP and selecting the GFP positive cells via fluorescence activated cell sorting (FACS). Cas9 protein expression was verified by Western blot analysis.

In order to obtain a single cell clone, one cell should be seeded per well. To achieve this, cells were diluted at a 0.5 cells/well ratio and manually seeded into 96-well plates. Then, the wells were scored for single cell seeding and allowed to grow in conditioned media (collected from each corresponding parental cell line) containing 20% FBS to accelerate colony formation. Single cells were allowed to grown by transferring into larger growth medium and 11-13 clonal sublines were obtained for each cell line.

Functionality of Cas9 was verified by two different strategies. First, competititon assay was performed. Accordingly, the Cas9-free plasmid lentiGuide-Hygro-dTomato was digested with the BsmBI enzyme and oligos with BsmBI matching sequences at the ends, targeting the Renilla luciferase gene used as negative control and RPA3 gene used as positive control, were cloned (Table 4). After ligation, plasmids were transformed into Stbl3 bacteria. Colonies containing gRNA sequences were detected by colony PCR. After plasmid isolation 2 samples were selected and gRNA cloning was confirmed by Sanger sequencing. MeT-5A-Cas9, H2052Cas9, H2452-Cas9 and H28-Cas9 cells were infected with virus particles packaged from plasmid samples confirmed by sequencing, and the percentage of Tomato positive cells was measured every 4 days by flow cytometry for 12 days.

Second, the Cas9-free plasmid lentiGuide-puro was digested with the BsmBI enzyme and oligos with BsmBI matching sequences at the ends targeting the Renilla luciferase gene used as negative control and EGFR gene used as positive control were cloned (Table 4). Plasmid samples were isolated as described above and gRNA cloning was confirmed by Sanger sequencing. MeT-5A-Cas9, H2052-Cas9, H2452-Cas9 and H28-Cas9 cells were infected with virus particles packaged from plasmid samples confirmed by sequencing for 48 h and selected with puromycin for 72 h. After selection, DNA isolation was performed, and the EGFR gene region was amplified with the primers given in Table 5 as described below. Obtained bands were verified by agarose gel electrophoresis and extracted from the gel. Extracted PCR products were digested with T7 Endonuclease I (T7EI) enzyme as described under the relevant section.

5X High Fidelity Buffer	4 µl
Phusion Polymerase (2U/µl)	0.1 µl
10 mM dNTPs	0.4 µl

Forward primer	0.8 µl
Reverse primer	0.8 µl
DMSO	0.6 µl
Template	200 ng
dH_2O	up to 20 µl

Thermocycler parameters:

Step	Temperature	Time	Number of Cycles
Initial denaturation	98°C	30 s	1
Denaturation	98°C	10 s	35
Annealing	72°C	20 s	
Extension	72°C	20 s	
Final extension	72°C	10 min	1

3.4.7. T7 Endonuclease I (T7E1) Assay

10X NEB Buffer	2 µl
Template	200 ng
dH_2O	up to 19 µl

Thermocycler parameters:

95˚C	5 min
95˚C	85˚C -2˚C /s
85˚C	25˚C -0.1˚C /s

T7E1 was added onto the reaction as 0.5 µl and incubated at 37˚C for 30 min (136). PCR products were run on 2% agarose gel.

3.4.8. Conventional Genomic DNA Isolation

Cells were collected by trypsinization and centrifuged at 1500 rpm for 1.5 min. Supernatant was discarded, pellets were resuspended in 500 µl lysis buffer and incubated overnight (16-18 h) at 55°C. Then, 250 µl 6M NaCl was added onto samples and centrifuged at max speed for 20 min. The supernatant was transferred into a new microcentrifuge tube. Isopropanol (0.7-fold of the sample volume) was added onto samples and vortexed vigorously. Samples were centrifuged for 15 min at max speed and supernatant was discarded. Pellets were resuspended in 500 µl 100% ethanol and vortexed. After centrifugation at max speed for 5 min supernatant was discarded. Finally, 500 µl 70% ethanol was added onto samples and vortexed again. After final centrifugation at max speed for 5 min, supernatant was discarded, and pellets were dissolved in 75 µl pre-heated (55°C) Tris. DNA concentration was measured by nanodrop.

3.4.9. Pooled Library Amplification

Human CRISPR Knockout Pooled Library (Brunello) was purchased from Addgene and amplified according to the recommended protocol by using Endura™ ElectroCompetent Cells. In detail, two tubes of Endura cells were thawed on ice and brought together in one tube in total 100 µl. 8 µl of library was added onto bacteria. Bacteria-library mixtures were transferred into 4 pre-cooled electroporation cuvettes (as 30, 30, 30, and 46 µl because bacteria amount was higher than 100 µl) and electroporated in EC1 (6 milisecond, 1.8 kV) program. Bacteriaplasmid mixtures were collected into 14 ml tube by directly adding pre-warmed 1 ml recovery medium. Up to 10 ml recovery medium was added and 5 ml was distributed to each of two 14 ml tubes. Tubes were incubated at 37˚C, 250 rpm for 1 h. Meanwhile, 100 mm agar plates and bioassay dishes, 241x241x20 mm dishes that are used to provide high volume of culturing, were pre-warmed. Then, 2.5 ml of cells were plated on each of the 4 bioassays and distributed evenly with biospreaders. Besides, bacteria culture was spreaded onto 100 mm agar plates as 1/500, 1/10000, and 1/40000 dilutions to calculate colony formation unit (CFU). Cultures were incubated at 32°C for 18 h (137,138).

Bioassay dishes were scraped by using biospreader with 20 mL cold LB per plate and bacteria from two dishes were collected into a 50 ml conical tubes kept on ice. Tubes were centrifuged

at 3900 rpm for 30 min. Supernatants were discarded and pellets were weighed. Total weight was 7.69 g (3.82 g and 3.87 g). Each conical tube was a single Maxiprep. HiSpeed Plasmid Maxi Kit protocol (139) was used for plasmid isolation.

* RNase A solution was added to Buffer P1.

* LyseBlue® reagent was added to Buffer P1 at a ratio of 1:1000.

* Buffer P3 was prechilled to 4°C.

1) Bacterial pellets were resuspended homogeneously in 10 ml Buffer P1.
2) 10 ml Buffer P2 was added into each tube and mixed by inverting 4-6 times, and incubated at room temperature for 5 min. 4 ml more Buffer P2 was added into each tube.
3) During the incubation, the caps were screwed onto the outlet nozzle of the QIAfilter Cartridge. The QIAfilter Cartridges were placed into a convenient tube.
4) 10 ml prechilled Buffer P3 was added into each tube and mixed thoroughly by inverting until lysates were completely colorless. 4 ml more Buffer P3 was added into each tube.
5) The lysates were poured into the barrel of the QIAfilter Cartridge and incubated at room temperature for 10 min.
6) HiSpeed Tips were equilibrated with 10 ml Buffer QBT, allowing it to enter the resin.
7) The caps were removed from the QIAfilter Cartridge outlet nozzle. The plungers were gently inserted into the QIAfilter Cartridge, and the cell lysates were filtered into the equilibrated HiSpeed Tip.
8) After the lysate has entered, the HiSpeed Tips were washed with 60 ml Buffer QC.
9) DNA was eluted with 15 ml Buffer QF.
10) DNA was precipated by adding 10.5 ml isopropanol, mixed, and incubated for 5 min.
11) During the incubation, the plungers were removed from a 30 ml syringe and the QIAprecipitator Modules were attached onto the outlet nozzle.
12) The QIAprecipitators were placed over a waste bottle, the eluate-isopropanol mixtures were transferred into the syringe, and the plungers were inserted. The eluate–isopropanol mixtures were filtered through the QIAprecipitator using constant pressure.

13) The QIAprecipitators were removed from the syringe and the plungers were pulled out. The QIAprecipitators reattached and 2 ml 70% ethanol was added to each syringe. The DNA was washed by inserting the plunger and pressing the ethanol through the QIAprecipitator.

14) The QIAprecipitators were removed from the syringe and the plungers were pulled out. The QIAprecipitators were attached again, the plungers were inserted, and the membranes were dried by pressing air through the QIAprecipitator forcefully. This step was repeated several times.

15) The outlet nozzle of the QIAprecipitators were dried with adsorbent paper.

16) The plungers from a new 5 ml syringe were removed, the QIAprecipitators were attached, and the outlets were holded over a 1.5 ml collection tube. 1 ml Buffer TE was added to each 5 ml syringe. The plungers were inserted and the DNA from two tubes was eluted into the same collection tube using constant pressure.

17) The QIAprecipitator was removed from the 5 ml syringe, the plunger was pulled out and the QIAprecipitator was re-attached to the 5 ml syringe.

18) The eluate from step 17 was transferred to the 5 ml syringe and eluted for a second time into the same 1.5 ml tube. DNA concentration was measured.

3.4.10. NGS Confirmation of Amplified Library

3.4.10.1. Preparation of Sequencing Library

PCR was performed to amplify the gRNA region over the library we amplified in our laboratory and the original library bought from Addgene following the protocol and conditions provided below. To this aim, primers required for the preparation of the sequence library were designed. These primers enable the creation of a ready-to-run deep sequencing PCR-library thanks to the additional sequences they carry (P5 and P7). In order to preserve sequence diversity in the PCR-library to be loaded into the flow cell in the Illumina device, a P5 primer mix containing stagger regions of different lengths is required. For this, at least 8 primers are recommended. In addition, index sequences are used on the P7 primer, allowing different samples to be run in the same flow cell. Primer sequences used in the amplification of sequence library are listed in the Table 6 (137,138) (P5 mix and P1 index1, and P7 index2 were used for library preparation). Mastermix was prepared as 100 µl and divided into 4 tubes as 25 µl. PCR amplified gRNA-

targeted regions were extracted from agarose gel. Isolated libraries were sequenced on HiSeq2500 system (Illumina, San Diego, CA, USA).

5X High Fidelity Buffer	4 µl
Phusion Polymerase (2U/µl)	0.25 µl
10mM dNTPs	0.5 µl
DMSO	0.75 µl
P5 primer (10 µM)	1 µl
P7 primer (10 µM)	1 µl
Template	10 ng
Nuclease-free H_2O	up to 25 µl

Thermocycler parameters:

Step	Temperature	Time	Number of Cycles
Initial denaturation	95°C	1 min	1
Denaturation	95°C	30 s	28
Annealing	53°C	30 s	
Extension	72°C	30 s	
Final extension	72°C	10 min	1

3.4.10.2. Analysis of NGS Results

Results from NGS were analyzed with the code count_spacers.py provided by Joung et al. (140) by using the paramaters KEY_REGION_START = 10 #start index of key region, KEY_REGION_END = 55 #end index of key region, and KEY = "CGAAACACC and gRNA representation was determined. After running the count_spacers.py code, the distribution of spacer sequences in the NGS results was written to an output file (library_count.csv), with the

guide spacer sequence in the first column and the read count in the second column. Finally, statistical data was generated by the code as output file.

3.4.11. Puromycin Dose Curve

Cells were seeded in a 96 well plate. After 24 h, puromycin was added onto each well in the range of 0.5-10 µg/ml as 1:2 serial dilutions. After 72 h treatment, medium was removed, cells were washed with 1X PBS and fixed with 3.7% formaldehyde (vol/vol) for 20 min, and then stained with crystal violet solution (0.5% wt/vol crystal violet powder dissolved in 20% glacial acetic acid) at room temperature for 40 min. After rinsing the stained plates in a stream of tap water, the plates were air-dried at room temperature. High-resolution images of the plates were obtained by using The Odyssey CLx Imaging System (LI-COR).

3.4.12. Virus Production and Infection

3.4.12.1. Virus Production

HEK293T cells were seeded in a 6 well plate to be ~80% confluent after 24 h and cotransfected with target vector, psPAX2, and pMD2.G using polyethylenimine (PEI). In detail, target vector, psPAX2, and pMD2.G were mixed in 200 µl 1xPBS at ratio of 4:2:1 to be 6 µg total DNA. In another tube, PEI (1 mg/ml) was added onto 200 µl 1xPBS at 1:5 DNA:PEI ratio. DNA and PEI mixtures were mixed and incubated for 20 min at room temperature. Medium of HEK293T cells were discarded and fresh medium was added. DNA-PEI mixture was added onto cells counterclockwise drop by drop. The supernatant was harvested after 48 hours and filtered through a 0.45 µm SFCA filter. The virus particles were then aliquoted and frozen at 80°C.

3.4.12.2. Virus Infection

Cells were seeded to be ~50-60% confluent after 24 h. Medium containing viral particles was diluted in the culture medium containing polybrene at a final concentration of 8 µg/ml and added onto cells. Cells were infected for 48 h and selected by puromycin treatment or

fluorescence associated cell sorting by BD FACS AriaIII depending on the selection marker the plasmid contains.

3.4.12.3. Virus Production and MOI Calculation with Brunello Library

In total $80x10^6$ HEK293T cells were seeded in eight T75 flasks at ~80% confluency and co-transfected with 33 µg Brunello, 16.5 µg psPAX2, and 8.25 µg pMD2.G using PEI at 1:5 DNA:PEI ratio and incubated for 20 min at room temperature. DNA:PEI mixture was added into 120 ml fresh DMEM. The medium of HEK293T cells was discarded and fresh DMEM w/ DNA:PEI mixture was divided into 8 flasks. The supernatants were harvested after 48 and 72 h and filtered through a 0.45 µm SFCA filter. The virus particles were then aliquoted and frozen at -80°C.

Next, $150x10^3$ cells seeded into 6 well plates were infected with different dilutions (1/16, 1/32, 1/64, and 1/128) of library virus particles. After 48 h of infection, cell were selected with specified doses of puromycin for 72 h and counted. Doses or dose ranges providing 25-30% infection rate were determined and tested on midi scale (100 mm dish).

3.4.13. Doubling Time Calculation

MeT-5A-Cas9, H2052-Cas9, H2452-Cas9, and H28-Cas9 cells were seeded into 12 wells of 24 well plate as $25x10^3$, $1x10^4$, $1x10^4$, and $25x10^3$ respectively. Two wells of each cell line were trypsinized and counted every 24 h for 6 days.

3.4.14. Whole Genome CRISPR-Cas9 Screen and Preparation of Sequencing Library

Since the aim of this project is to identify MPM essential genes, MeT-5A, a nontumorigenic mesothelial cell line was used in parallel to H2052, H2452 and H28 cell lines, which are the frequently used MPM cell lines in the literature, for the whole genome CRISPR screen in order to exclude common essential genes. To achieve 250X gRNA representation after puromycin selection, ~$19.4x10^6$ (77441x250) cells need to be collected for the DNA isolation step. For this, the number of cells to be seeded before infection was calculated as $120x10^6$.

3.4.14.1. MeT-5A Cell Line

A total of $120x10^6$ MeT-5A-Cas9 cells were divided into three 5-layer flasks and seeded. Cells were infected with the gRNA lentivirus library at 1/128 dilution. After 48 h of infection, cells were selected with 2 μg/ml puromycin for 72 h. After selection, cells from three flasks were pooled, counted and in total $130x10^6$ cells were obtained. Cells were divided into four groups. $32x10^6$ cells were seeded in each 5-layer flasks as triplicates and $32x10^6$ cells were stored as pellet at -80°C. Thus, screen was continued with 413X representation for MeT-5ACas9 cells. When the cells became confluent, cells in each flask were counted and $32x10^6$ cells were seeded again in each passage. At the end of 14 duplication times (17 days), cells were counted and $63x10^6$, $61x10^6$ and $54x10^6$ cells were obtained for Groups 1, 2 and 3, respectively. All of the collected cells were centrifuged by transferring $32x10^6$ cells for each group into another tube and stored at -80°C.

3.4.14.2. H2052 Cell Line

A total of $120x10^6$ H2052-Cas9 cells were divided into six 5-layer flasks due to the size of these cells and seeded. Cells were infected with the gRNA lentivirus library at 1/48 dilution. After 48 h of infection, cells were selected with 3 μg/ml puromycin for 72 h. After selection, cells from six flasks were pooled, counted and in total $147x10^6$ cells were obtained. Cells were divided into four groups. $36x10^6$ cells were seeded in each 5-layer flasks as triplicates (six flasks in total -two flasks for each group-) and $36x10^6$ cells were stored as pellet at -80°C. Thus, screen was continued with 476X representation for H2052-Cas9 cells. When the cells became confluent, cells in each flask were counted and $36x10^6$ cells were seeded again in each passage. At the end of 14 duplication times (16 days), cells were counted and $73x10^6$, $76x10^6$ and $76x10^6$ cells were obtained for Groups 1, 2 and 3, respectively. All of the collected cells were centrifuged by transferring $36x10^6$ cells for each group into another tube and stored at -80°C.

3.4.14.3. H2452 Cell Line

A total of $120x10^6$ H2452-Cas9 cells were divided into three 5-layer flasks and seeded. Cells were infected with the gRNA lentivirus library at 1/24 dilution. After 48 h of infection, cells were selected with 3 μg/ml puromycin for 72 h. After selection, cells from three flasks were pooled, counted and in total $80x10^6$ cells were obtained. Cells were divided into four groups.

$20x10^6$ cells were seeded in each 5-layer flasks as triplicates and $20x10^6$ cells were stored as pellet at -80°C. Thus, screen was continued with 262X representation for H2452-Cas9 cells. When the cells became confluent, cells in each flask were counted and $20x10^6$ cells were seeded again in each passage. At the end of 14 duplication times (19 days), cells were counted and $49x10^6$, $47x10^6$ and $51x10^6$ cells were obtained for Groups 1, 2 and 3, respectively. All the collected cells were centrifuged by transferring $20x10^6$ cells for each group into another tube and stored at -80°C.

3.4.14.4. H28 Cell Line

A total of $120x10^6$ H28-Cas9 cells were divided into three 5-layer flasks and seeded. Cells were infected with the gRNA lentivirus library at 1/128 dilution. After 48 h of infection, cells were selected with 2 µg/ml puromycin for 72 h. After selection, cells from three flasks were pooled, counted and in total $230x10^6$ cells were obtained. Cells were divided into four groups. $50x10^6$ cells were seeded in each 5-layer flasks as triplicates and $50x10^6$ and $30x10^6$ cells were stored as pellets at -80°C. Thus, screen was continued with 645X representation for H28-Cas9 cells. When the cells became confluent, cells in each flask were counted and $50x10^6$ cells were seeded again in each passage. At the end of 14 duplication times (17 days), cells were counted and $83x10^6$, $97x10^6$ and $68x10^6$ cells were obtained for Groups 1, 2 and 3, respectively. All of the collected cells were centrifuged by transferring $50x10^6$ cells for each group into another tube and stored at -80°C.

Genomic DNA was extracted by using QIAamp Blood Maxi Kit according to kit protocol. PCR was performed to amplify the gRNA region over the extracted genomic DNA as described in detail in NGS Confirmation of Amplified Library section following the protocol and conditions provided below. In total, 51.1 µg DNA template was used to achieve 100X PCR representation. Primer sequences used in the amplification of sequence library are listed in the Table 6. Mastermix was prepared as 500 µl and divided into five tubes as 100 µl. PCR amplified gRNA-targeted regions were extracted from agarose gel. Isolated libraries were sequenced on HiSeq2500 system (Illumina, San Diego, CA, USA).

NEBNext High-Fidelity 2X PCR Master Mix	250 µl

P5 primer (10 µM)	25 µl
P7 primer (10 µM)	25 µl
Template	51.1 µg
Nuclease-free H_2O	up to 250 µl

Thermocycler parameters:

Step	Temperature	Time	Number of Cycles
Initial denaturation	98°C	30 s	1
Denaturation	98°C	10 s	28
Annealing	53°C	30 s	
Extension	72°C	30 s	
Final extension	72°C	2 min	1

3.4.15. Analysis of Screen Results

The raw data from the next generation sequencing were trimmed with the Cutadapt algorithm and gRNA sequences were separated to make them ready for use in the MAGeCK algorithm. The trimmed raw data were aligned to the sequences of the Brunello library using the MAGeCK algorithm to obtain the read count for each gRNA. Then, the gRNA numbers were normalized. Robust Rank Aggregation (RRA) analysis that determines the gRNAs that were significantly selected by comparing T0 and T14 groups (for each cell line separately) was performed. Afterwards, the quality control (QC) and downstream analyses of the CRISPR screen results were performed with the MAGeCKFlute algorithm. MAGeCKFlute is a bioinformatics tool that enables comprehensive analysis of CRISPR screening data by applying MAGeCK or its extension MAGeCK-VISPR to identify target genes and then performs downstream functional analyses using FluteRRA or FluteMLE (141).

3.4.16. Competition Assay

gRNAs targeting ATG9A, BUB1, or VPS37A genes (Table 4) were cloned into pECPV backbone (135,142). MeT-5A, H2052, H2452, and H28 cells were infected and Venus positivity was measured by flow cytometry at days 0 (post-infection day 5), 4, 8, 11, and 16. Venus+ cell percentage at day 0 was normalized to 100% and following measurements were normalized accordingly.

3.4.17. Establishment of BUB1 Knockout Cells

BUB1 targeting gRNA sequences were obtained from Brunello, GeCKO and Sabatini libraries. Sequences compatible with restriction sites were added at the 5' and 3' regions of forward and reverse primer sequences and oligonucleotides were synthesized by Macrogen (Macrogen, South Korea). Renilla luciferase gene specific gRNA (g208) was used as a nontargeting control (135,143). The gRNA oligonucleotides were cloned into the lentiCRISPR v2 backbone according to a previously published protocol (144). Briefly, oligonucleotide pairs were annealed, phosphorylated, and ligated into the lentiCRISPR v2 backbone digested with the BsmBI restriction enzyme. Ligation products were transformed into Stbl3 strain. MeT-5A, H2052, H2452, and H28 cells were separately infected with vectors expressing either gRNAs and selected with puromycin for 72 h. BUB1 knock-out was validated by Western blot.

3.4.18. Western Blot

3.4.18.1. Protein Isolation

Cells were collected by trypsinization or scraping. Before scraping, cells were washed with ice-cold PBS. PBS was discarded and ice-cold RIPA buffer (Table 12) was added onto each dish. Cells were scraped and transferred into pre-cooled 1.5 ml microcentrifuge tubes. Tubes were incubated for 30 min on ice by vortexing every 10 min. Samples were centrifuged at 11000 *g*, at 4°C for 30 min. Supernatants were transferred into new 1.5 ml microcentrifuge tubes and stored at -20°C for short term storage, or at -80°C for long-term storage.

3.4.18.2. Determination of Protein Concentration

Bicinchoninic acid (BCA) assay was performed to determine protein concentration by using Pierce™ BCA Protein Assay Kit. Albumin standards were prepared as 1000, 500, 250, 125, 62.5, and 31.25 ng/ml serial dilutions. Standards and samples (2 µl of each) were added into 96-well plate as triplicate and 50 µl working reagent prepared by combining solution B and solution A by the ratio of 1:50 was added onto each sample. Sample-buffer mixture was incubated at 37°C for 30 min and absorbance was measured at 562 nm by Multiskan™ GO Microplate Spectrophotometer. The protein concentration of each sample was determined according to the standard curve which is automatically calculated by The Varioskan software. Protein concentrations of the samples to be compared were equalized in equal volumes and 5X laemmli buffer including 30% β-Mercaptoethanol was added onto each sample. Then, samples were boiled at 95°C for 5 min.

3.4.18.3. Running of Protein Samples

Each protein sample was loaded into gel as of 20 µg. Samples were run at 90V until samples leave the stacking gel and then at 120V during separation. Wet transfer was applied following the protocol provided by abcam (145). The gel and membrane are sandwiched between sponge and paper (sponge/paper/gel/membrane/paper/sponge) and all are clamped tightly together after ensuring no air bubbles have formed between the gel and membrane. Transfer was performed at 350 mA for 90 min. Then, membrane was blocked with 5% skim milk powder solved in TBS at room temperature for 1 h. After blocking, membrane was washed shortly with TBS-T and then incubated with primary antibody overnight at +4°C. Antibodies were diluted in 1% BSA in 1X TBS-T in a recommended ratio. Membranes were washed with 1X TBS-T three times for 10 min by shaking at 50 rpm. Membranes were incubated with secondary antibody at room temperature for 1 hour by shaking at 20 rpm. Then, membranes were washed with 1X TBS-T three times for 10 min by shaking at 50 rpm. Used antibody dilutions are listed in Table 18. Membranes were imaged at 700 (for anti-mouse secondary antibody) or 800 (for anti-rabbit secondary antibody) channels by Image-Studio software and Li-Cor Odyssey CLx imaging system.

3.4.19. Colony Formation Assay

Cells were seeded into 12-well plates as 600 cells per well. Medium was replaced every 3-4 days during clonal growth for ~14 days. Cells were fixed with 3.7% formaldehyde and stained with crystal violet. High-resolution images of the plates were obtained by using the Odyssey CLx Imaging System (LI-COR) and signal intensities were quantified using ImageJ 1.53e software.

To test the effect of BAY-1816032 (a BUB1 inhibitor) treatment on colony formation, 24 h after cell seeding cells were treated with three different concentrations (IC50 dose and two doses under IC50 for each cell line) of BAY816032 for 72 h. Medium was replaced with fresh medium every 3-4 days.

3.4.20. Soft Agar Assay

Agar (1 g) was dissolved in sterile 100 ml PBS and autoclaved. Agar solution (1%) was microwaved for short periods of time until it is fully dissolved and then placed into water bath at 43°C. The bottom of the 12-well plate was covered with 800 µl of equal volume of culture medium and 1% noble agar (w/v) mixture and left to solidify in hood at room temperature for 30 min. Cells were trypsinized and 8000 cells/800 µl per well were seeded by mixing equal volume of medium and 0.6% noble agar (w/v). Cell-agar mixture was left to solidify in hood at room temperature for ~15 min and 800 µl medium was added into each well. Cells were allowed to grow for 21 days. Fresh medium was added every 3-4 days. H28 cell line failed to form colonies.

To test the effect of BAY-1816032 on 3D colony formation, 24 h after cell seeding medium was discarded. Cells were treated with three different concentrations (IC50 dose and two doses under IC50 for each cell line) of BAY-1816032 for 72 h. Medium was replaced with fresh medium. After 72 h of drug holiday, cells were treated with same doses of BUB1 inhibitor for 72 h. Medium was replaced with fresh medium and fresh medium was added every 3-4 days.

3.4.21. MTT Assay

Cells were seeded into 96-well plates as 750 cells/well. After 48, 96, and 144 h, thiazolyl blue tetrazolium bromide (MTT) was added onto cells at a final concentration of 0.5 mg/ml and incubated for 4 h at 37°C. Medium was discarded and cells were incubated with 100 µl DMSO for 45 min shaking at room temperature. Absorbance signals were measured at a wavelength of 570 and 720 nm by Multiskan™ GO Microplate Spectrophotometer.

For IC50 dose calculation, cells were seeded into 96-well plates as 1500 cells/well. After 24 h, cells were incubated with different doses of BAY-1816032 for 72 h. MTT assay was performed as explained above. IC50 values were calculated using GraphPad Prism 8.0 software.

3.4.22. Bromodeoxyuridine (BrdU) Incorporation Assay

Cells were seeded on 18 mm round glass slides in 12-well plates as 20000 cells/well and allowed to grow for 48 h. Cells were labeled with 30 µM BrdU for 12 h and then rinsed with 1X PBS and fixed with ice-cold 70% ethanol for 10 min on ice. DNA was denatured with 2N HCl treatment for 30 min. Slides were washed three times with PBS-T for 5 min shaking. BrdU monoclonal antibody was added onto slides and incubated for 2 h at room temperature. Slides were washed three times with PBS-T for 5 min shaking. Cells were labeled with donkey antimouse Alexa Fluor 488 or Alexa Fluor 594 for 1 h at room temperature. Finally, slides were washed three times with PBS-T for 5 min shaking and DAPI was used to counterstain nuclei. Coverslips were mounted onto glass slides.

3.4.23. Senescence Associated Beta-Galactosidase Assay (SA-β-Gal)

Cells were seeded into 12-well plates as 20000 cells/well and allowed to grow for 48 h. Cells were fixed with 500 µl fixative solution (Table 21) for 10 minutes in room temperature. Cells were washed twice with 1X PBS and treated with staining solution (Table 21) for 12 h at 37°C. Blue staining was monitored under the phase contrast microscope.

3.4.24. Cell Cycle and Apoptosis Assay

Appropriate number of cells were seeded into 6-well plates and allowed to grow for 48 h. Cells were collected and resuspended in 300 µl PBS and 700 µl 100% ice-cold ethanol and fixed for 15 min on ice. Fixed cells were collected by centrifugation at 1200 rpm for 15 min 4°C and resuspended in 70 µl PI-solution (50 µg/ml propidium iodide, 0.1 mg/ml RNase A and 0.05% TritonX-100), and incubated for 40 min at 37°C by vortexing every 10 min. After centrifugation at 6000 rpm for 5 min at 4°C, stained cells were transferred to polystyrene tubes in 100 µl PBS and analyzed using flow cytometer. Cell cycle phases were analyzed by using FlowJo v10.8.0 software.

FITC Annexin V Apoptosis Detection Kit with PI was used for apoptosis analysis. Exponentially growing cells for 48 h were collected and washed with ice-cold PBS. After centrifugation, cells were resuspended in 30 µl Annexin V Binding Buffer. 2 µl Annexin V and 4 µl PI solution were added onto each sample and incubated for 15 min at room temperature. Cells were transferred to polystyrene tubes with additional 120 µl of Annexin V Binding Buffer and analyzed using flow cytometer. Apoptotic cells were analyzed by using FlowJo v10.8.0 software.

To test the effect of BAY-1816032 on cell cycle distribution and apoptosis, cells were treated with three different concentrations (IC50 dose and two doses under IC50 for each cell line) of BAY1816032 for 72 h prior to cell cycle and apoptosis assays.

3.4.25. Immunofluorescence

Cells were seeded on 12 mm round glass slides in 24-well plates as 12000 cells/well. After 24 h, cells were rinsed with 1X PBS and fixed with 3.7% formaldehyde for 10 min at room temperature. After permeabilization with 0.5 % Triton-X100 for 5 min, cells were washed three times with PBS for 5 min shaking and blocked with 5% BSA in PBS for 1 h in room temperature. Cells were rinsed wit PBS-T and incubated with primary antibody (diluted in 1X PBS with 1% BSA and 0.3% Triton X-100) for 1 h at room temperature. Cells were washed three times with PBS-T for 5 min shaking and incubated with donkey anti-mouse Alexa Fluor 488 for 1 h at room temperature. Finally, slides were washed three times with PBS-T for 5 min shaking and DAPI was used to counterstain nuclei. Coverslips were mounted onto glass slides.

3.4.26. Migration and Invasion Assays

Cells were loaded onto the upper well of the Transwell chamber in 24-well plate as 25000 cells/200 µl serum-free medium. The lower well was filled with 600 µl of RPMI-1640 containing 10% FBS and the cells were incubated for 48 h. Medium was removed and chambers were washed twice with 1X PBS. Cells were fixed with 3.7% formaldehyde for 2 min and washed twice with 1X PBS. After permeabilization with 100% methanol for 20 min chambers were washed twice with 1X PBS and stained with crystal violet for 15 min. Crystal violet was removed and chambers were washed twice with 1X PBS. Non-invasive cells were scraped off with cotton swabs. Migrated cells were counted under light microscope.

To test invasion rate, chambers were coated with matrigel matrix diluted 1:40 in serumfree RPMI-1640 in a final volume of 50 ul for each well and incubated for 2 h at 37°C. The remaining liquid was removed from the permeable support membrane without disturbing the layer of matrigel matrix on the membrane prior to cell seeding.

3.4.27. Wound Healing Assay

Cells were seeded into 6-well plates as 250000 cells/well. Once the cells were near confluent medium of cells was replaced with fresh medium containing %2 FBS. After 24 h, a wound area was created by using 200 µl pipette tip. Wound areas were monitored at T0 and different time points (T6 and T12 for H2052 and T24 and T48 for H2452). Scratch areas were quantified using ImageJ 1.53e software.

3.4.28. In vivo Tumor Formation Assay

To reduce the number of animals to be used, H2052 and H2452 cell lines were prioritized for *in vivo* investigation. First, $5x10^5$, $1x10^6$, or $2x10^6$ parental cells were injected subcutaneously on the right flank of NU/J mice (n=3 for each group) to assess tumor formation capacity and optimize cell number and follow-up time. However, tumor formation was only observed in four animals (all of three of H2052 $2x10^6$ group and one of H2052 $2x10^6$) and three of them were lost in time. Next, $1x10^6$, or $2x10^6$ parental cells were suspended in 100 µl 1:1 complete

medium-matrigel mixture and injected again (n=4 for each group). In addition, Huh7 cells, that we know to have high tumor formation capacity *in vivo*, were injected as well on right and left flanks as $1x10^6$ and $2x10^6$, respectively (n=1). While Huh7 cells formed tumors with a logarithmic growth, H2052 cells formed tumors but these tumors reached a limited size (at most 182 mm^3). Besides, H2452 cells failed to form tumors. Therefore, H2452 cell line was excluded from the *in vivo* experiments. Thus, *in vivo* studies were continued with the H2052 $2x10^6$ group. H2052 gRen, BUB1 g3 and BUB1 g5 cells ($2x10^6$) were suspended in 100 µl 1:1 complete medium-matrigel mixture and injected subcutaneously on the right flank of NU/J mice (n=6 for each group). Animals were examined for palpable tumors and tumor volumes were measured by using a caliper every 2-3 days for 26 days.

3.4.29. Public Data Set Analysis

To investigate the essentiality of BUB1 gene in MPM (i.e., CRISPR gene effect scores and RNA interference scores), a systematic and interactive analysis of genomic data using the CRISPR gene effect and RNA interference datasets via DepMap portal was performed.

Further, BUB1 expression levels in MPM tumors and adjacent normal tissues were accessed in the Gene Expression Omnibus (GEO) database (146). Four independent cohorts of gene expression microarray datasets of MPM and normal mesothelioma and lung tissues (GSE2549, GSE42977, GSE51024 and GSE117668) were retrieved from the GEO database. Specifically, the GSE2549 dataset consists of 42 MPM tissues and 5 adjacent non-tumoral tissues. The GSE42977 dataset consists of 39 MPM tissues and 7 adjacent non-tumoral tissues. The GSE51024 dataset consists of 55 MPM tissues and 41 adjacent non-tumoral tissues. The GSE117668 dataset consists of 36 MPM tissues and 3 adjacent non-tumoral tissues. Tissue samples in GSE2549, GSE42977, GSE51024 and GSE117668 datasets were processed on Affymetrix Human Genome U133A Array, Illumina HumanRef-6 v2.0 expression beadchip, Affymetrix Human Genome U133 Plus 2.0 Array, and Affymetrix Human Gene 2.0 ST Array platform, respectively. The datasets were analyzed and normalized using the RMA normalization algorithm. Box plots demonstrating differential expression of BUB1 were plotted using R script programming. Student's t-test was used to compare statistical differences between the two groups.

To correlate the level of BUB1 expression with epithelial-mesenchymal transition (EMT) and G2M gene sets enrichment in MPM samples, the GSE2549, GSE29211, GSE51024, GSE117668 and GSE163722 datasets were analyzed. In addition to the datasets that were explained above, the GSE29211 dataset consists of 53 MPM tissues only. All datasets were individually divided into two cohorts based on the median value of BUB1 expression. These cohorts were represented as BUB1 High and BUB1 Low groups. Differentially expressed genes (DEGs) from "High" vs. "Low" expression groups were evaluated for enriched gene sets using the GSEA tool from the Broad Institute. As for the GSEA, a list of DEGs with phenotype labels "High" vs. "Low" was uploaded to the GSEA tool, and normalized enrichment scores (NES), nominal p-values (p), and false discovery rates (FDR) were computed after 1000 random permutations of the gene set. The MSigDB gene sets database was set to hallmarks.v2022.1.Hs.symbols collection. NES> 1, $p<0.05$, and FDR<0.25 were considered to be statistically significant.

3.4.30. Study Plan and Calendar

January 2018 - December 2018	Generation and functional characterization of stable Cas9 expressing single cell clones
April 2018 - December 2018	Library amplification and NGS validation
February 2019 – May 2019	Lentiviral libray virus production and MOI calculations
May 2019 – December 2019	Screen and sequencing library preparation
January 2020 – July 2020	NGS data analysis and selection of target genes
August 2020 – April 2021	Functional validation of ATG9A, BUB1, and VPS37A genes (pECPV)
June 2021 – September 2021	Inducible system trial experiments
September 2021 – December 2021 September 2022 – January 2023	BAY-1816032 experiments
October 2021 – January 2023	Knockout studies (lentiCRISPR v2)
May 2022 – August 2022	*In vivo* studies
February 2022 – January 2023	Overexpression studies

3.4.31. Data Evaluation

All statistical analyses were performed by using GraphPad Prism 8 software. Two-tailed nonparametric Student's t-test was used to compare two independent groups and 2-way ANOVA was used to compare multiple groups. *$p<0.05$, **$p<0.01$, and ***$p<0.001$ represent the significance.

3.4.32. Limitations of the Study

At the beginning of this thesis project, since we were a newly established laboratory where the protocols used were applied for the first time and in the know-how development process, we had to carry out multiple repeats and optimization studies at many stages, especially to obtain single-cell clones and amplify gRNA library. After bioinformatical analyzes we noticed that MeT-5A cell line isn't an absolutely accurate model for segregating cancer-specific depletion genes due to being an immortalized cell line transformed with the SV40 T antigen and adapted to growth in a two-dimensional cell culture medium and carrying various karyotypic changes. For this reason, we focused on the genes in which gRNA and gene scores showed depletion in MPM cell lines but showed minimal effect in MeT-5A cell line and this limited the number of potential targets. This and the lower depletion scores of the H28 cell line than the other cell lines limited the number of candidate genes. Additionally, it was not possible to perform all experimental setups with the same infected clones, as the number of cells showing BUB1 depletion began to decrease after a while in culture. Since different polyclonal lines create variations between repeats, there is a need to use of an inducible system to avoid this.

3.4.33. Ethics Committee Approval

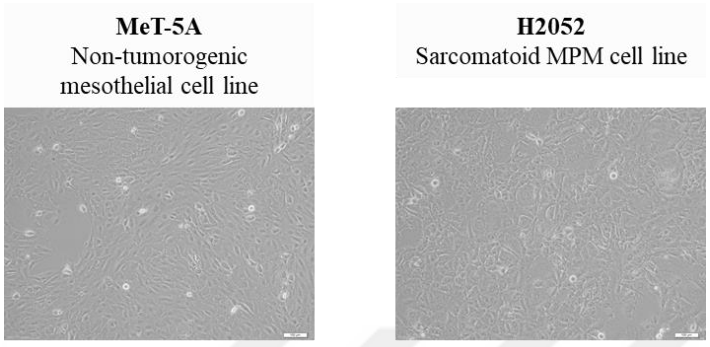
This study was approved by the IBG Local Ethics Committee with protocol number 2023-005 and the IBG Animal Experiments Local Ethics Committee with protocol number 2022015.

4. RESULTS

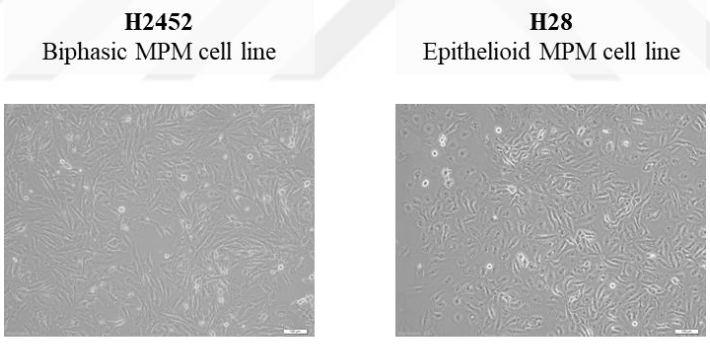
4.1. Selection of Cell Line Models

H2052 (sarcomatoid), H2452 (biphasic) and H28 (epithelioid) cell lines, which represent all three different histological subtypes and are frequently used in the literature, were selected for

genome-wide CRISPR-Cas9 screen. Of particular significance, these cell lines are wild type for the most common mutations in MPM, except for the BAP1 mutation in H28. Also, MeT5A, which is a non-tumorigenic mesothelial cell line, was used to exclude common essential genes (Figure 13).



Gene	Mutation status
BAP1	WT
NF2	Nonsense
SETD2	WT
CDKN2A	WT
CDKN2B	WT
TP53	WT
DDX3X	WT



Gene	Mutation status
BAP1	WT
NF2	WT
SETD2	WT
CDKN2A	WT
CDKN2B	WT
TP53	WT
DDX3X	WT

Gene	Mutation status
BAP1	Del
NF2	WT
SETD2	WT
CDKN2A	WT
CDKN2B	WT
TP53	WT
DDX3X	WT

Figure 13. Images of MeT-5A, H2052, H2452 and H28 cell lines under light microscope (10x magnification). Scale bar represents 100 μm.

4.2. Establishment and Characterization of Stable Cas9-Expressing Monoclonal Cells

To obtain stable Cas9 expressing clonal cells, MeT-5A, H2052, H2452, and H28 cells were infected with lentiCas9-EGFP vector. After 6 days of infection, cells expressing high GFP were enriched by FACS. Expression of GFP and Cas9 on the vector backbone occurs by the co-expression of two polypeptides on the same mRNA via the P2A self-cleaving peptide. Accordingly, GFP expression is expected to be at a similar rate as Cas9 expression. Therefore, selection of cells with high GFP expression was considered to be advantageous for Cas9 expression and hence gene editing activity. Among the GFP expressing cell populations, 6.5%, 6.3%, 6.1%, and 6.2% highest GFP expressing pools were sorted for MeT-5A, H2052, H2452, and H28 cells, respectively (Figure 14).

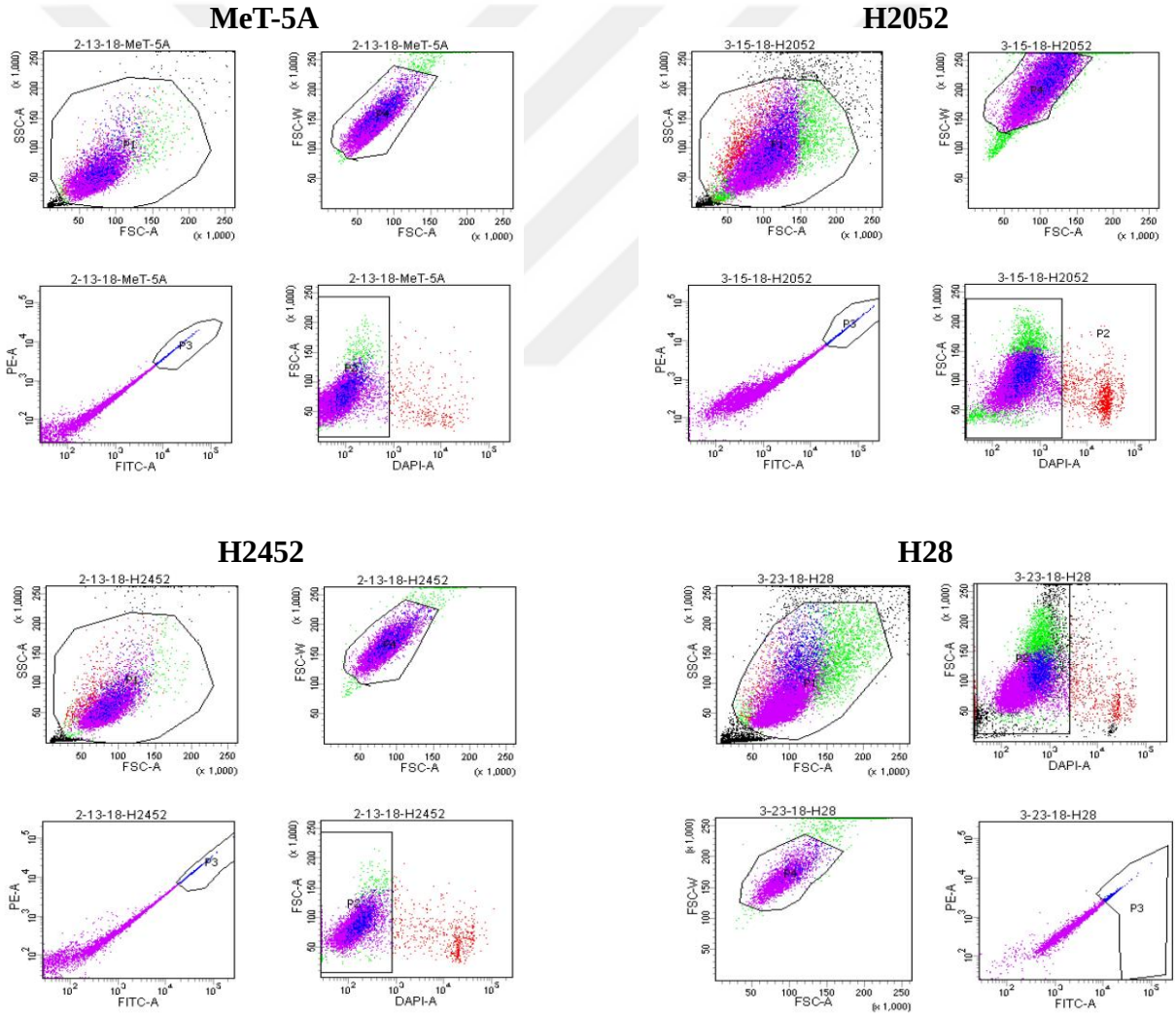


Figure 14. FACS distribution graphics of MeT-5A, H2052, H2452, and H28 cell lines infected with lentiCa9-EGFP vector. Cells with high GFP expression, indicated by P3, were selected and sorted.

After sorting, cells were grown in culture and Cas9 expression was measured at the protein level by western blot. Cas9 expression was demonstrated using the Flag antibody, because the Cas9 protein is expressed with an N-terminal Flag epitope (Figure 15).

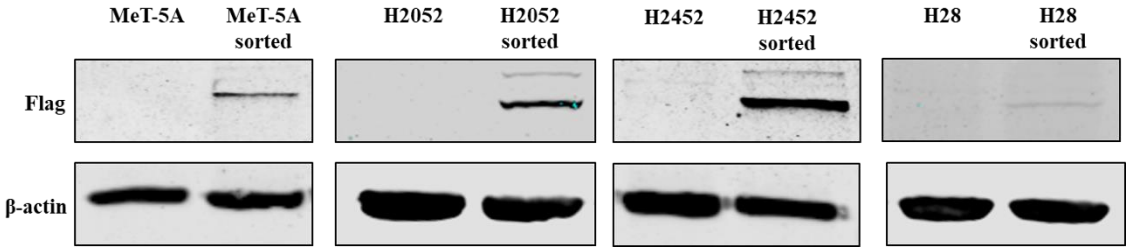


Figure 15. Western blot results of Cas9 protein levels tagged with Flag antibody in parental and sorted cells.

Cell pools enriched for GFP positivity were processed to generate single cell line clones expressing stable Cas9 at ostensibly equal or very homogenous ratio. In order to characterize single cell clones, GFP expression of obtained clones was first validated by flow cytometry (Figure 16).

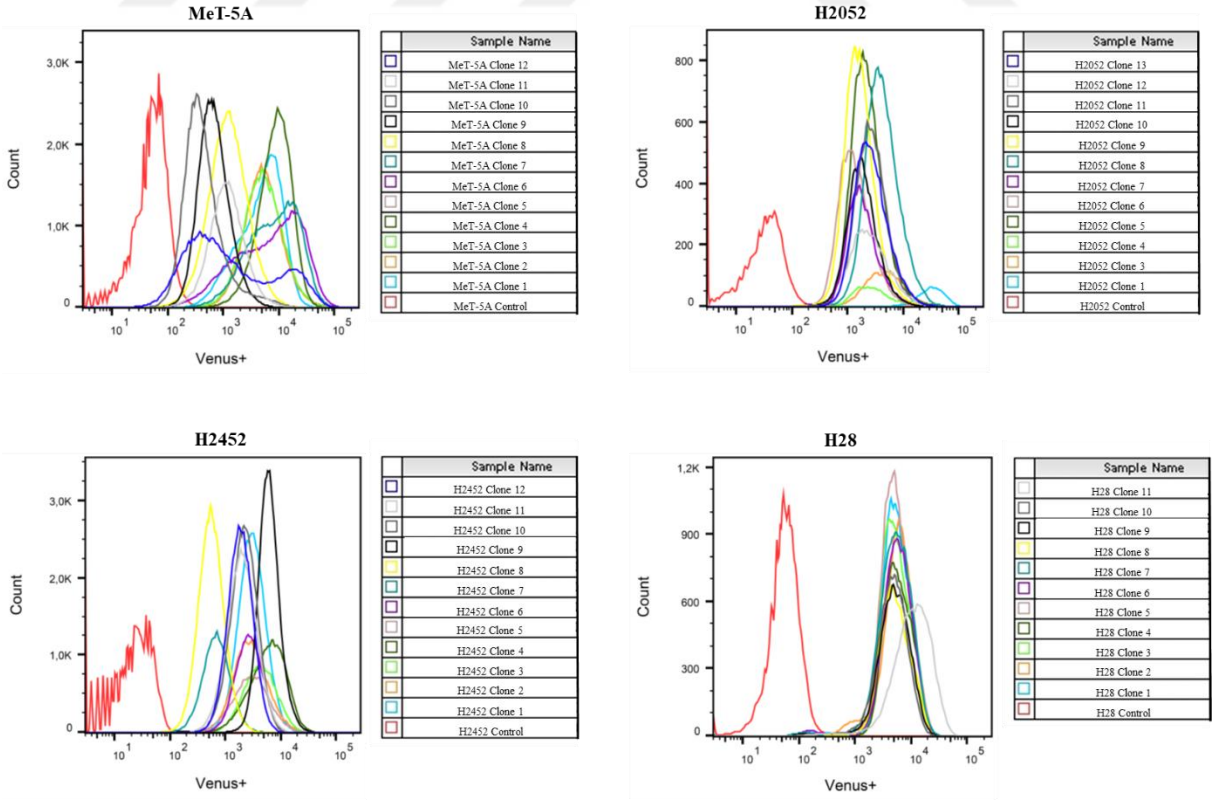


Figure 16. Flow cytometry analysis of GFP levels of Cas9 expressing MeT-5A, H2052, H2452, and H28 clones.

Based on flow cytometry analysis, five isogenic clones with the highest GFP expression in all four cell lines were selected. Protein isolation was performed, and Cas9 protein expression levels were determined by western blot (Figure 17). The clone with the highest Cas9 protein expression for each cell line (i.e., Clone 8 for H2052, Clone 4 for H2452, and Clone 4 for H28) was selected as the subline to be used in subsequent experiments. Although the highest Cas9 expression in the MeT-5A cell line was observed in Clones 2 and 3, these cells ceased to proliferate after a long period of culture. Thus, Clone 5 was chosen for this cell line. Despite our best efforts, Cas9 expression in H28 cells remained comparatively lower than other cell lines.

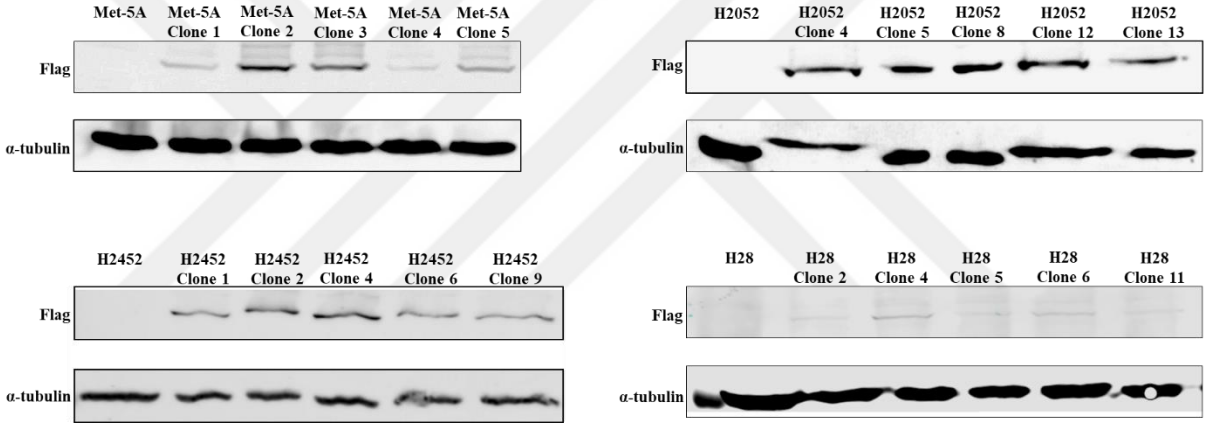


Figure 17. Western blot results of Cas9 protein levels tagged with Flag antibody in five clones with the highest GFP expression for each cell line.

Then, to functionally characterize Cas9 based genome editing performance in selected cell clones, two different strategies were followed. First, a competition assay was performed to measure the time-dependent percentage of dTomato positive cells by flow cytometry. For competition assay, cells are examined for dTomato positivity every 4 days using flow cytometry and their distribution over time is documented. Significant decrease in the percentage of dTomato positive cells infected with gRNA targeting RPA3 gene, a known essential gene whose depletion causes prominent cell death over time, shows that functional Cas9 expression is achieved in these cells. As expected, the percentage of dTomato positive cells infected with RPA3 gRNA significantly decreased over time (Figure 18).

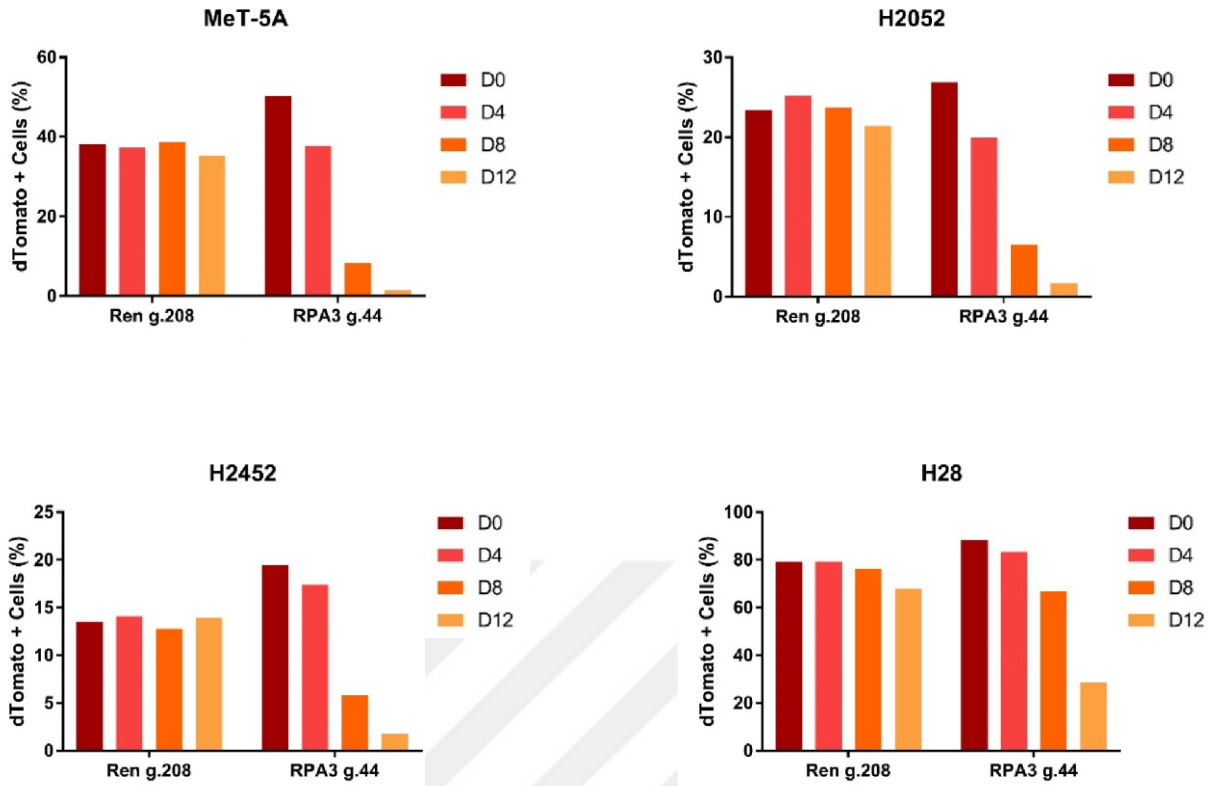


Figure 18. Competition assay results of MeT-5A-Cas9, H2052-Cas9, H2452-Cas9, and H28Cas9 cells. While percentage of dTomato positive cells infected with gRen showed slight changes, this value decreased significantly over time in cells infected with RPA3 gRNA.

Secondly, T7 Endonuclease I (T7EI) assay was performed by targeting the EGFR gene (Exon 1). Genomic DNA (gDNA) was isolated from cells infected with gRen and EGFR specific gRNA and the EGFR gene region was amplified by PCR. PCR products were confirmed by agarose gel electrophoresis and extracted from the gel. Extracted amplicons were digested with T7EI. In this protocol, after nucleic acid insertion and/or deletion (indel) induced by functional Cas9 in the target gene has taken place, the targeted region is amplified from genomic DNA by PCR. Then, following multiple repeats of denaturation and reannealing, heteroduplexes with mismatches are formed and these mismatches are digested with T7EI and run on an agarose gel. According to our results, a ~950 bp band of EGFR amplicon should be observed in control cells (gRen). As expected, a ~950 bp intact band, as well as ~300 bp and ~600 bp bands resulting from digested mismatches were observed in cells expressing EGFR targeting gRNA (g60) (Figure 19).

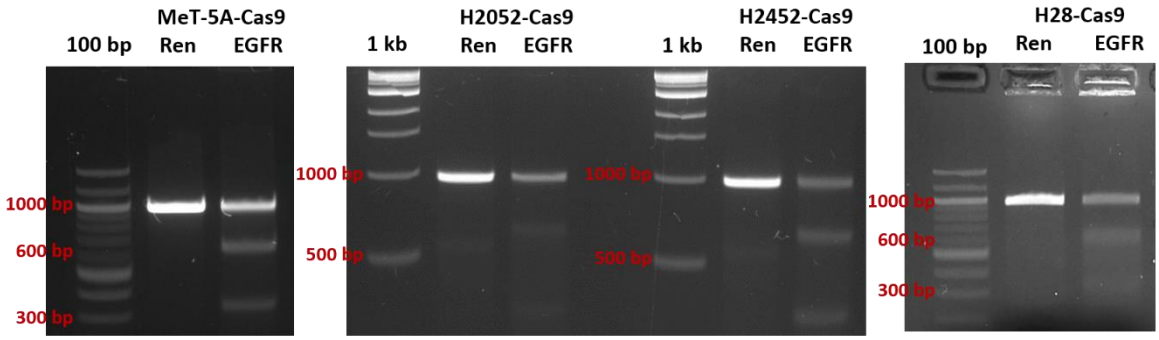


Figure 19. Agarose gel images of EGRF amplicons digested with T7E1 enzyme. While a ~950 bp intact band was detected in gRen cells, a ~950 bp intact band, as well as ~300 bp and ~600 bp bands were detected in cells targeted with EGFR gRNA consistent with mismatches resulted from indels.

4.3. Library Amplification and NGS Confirmation

The Brunello library used in our project is a second generation whole-genome gRNA library with reduced off-target effects developed by David Root and colleagues (137) at the Broad Institute for CRISPR-Cas9 screenings in human cell lines. This library contains 76441 unique gRNAs (3-4 gRNAs for each gene) that target 19114 genes in the human genome as well as 1000 negative control gRNAs. Brunello gRNA library was amplified according to the recommended protocol using Endura™ ElectroCompetent Cells and grown by plating on bioassay dishes. Meanwhile, bacteria culture was spread onto 100 mm agar plates as 1/500, 1/10000, and 1/40000 dilutions to calculate colony formation unit (CFU). Colonies obtained from 1/40000 dilution were counted and CFU value and coverage were calculated according to the formula given below. This calculated value is above 1000X coverage, which is considered a good library amplification indicator by many sources (Figure 20).

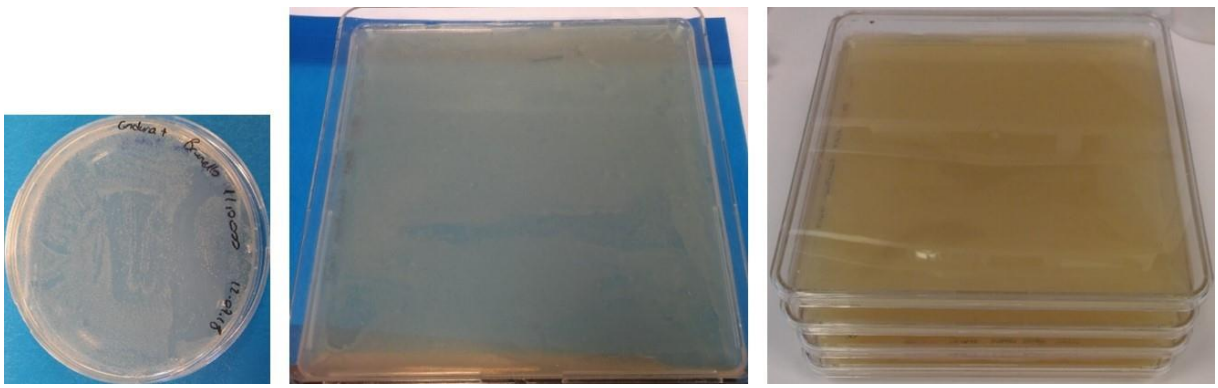


Figure 20. Colonies obtained as a result of transformation of library plasmid DNA with Endura bacterial cells.

$$\frac{Number\ of\ transformants}{DNA\ concentration} x \frac{colonies}{\mu g\ volume} x \frac{1x10^{6}\ volume\ of\ plated}{dilution\ factor}$$

$$\frac{2375}{400\ ng} x \frac{1x10^{6}}{\mu g} x \frac{5}{10\ \mu l} x 80 = 2.3x10^{9}\ CFU\ -\ ml$$

$$\frac{2375x40000}{77441} = 1226X\ coverage$$

Next, the amplified library (in house) and the original library (obtained from Addgene) were deep sequenced on HiSeq2500 system. The representation of the amplified library was determined and compared to the original library. The NGS results were analyzed using the count_spacer.py script in accordance with the library content (list of gRNA sequences). According to the findings of this analysis, the sequencing data of the original Brunello library, which was amplified by Addgene and which we accept as a reference, showed 93.5% similarity to the gRNA content of the library provided by David Root et al, while the amplified library (in house) showed 93.6% similarity. The percentage of mismatched gRNA was 0.2% for the original library and 0.3% for the amplified library. In addition, the skew ratio was calculated as 4.50% for the original library and 4.46% for the amplified library. Notably, libraries with a matched gRNA percentage above 70%, an undetectable gRNA percentage below 0.5%, and a skew ratio lower than 10% are considered ideal (138). Accordingly, the library amplified in our laboratory has achieved results that are above the ideal values, and even completely overlapping with the original library.

In addition, a Lorenz curve was drawn to compare the gRNA representation of amplified library and the original library. The gRNA representation of any established library can be visually depictured and more easily understood with the Lorenz curve. Therefore, the number of gRNA reads in the file is ranked first by most frequent, followed by how much of the gRNAs are represented. In an ideal library, each gRNA should in principle be represented with exactly the same frequency. Hence, the "read count" on the Lorenz curve increases steadily, forming a diagonal line. In this case, the "area under the curve (AUC)" value would be 0.5. Deviation from

this ideal condition causes an upward swell in the cumulatively plotted Lorenz curve and the AUC value increases, but the closer this AUC value is to 0.5, the better the representative quality of the library. In this case, the Lorenz curve of the library amplified in our laboratory was as shown in Figure 21A and its AUC value was 0.66. With this result, one can deduce that there is no major deviation in the representation of the Brunello library. To compare the representation of the amplified library, the Lorenz curve was also drawn for the original library and the AUC value was calculated as 0.66 (Figure 21B). These data suggest that the library which was amplified in our laboratory had completely overlapping results with the original library obtained from Addgene.

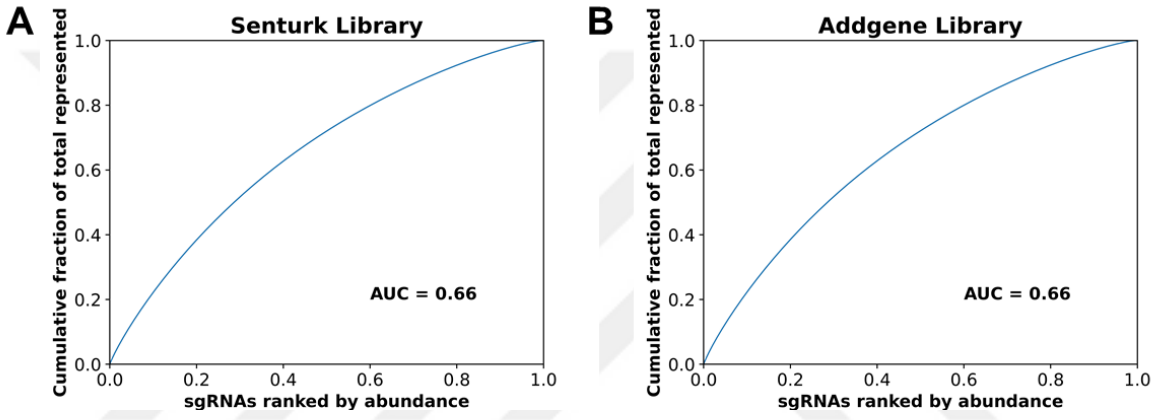


Figure 21. Lorenz curve of amplified (A) and original (B) Brunello libraries.

4.4. Puromycin Kill Curve and Selection Dose Calculation

The Brunello library used in this project was designed on the lentiGuide-puro backbone. Since the backbone contains the puromycin resistance gene as the mammalian selection marker, a puromycin kill curve was performed in the studied cell lines. To this end, cells were treated with puromycin in the range of 0.5-10 µg/ml as 1:2 serial dilutions for 72 h and the results were visualized by crystal violet staining. As a result, the puromycin selection doses were determined as 2 µg/ml for MeT-5A and H28 cell lines, and 3 µg/ml for H2052 and H2452 cell lines (Figure 22).

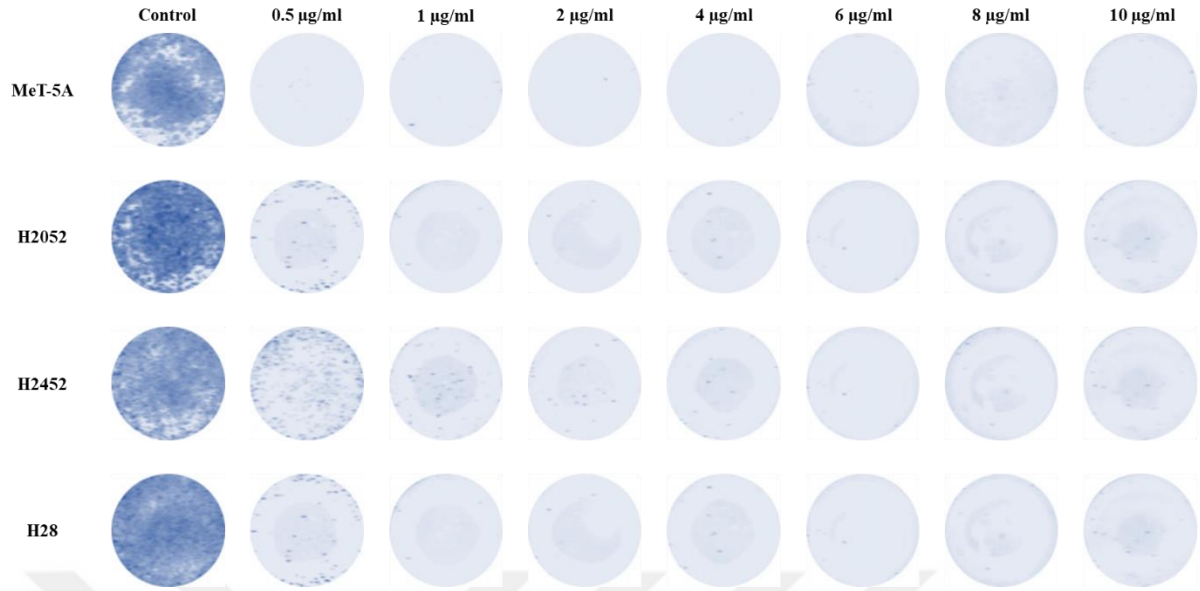


Figure 22. Images of MeT-5A, H2052, H2452, and H28 cell lines stained with crystal violet after different doses of puromycin treatment for 72 h.

4.5. Large Scale Virus Production

After library amplification and validation, small-scale (100 mm dish) virus production was performed as a preliminary trial. Despite a successful packaging of the gRNA plasmid library, repeat experiments showed that small-scale titration calculations did not contribute enough to the data evaluations. Then, large-scale virus production (120 ml) was performed and the titration - in terms of representation - was calculated at this scale (Figure 23).

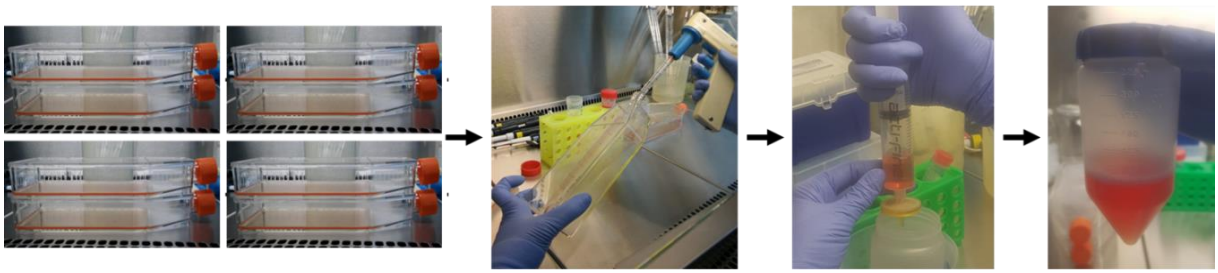


Figure 23. Photographed flow of large-scale virus production and collection.

4.6. MOI Calculation

Multiplicity of infection (MOI) is a term that is frequently used in virology and expresses the number of virus particles per cell during infection. The number of virus particles that each cell receives at different MOIs is formulated with the Poisson Distribution ($P(n) = e^{-m}m^n/n!$). In this

formula, e represents the base of the natural logarithm, m represents the transduction coefficient, and n represents the virus particles. P(n) is the probability of a cell being infected with n particles (147,148). MOI < 1 is generally preferred for whole-genome functional CRISPR-Cas9 screens. The aim here is to keep the number of cells infected with more than 1 virus to a minimum, that is, to ensure the genome integration of a single gRNA into the infected cells after viral transduction. Thus, gRNA expression is aimed to target a single gene in each cell. Accordingly, taking the MOI = 0.3 (i.e., 20-30% total transduction rate) in the above formula, the number of cells infected with more than one virus and thus the possibility of multigenome integration is minimized. To determine the virus dilution that provides MOI ~0.3, MeT5A-Cas9, H2052-Cas9, H2452-Cas9, and H28-Cas9 cells were infected in the range of 1/16 to 1/128 as 1:2 serial dilutions with the gRNA lentivirus library on a mini scale (6-well plate). Cells were selected for 72 h with the determined doses of puromycin starting at 48 h post infection. After selection, cells were trypsinized and counted, and the dilutions providing MOI of ~0.3 were determined (Table 25). These dilutions were also confirmed on midi scale (100 mm culture dish) (Table 26). In summary, virus dilutions of 1/128, 1/48, 1/24 and 1/128 were selected for MeT-5A-Cas9, H2052-Cas9, H2452-Cas9, and H28-Cas9 cells, respectively.

Table 25. Obtained infection rates calculated by proportioning number of infected and puromycin selected cells to uninfected control group in mini scale (6 well plate).

	Infection rate (%)			
Cell line	**1/16**	**1/32**	**1/64**	**1/128**
MeT-5A-Cas9	91.2	70.6	43.9	39.2
H2052-Cas9	-	54.8	20	9.7
H2452-Cas9	57.37	29	11.75	3.1
H28-Cas9	88.4	60.9	57.8	39.4

Table 26. Obtained infection rates calculated by proportioning number of infected and puromycin selected cells to uninfected control group in midi scale (100 mm dish).

	Infection rate (%)				
Cell line	**1/24**	**1/32**	**1/48**	**1/64**	**1/128**
MeT-5A-Cas9	-	-	-		31.4
H2052-Cas9	-	-	34.9	28.7	-
H2452-Cas9	33.5	19.5	-	-	-
H28-Cas9	-	-	-	-	35.8

4.7. Whole Genome CRISPR-Cas9 Screen

MeT-5A-Cas9, H2052-Cas9, H2452-Cas9, and H28-Cas9 cells seeded into 5-layer flasks were infected with Brunello lentivirus library at MOI ~0.3 (1/128, 1/48, 1/24, and 1/128 dilutions, respectively). After 48 h of infection, cells were selected with puromycin (2-3 µg/ml) for 72 h. Cells were trypsinized and counted. Total number of cells were divided into 4 groups. Three groups were seeded as triplicates and one group of each cell line was stored as cell pellet. At least $20x10^6$ cells ($32x10^6$, $36x10^6$, $80x10^6$, and $80x10^6$ cells, respectively) were collected as T0 samples. After 14 doubling times, all cells were collected and stored as T14 samples (Figure 24).

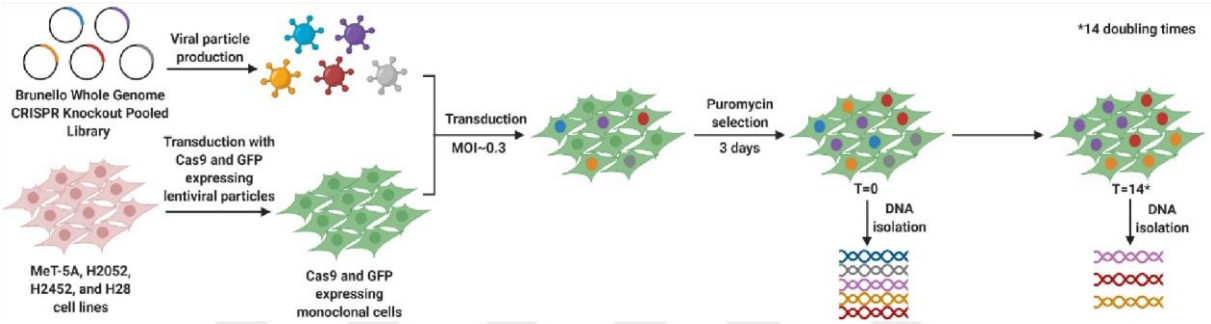


Figure 24. Depictured flow of the screen process.

4.8. Illumina Platform Compatible gRNA PCR Library Preparation and Next Generation Deep Sequencing

After the screen was completed for all cell lines, total genomic DNA was isolated from T0 and T14 pellets and DNA concentrations were measured (Table 27).

Table 27. DNA concentrations of each time point/group of screen samples.

Cell Line	Concentration (ng/µl)	A260/280	A260/230
MeT-5A-Cas9 T0	1033.1	1.92	2.32
MeT-5A-Cas9 Group 1	970.2	1.93	2.33
MeT-5A-Cas9 Group 2	1070.5	1.92	2.35
MeT-5A-Cas9 Group 3	942.9	1.93	2.35
H2052-Cas9 T0	1350.3	1.92	2.34

H2052-Cas9 Group 1	1163.3	1.94	2.34
H2052-Cas9 Group 2	1174.7	1.93	2.36
H2052-Cas9 Group 3	1078.9	1.93	2.34
H2452-Cas9 T0	720.2	1.91	2.25
H2452-Cas9 Group 1	720.4	1.88	2.21
H2452-Cas9 Group 2	696.0	1.90	2.28
H2452-Cas9 Group 3	768.9	1.92	2.27
H28-Cas9 T0	1190.8	1.89	2.31
H28-Cas9 Group 1	1646.8	1.92	2.33
H28-Cas9 Group 2	1490.7	1.91	2.35
H28-Cas9 Group 3	1627.4	1.91	2.33

Following the PCR reaction required for the preparation of the sequence library as described in the method section, the bands of expected amplicon length were excised from the gel (Figure 25) and purified (Table 28).

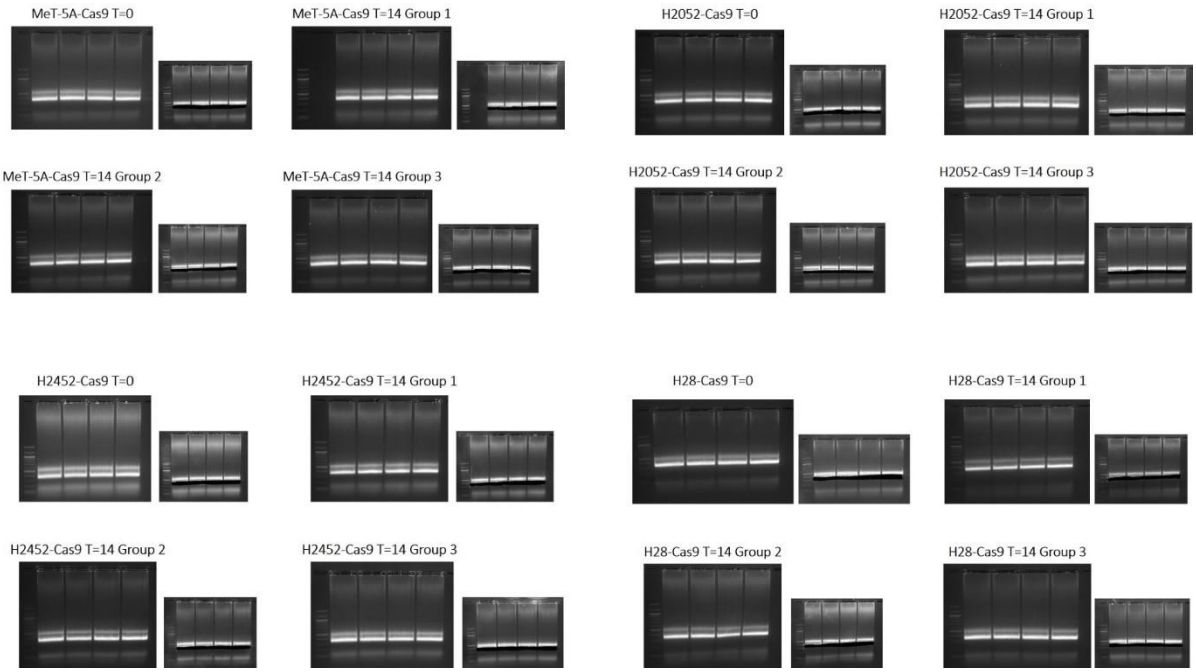


Figure 25. Agarose gel image of sequence library samples. After PCR reaction conducted with P5 and P7 primers an amplicon of ~354 bp is expected. In our images, in addition to the expected band size, a higher length and fainter band is visible. Considering the agarose gel images in various studies of the Feng Zhang laboratory at MIT, which is accepted as the pioneering reference in this field, ready-to-run PCRs can contain diffuse contamination above the relevant band length. These bands mostly disappear by gel extraction, yet do not interfere with NGS.

Table 28. Concentration of the sequence libraries extracted from agarose gels

Cell Line	**Concentration (ng/µl)**	**A260/280**	**A260/230**
MeT-5A-Cas9 T0	137.3	1.86	1.89
MeT-5A-Cas9 Group 1	124.8	1.84	1.73
MeT-5A-Cas9 Group 2	145.0	1.86	1.93
MeT-5A-Cas9 Group 3	157.6	1.86	1.94
H2052-Cas9 T0	140.2	1.88	1.87
H2052-Cas9 Group 1	150.5	1.88	1.67
H2052-Cas9 Group 2	120.9	1.85	1.80
H2052-Cas9 Group 3	164.9	1.88	1.61
H2452-Cas9 T0	137.1	1.86	1.73
H2452-Cas9 Group 1	145.1	1.87	1.98
H2452-Cas9 Group 2	159.3	1.88	1.85
H2452-Cas9 Group 3	134.7	1.87	1.72
H28-Cas9 T0	146.8	1.9	2.20
H28-Cas9 Group 1	111.3	1.87	2.13
H28-Cas9 Group 2	141.3	1.89	2.12
H28-Cas9 Group 3	168.8	1.90	1.9

4.9. The Analysis of Whole Genome CRISPR-Cas9 Screen

The reads obtained after deep sequencing were first analyzed with the count_spacers.py program and the read distributions of the gRNAs were plotted (Figure 26). In the chart, the reads shifting towards the Y-axis (i.e., 0 value on the X-axis) indicate decreased representation for those gRNAs, while the reads for gRNAs shifting in the opposite direction have an increased representation in the pool. Immediately, a decent number of gRNAs demonstrated depletion and/or enrichment in all cell lines. As expected, however, most of the gRNAs remained unchanged after the screen. According to this data, it was possible to conclude that CRISPRCas9 screen was successful in all cell lines. Notably, though, the number of gRNAs with a shift (negative or positive) in the number of reads in H28 cell line was less prominent than that of other cell lines, suggesting that the screen performance in this cell line was considerably lower.

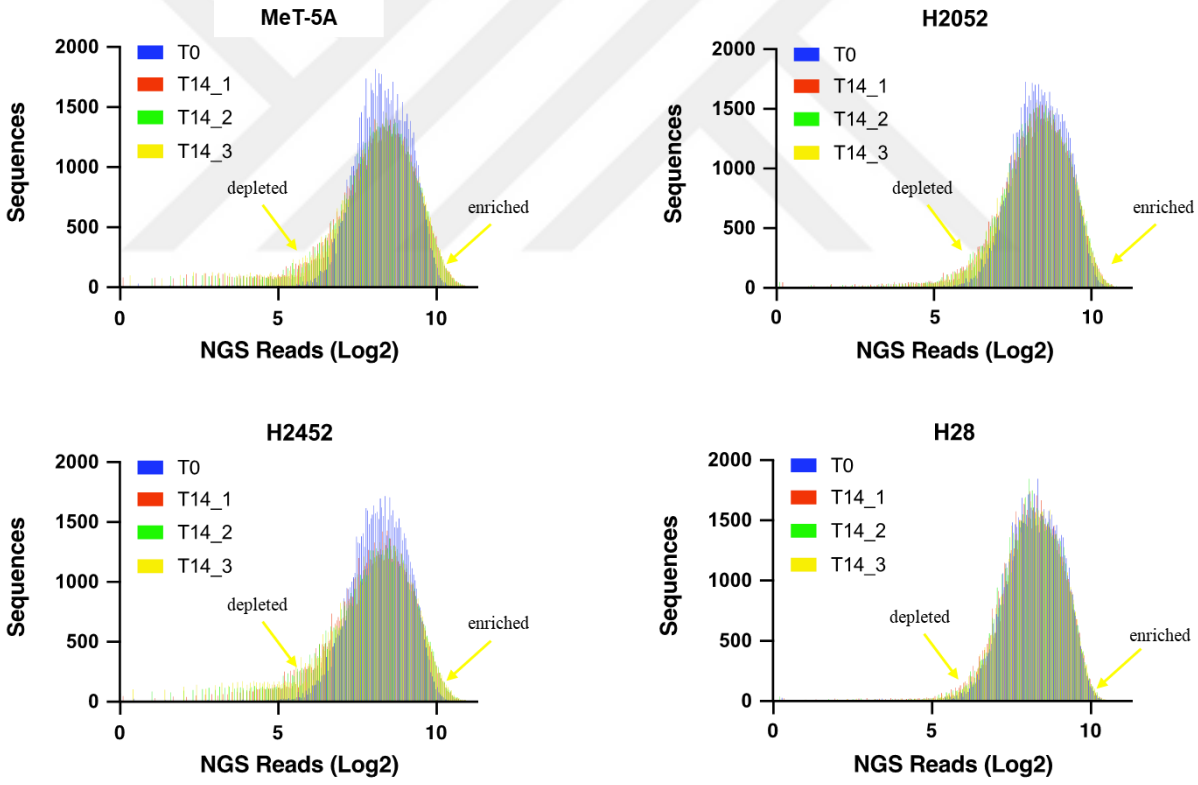
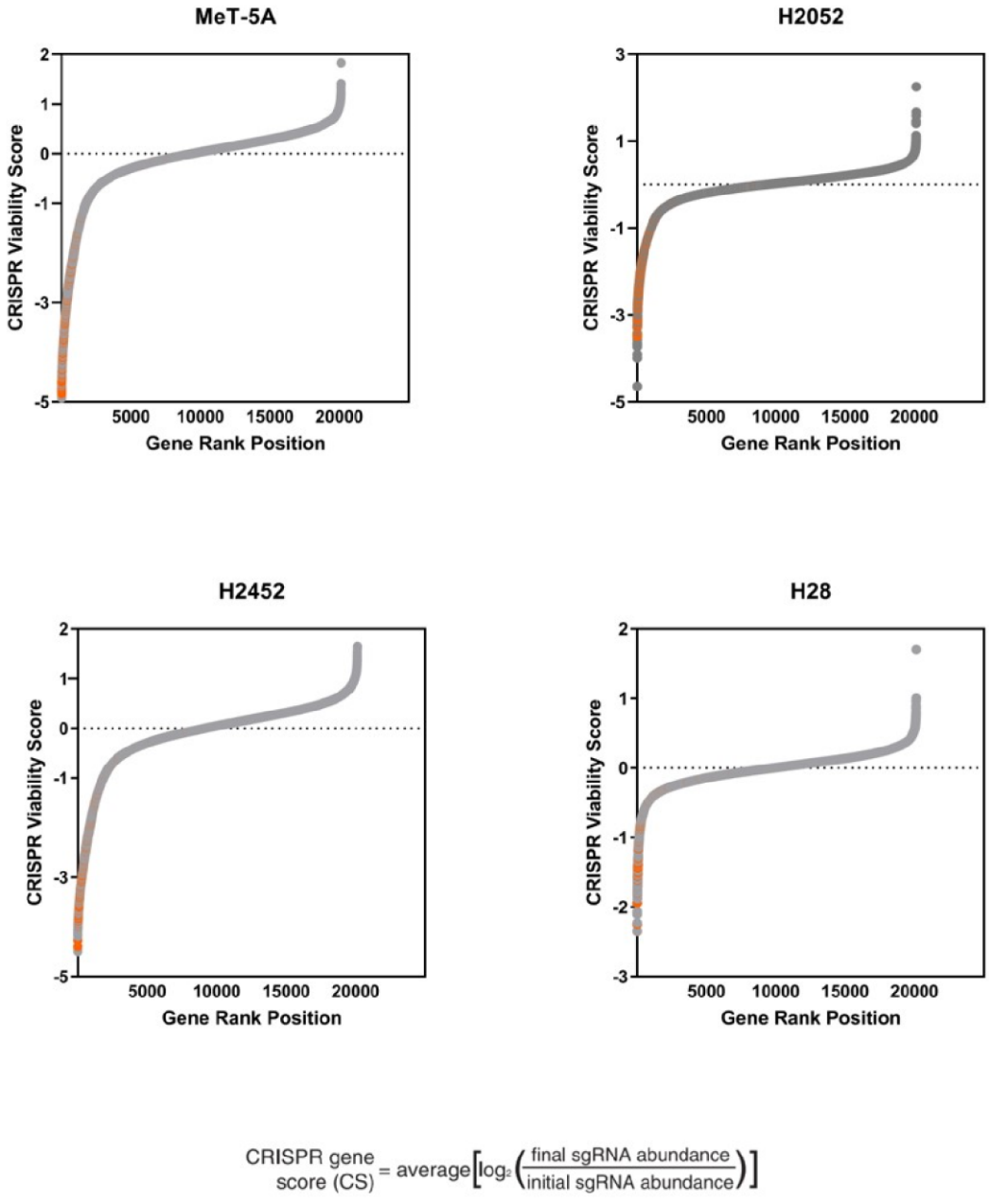


Figure 26. Image of gRNA read distributions obtained by count_spacers.py analysis after deep sequencing. Genes whose distributions shift to the left side of the figure represent depleted genes, and genes that shift to the right side of the figure represent enriched genes. NGS Reads (Log2) indicates the representation of each gRNA.

Following this primary analysis, the gRNA scores were obtained with the MaGecKFlute pipeline (141), and the log2 fold changes of these gRNAs were depicted with GraphPad Prism

8. In the waterfall chart showing the gRNA distributions (Figure 27), the positions of each gRNA targeting well-defined common essential genes (149) are highlighted by orange dots. As expected, the gRNAs targeting the common essential genes displayed negative depletion on the Y-axis (Figure 27).



$$\text{CRISPR gene score (CS)} = \text{average}\left[\log_2\left(\frac{\text{final sgRNA abundance}}{\text{initial sgRNA abundance}}\right)\right]$$

Figure 27. Graph showing the distributions of gRNAs and the positions of gRNAs targeting common essential genes (orange dots) in this distribution.

Similarly, the dot plot chart comparing the distribution of T14 samples to T0 samples, confirmed that the gRNAs targeting common essential genes (orange dots) had produced significant depletion scores. On the other hand, the distribution of non-targeting gRNAs (blue dots), negative controls in the Brunello library, remained largely unchanged (Figure 28). These findings point out that the CRISPR screen enabled the identification of common essential genes in MeT-5A as well as the MPM cell lines.

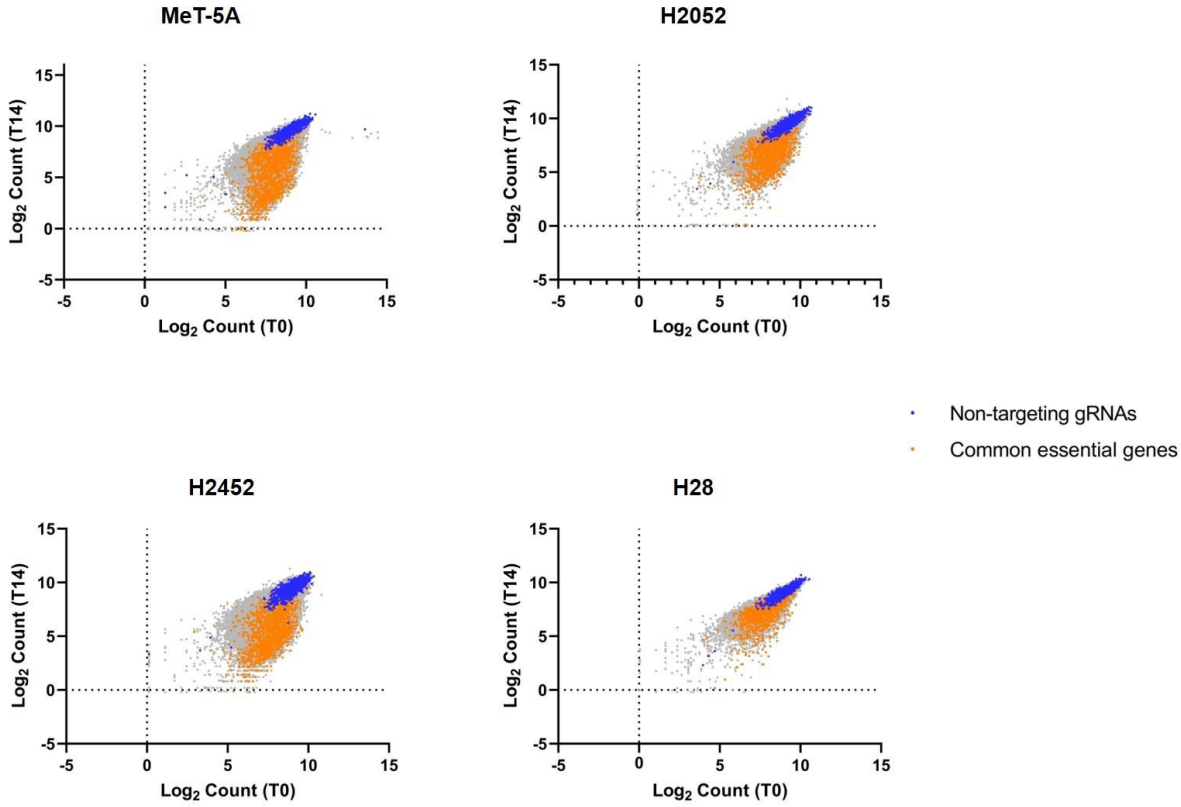


Figure 28. Graph showing the distributions of T14 gRNA scores relative to T0 gRNA scores, and the locations of gRNAs targeting common essential genes (orange dots) and non-targeting gRNAs in this distribution.

Next, deep sequencing data were further analyzed using the MaGeCKFlute pipeline. That is, the gRNAs that were significantly depleted or enriched by negative or positive selection, respectively, and their distribution patterns were depictured by RRA (Robust Rank Aggregation) analysis (Figure 29). As expected, the gRNAs which target the genes with known oncogenic functions such as *CCT6A*, *KPNB1*, *HSPA5*, and *CCNA2* (150–153). In contrast,

enriched gRNAs included those that target tumor suppressor genes such as *PTEN*, *TP53*, *CDKN1A*, and *CPEB2* (154,155).

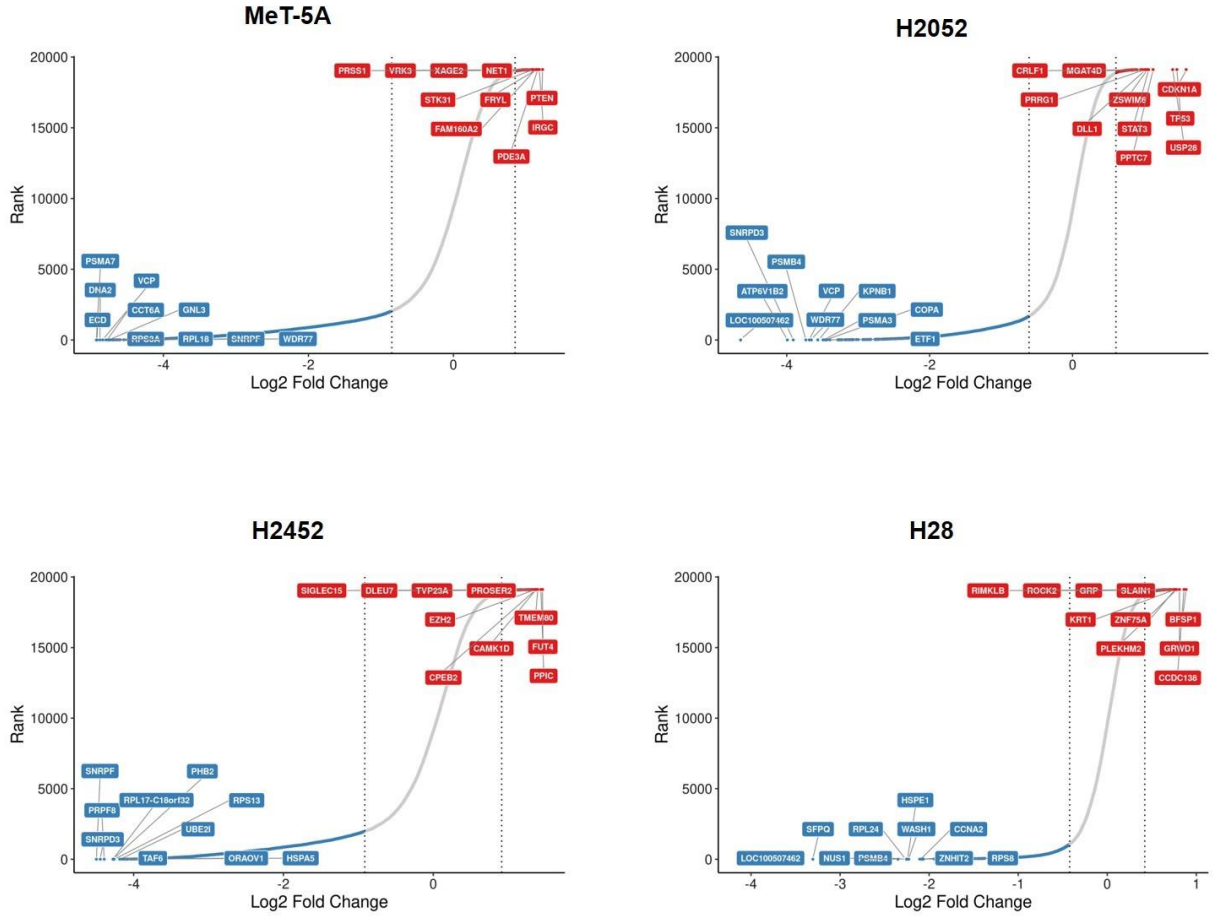


Figure 29. Significantly depleted and enriched gRNA distributions obtained by RRA analysis. Log2 fold changes negative values indicate depleted genes, and positive values indicate enriched genes.

To investigate how the most significantly depleted genes were classified/grouped based on their molecular function and/or pathway, KEGG analysis, a key component of the MaGeCKFlute algorithm, was initially performed. Accordingly, the pathways enriched for the genes with the highest depletion scores were investigated. As shown in Figure 30, the molecular functions critical for cell survival, DNA replication, RNA polymerases and ribosomes were enriched. Next, the top 200 genes with the highest depletion score in each cell line were annotated by the DAVID functional annotation database (Figure 31). In line with the previous observations, this analysis also identified several genes that were involved in key molecular functions associated

with cell survival including cell cycle, ribosomal function, RNA transport, and pyrimidine metabolism.

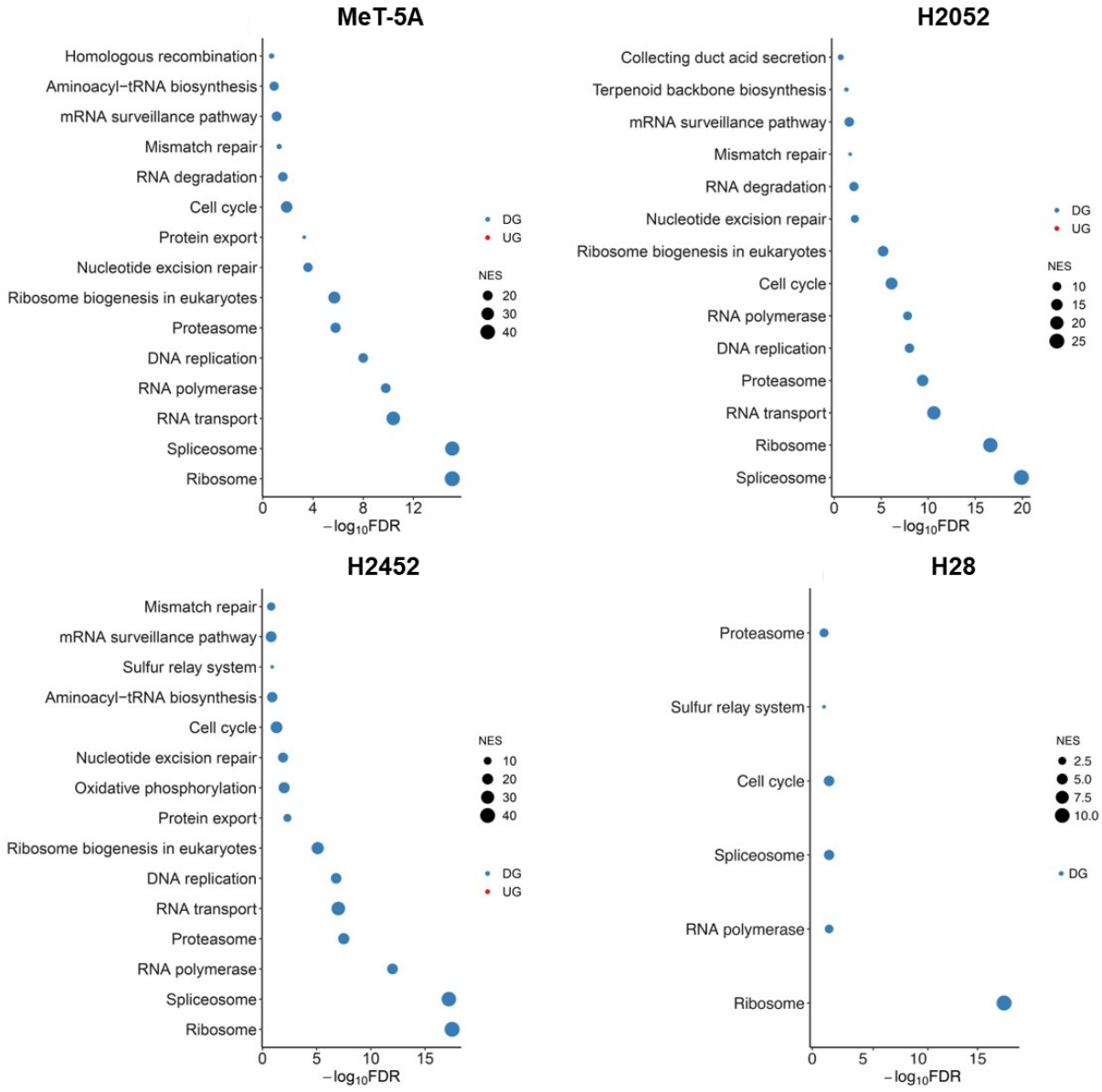


Figure 30. Biological processes and molecular functions involving the genes with the highest depletion score after CRISPR screen obtained by KEGG analysis.

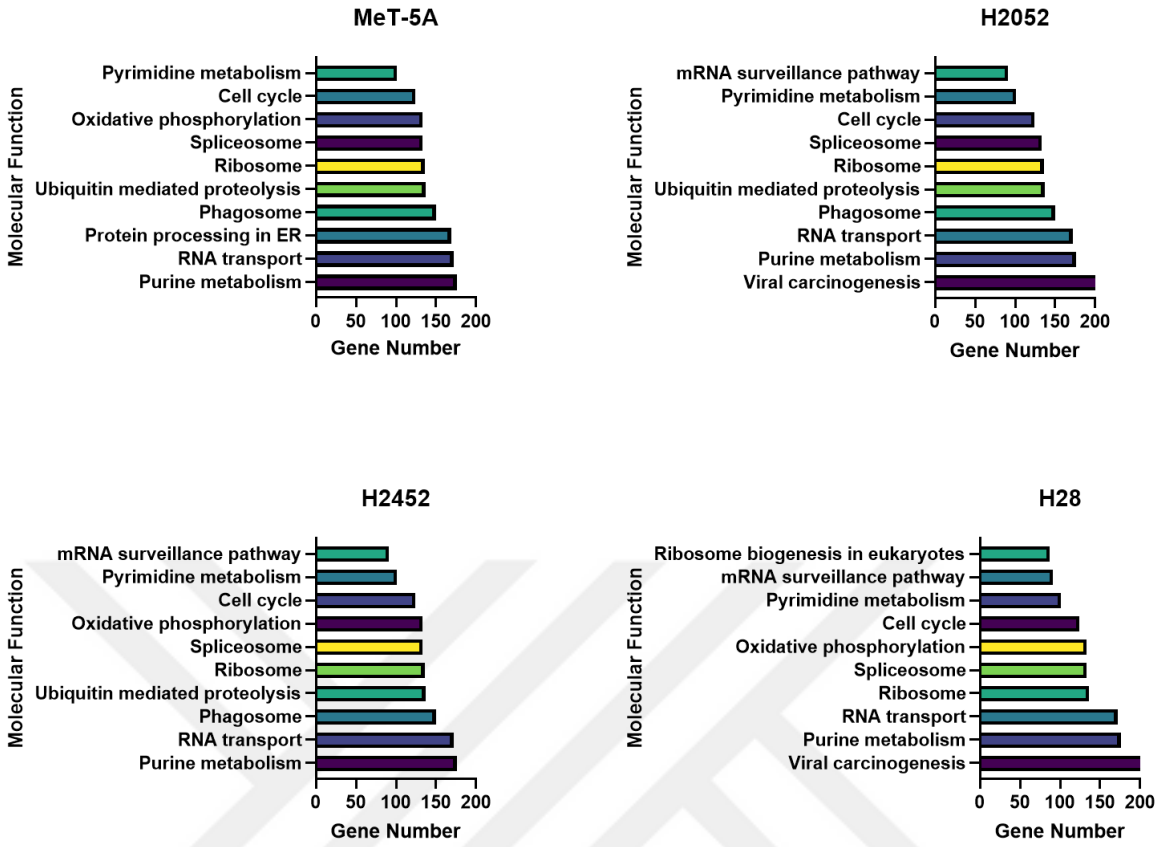


Figure 31. DAVID annotations showing the molecular functions in which the top 200 genes with the highest depletion score clustered.

4.10. Selection of Candidate Genes

The findings presented so far strongly suggest that the technical and biological nature of the CRISPR-Cas9 screens can enable the identification of MPM cell line specific cancer essential genes, in other words, the genes with significant depletion in MPM cell lines but not in the MeT-5A cell line, hence the aim of this thesis. To pursue this goal, first, genes with negative p-value ≤0.05 were sorted. Then, genes that scored in common for all three of the H2052, H2452, and H28 cell lines were listed. From this gene list, those that co-scored with the MeT-5A cell line were excluded. However, since MeT-5A is not the absolutely accurate model for segregating cancer-specific depletion genes due to karyotipic changes it gained upon immortalization and the screening efficiency of the H28 cell line and thus the depletion scores was lower than other cell lines, a few genes were listed. Then, two different strategies were followed based on depletion scores.

First, gRNAs with a **gRNA score** of more than 50% depletion (log2 ≤ -1) were listed. Because the number of gRNAs with log2 ≤ -1 were limited in the H28 cell line, this depletion value was adjusted to the mean value (-0.36) of the negative fold changes for this cell line. More importantly, the genes represented by less than 2 gRNAs (the library has an average of 4 gRNAs per gene) were excluded from the resulting list. Of the remaining genes, those that scored in common for all three of the H2052, H2452, and H28 cell lines were listed. From this gene list, those that co-scored with the MeT-5A cell line were excluded (Table 29).

Table 29. List of genes that scored in common in three MPM cell lines but co-scoring with MeT-5A cell line based on gRNA score.

Gene	MeT-5A LFC				H2052 LFC			
	gRNA1	gRNA2	gRNA3	gRNA4	gRNA1	gRNA2	gRNA3	gRNA4
ALG5	-0.56	-1.00	-0.93	-1.23	-0.12	-1.65	-0.84	-1.29
ATG9A	-0.36	-0.52	-1.26	0.40	-1.43	-2.39	-1.47	0.35
BUB1	-3.20	0.69	0.81	0.22	-2.36	-1.51	-4.35	0.48
CCND1	-0.72	-0.31	0.06	0.27	-1.88	-2.20	-2.37	-2.07
CCNK	0.16	-0.93	-0.80	-5.53	0.05	-0.11	-1.26	-2.70
CDK2	-0.80	-0.01	0.57	-0.56	-2.40	-1.55	0.15	-1.51
DCLRE1B	-0.31	-1.09	0.09	-0.97	-1.10	-0.99	-1.08	-0.67
DPM3	-1.00	-1.12	0.55	0.00	-1.06	0.26	0.22	-1.32
EIF1	-0.64	-0.44	-2.39	0.47	-1.51	-0.05	-1.64	0.15
GOLGA8N	-0.85	-0.70	-3.97	-0.11	-1.20	-1.21	-1.39	1.28
HIST1H2BL	-0.95	0.56	-1.30	-0.61	-0.74	-0.54	-1.40	-1.65
HIST1H2BN	-0.24	-4.79	-0.62	1.03	-0.19	-1.88	-0.18	-1.08
HIST2H2AC	-0.55	-0.36	-1.78	-0.56	-0.53	-1.43	-1.54	-0.18
ILK	-0.52	-2.22	-0.93	0.10	-0.59	-1.45	-0.91	-1.01
NAA30	-1.22	-0.98	-0.07	-0.45	-0.43	-1.77	-1.34	-0.80
NPIPA5	-0.19	0.18	-1.55	-0.05	-0.05	-1.18	-0.97	-1.15
PAXBP1	-0.07	-0.34	-0.09	-3.90	-0.33	-0.70	-2.08	-1.91
PIKFYVE	-0.71	-1.65	0.87	0.37	-1.18	-1.37	0.32	-0.61
RNF8	-0.73	-0.49	-2.72	0.42	-1.01	-0.09	-2.33	-0.54
RPN2	-2.14	-0.76	-0.74	-0.91	-1.13	-0.52	-1.42	-1.78
TMEM41B	-0.06	-1.03	0.08	-0.72	0.47	-1.99	-0.60	-1.64
TOP1	1.25	-0.44	-0.31	-1.08	-0.64	0.25	-2.19	-2.66
USP17L25	-0.85	0.03	-0.63	-0.01	-1.36	-0.42	-1.83	-1.13

VPS37A	-0.16	0.06	-0.16	-0.57	-1.65	0.17	-1.54	-1.46
ZNRD1	-3.49	-0.84	-0.83	-0.70	-2.12	-1.40	-0.41	-0.11
Gene	H2452 LFC				H28 LFC			
	gRNA1	gRNA2	gRNA3	gRNA4	gRNA1	gRNA2	gRNA3	gRNA4
ALG5	-0.23	-2.92	-1.57	-1.24	-0.13	-0.30	-0.65	-0.40
ATG9A	-2.30	-2.04	-0.82	-0.12	-1.29	-0.31	-1.00	0.15
BUB1	-2.62	-1.18	-2.75	0.26	-0.68	0.21	-0.57	0.35
CCND1	-1.59	-1.18	-1.38	-1.26	-0.32	-2.21	-0.70	-0.88
CCNK	0.63	-1.29	-1.72	-4.25	0.39	0.21	-1.23	-1.28
CDK2	-1.10	-2.01	-2.05	0.09	-0.49	-0.22	-0.26	-0.57
DCLRE1B	-1.29	-1.66	-1.12	-1.57	0.04	-0.72	-0.80	0.78
DPM3	-1.31	-2.76	0.53	-2.37	-0.76	-0.33	0.09	-1.20
EIF1	-1.18	-2.31	-0.58	-1.47	-1.16	0.15	-0.65	0.33
GOLGA8N	-1.29	-1.20	-2.38	-0.34	0.23	-1.18	-0.36	-0.58
HIST1H2BL	-1.35	-0.78	-3.46	-0.08	-1.55	-0.71	-1.39	-0.19
HIST1H2BN	-1.39	-2.37	-1.85	0.04	-0.20	-2.78	-0.86	-0.07
HIST2H2AC	-0.38	0.35	-1.08	-2.00	-0.06	-0.82	-0.75	-0.42
ILK	-2.68	-2.04	-1.04	-1.66	0.21	-1.69	-0.25	-1.19
NAA30	-1.37	-1.41	-0.63	-0.70	0.10	-0.49	-0.45	-0.74
NPIPA5	0.31	-1.89	-1.46	-2.31	-0.38	0.30	-1.13	0.52
PAXBP1	-0.37	-1.34	-2.21	-3.85	0.50	0.00	-0.96	-1.26
PIKFYVE	-2.91	-2.30	0.17	-3.24	-0.18	-0.55	0.03	-0.86
RNF8	-0.93	-0.34	-3.43	-1.13	-0.48	0.16	-0.35	-1.21
RPN2	-1.06	-2.70	-1.05	-4.32	-0.96	0.16	-1.16	0.05
TMEM41B	-0.29	-1.73	-1.47	-2.29	0.11	-1.17	-0.82	-0.32
TOP1	-0.67	-1.73	-1.39	-1.24	0.12	-0.43	-0.10	-0.51
USP17L25	0.11	-0.59	-1.37	-1.46	-0.36	0.77	-1.52	-0.88
VPS37A	-1.73	-0.83	-0.15	-2.23	-0.39	0.31	-0.48	-0.50
ZNRD1	-4.02	-1.20	-1.79	0.06	-1.13	-0.80	-0.17	-0.44

In the second strategy, the gRNAs with a **gene score** of more than 50% depletion ($\log2 \leq -1$) in all cell lines were listed. Similar to above, for the analysis of H28 cell line, the mean value (-0.21) of negative fold changes had to be implemented. Again, the genes represented by less than 2 gRNAs were excluded from the resulting list. Finally, the genes that scored in common for

all three of the H2052, H2452, and H28 cell lines were determined. Similarly, the genes that co-scored with the MeT-5A cell line were excluded (Table 30).

Table 30. List of genes that scored in common in three MPM cell lines but co-scoring with MeT-5A cell line based on gene score.

Gene	MeT-5A			H052			H2452			H28		
	LFC	p value	FDR	LFC	p value	FDR	LFC	p value	FDR	LFC	p value	FDR
ATG9A	-0.44	0.11	0.74	-1.45	0.002	0.06	-1.43	0.023	0.26	-0.66	0.029	0.59
C19orf53	-0.33	0.24	1.00	-1.76	0.021	0.30	-2.07	0.004	0.07	-1.29	0.001	0.13
CCND1	-0.12	0.53	1.00	-2.14	0.000003	0.00	-1.55	0.011	0.15	-0.79	0.001	0.10
CDK2	-0.29	0.35	1.00	-1.53	0.001	0.03	-1.25	0.035	0.36	-0.37	0.130	0.95
GOLGA8N	-0.78	0.08	0.64	-1.20	0.020	0.30	-1.06	0.146	0.94	-0.47	0.135	0.96
HIST1H2BL	-0.78	0.13	0.82	-1.07	0.019	0.28	-1.87	0.060	0.54	-1.05	0.040	0.66
LOC100144595	-0.87	0.11	0.77	-1.07	0.019	0.28	-1.04	0.012	0.17	-1.05	0.102	0.90
NAA30	-0.71	0.10	0.70	-1.07	0.006	0.12	-1.78	0.003	0.06	-0.47	0.061	0.78
PAXBP1	-0.22	0.15	0.91	-1.30	0.002	0.05	-1.88	0.006	0.09	-0.48	0.072	0.83
RPN2	-0.84	0.02	0.19	-1.28	0.008	0.15	-2.56	0.000003	0.00	-0.46	0.082	0.86
RPS4X	-0.87	0.03	0.33	-2.28	0.0001	0.01	-1.39	0.055	0.51	-1.16	0.0003	0.06
TBC1D3H	-0.73	0.13	0.82	-1.27	0.0004	0.02	-2.19	0.0002	0.01	-0.66	0.018	0.49
TMED10	-0.82	0.11	0.76	-1.68	0.001	0.03	-2.19	0.0002	0.01	-2.07	0.000004	0.00
TMEM41B	-0.39	0.19	1.00	-1.12	0.004	0.10	-1.60	0.0005	0.01	-0.57	0.002	0.19
VPS37A	-0.16	0.65	1.00	-1.50	0.001	0.04	-1.28	0.033	0.34	-0.44	0.022	0.53

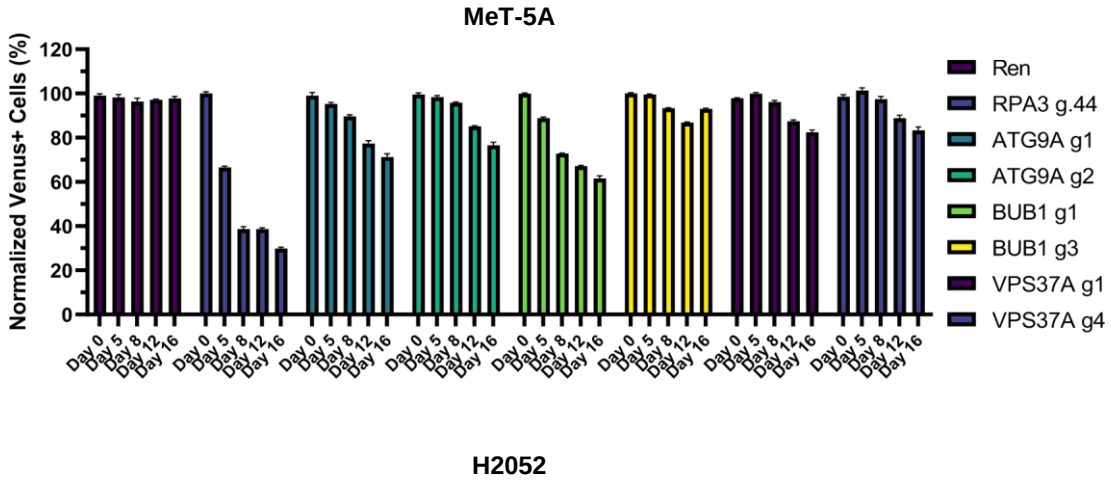
When combined, these two strategies enabled the identification of all the genes that emerged as an intersection and common cluster in the MPM cell lines, while excluding those that co-scored in the MeT-5A cell line. This list is composed of 30 genes (Table 31). One can note that among these genes are known common essential genes (*C19orf53, EIF1, HIST1H2BN, HIST2H2AC, NAA30, PAXBP1, RPN2, RPS4A, TBC1D3H*, and *TOP1*) (156). They are known to perform cell survival related functions in normal cells as well, thus resulting in their exclusion from future MPM-specific studies. In addition to these, manual curation was performed specific to the MeT-5A cell line, by controlling the gRNA and gene scores one by one, 11 other genes, namely *ALG5, CCNK, DCLRE1B, DPM3, GOLGA8N, HIST1H2BL, ILK, LOC100144595, RNF8, TMED10,* and *ZNRD1*, whose depletion were relatively high even though log2 ≥ -1 were excluded. After all these evaluations, a core list consisting of 9 genes (i.e., *ATG9A, BUB1, CCND1, CDK2, NPIPA5, PIKFYVE, TMEM41B, USP17L25*, and *VPS37A*) was obtained.

Table 31. The gene list that emerges as the intersection of two strategies.

ALG5	CCNK	GOLGA8N	LOC100144595	RNF8	TMEM41B
ATG9A	CDK2	HIST1H2BL	NAA30	RPN2	TOP1
C19orf53	DCLRE1B	HIST1H2BN	NPIPA5	RPS4X	USP17L25
BUB1	DPM3	HIST2H2AC	PAXBP1	TBC1D3H	VPS37A
CCND1	EIF1	ILK	PIKFYVE	TMED10	ZNRD1

4.11. Validation of Candidate Genes

The following approach was to validate the screen results and the cell survival essentiality of these genes. To achieve that, a competition assay was performed by individually targeting a select number of genes. In this assay, the *RPA3* gene, which is a common essential gene and shows depletion in all four cell lines was used as a positive control, and, *ATG9A*, *BUB1*, and *VPS37A* genes, with preferential depletion in MPM cell lines, were prioritized. In conclusion, the selective targeting of these genes with specific gRNAs revealed a positive correlation with the CRISPR-Cas9 screen results (Figure 32).



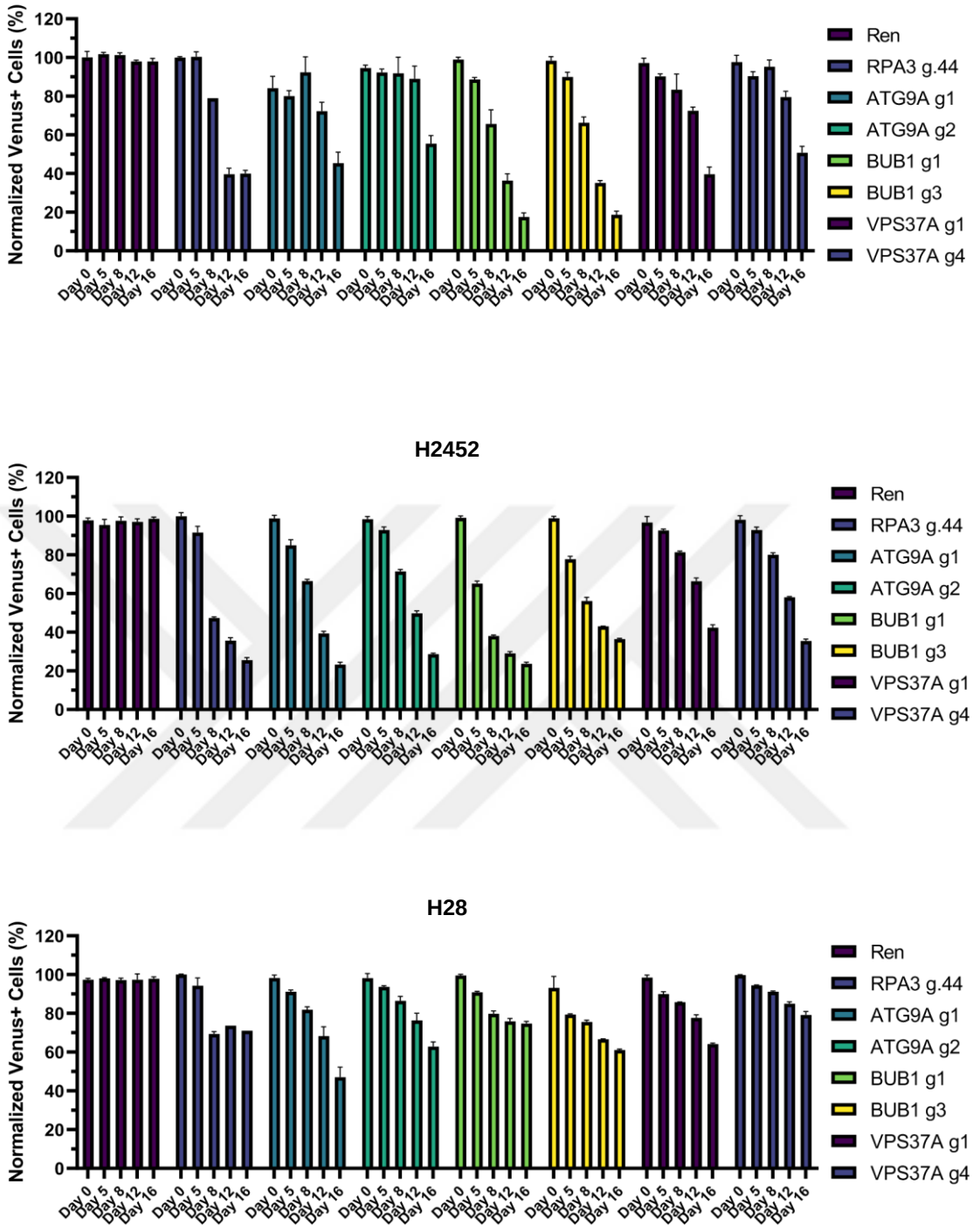


Figure 32. Competition assay results of MeT-5A, H2052, H2452, and H28 cells. The percentage of Venus positivity of Day 0 samples of each group was normalized to 100 and percentage of other days were normalized accordingly.

To select the gene(s) for future studies, specific interest was placed on the druggable factors/enzymes, and those that have increased expression in MPM with negative correlation on overall patient survival. To this end, as a first step, the association of 9 genes with survival

in MPM patients was examined. Specifically, the genes associated with patient survival in MPM tumor data (TCGA dataset consisting of 87 tumor samples) were searched on the UALCAN (157) and GEPIA (158) data analysis portals. The findings suggested that increased expression of *ATG9A*, *BUB1*, *CDK2*, *TMEM41B*, and *VPS37A* genes was negatively associated with survival (Figure 33).

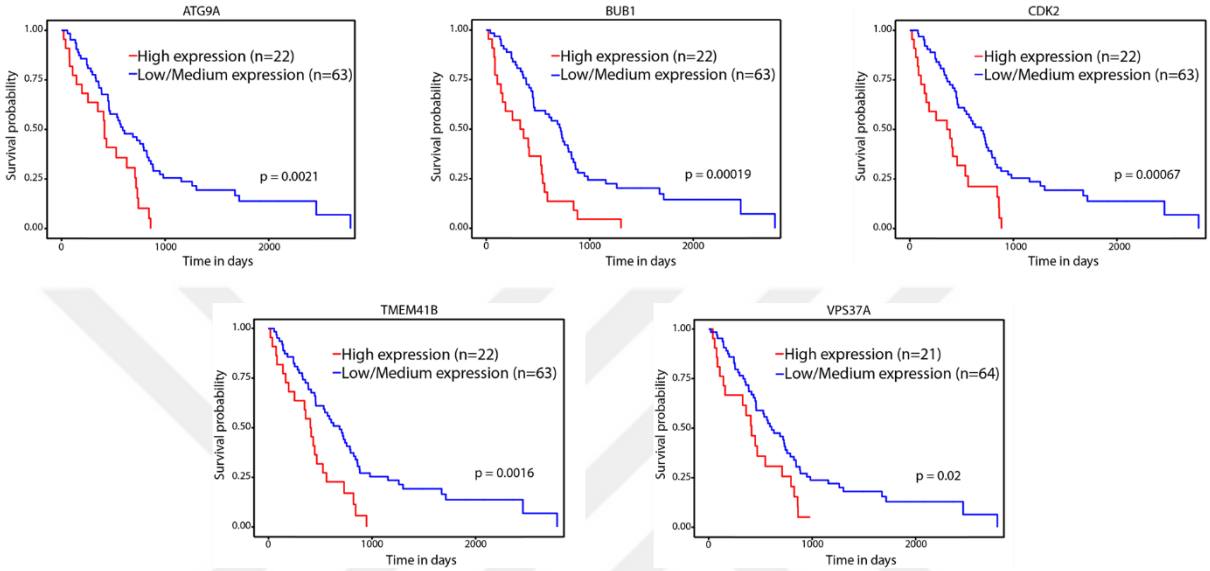


Figure 33. Survival analysis results of *ATG9A*, *BUB1*, *CDK2*, *TMEM41B* and *VPS37A* genes in the TCGA MPM dataset.

Next, the following criteria were considered: having been verified by DepMap, being an enzyme and a druggable molecule with no or limited studies in MPM. Based on this evaluation, the *BUB1* gene was selected for further studies (Table 32).

Table 32. Evaluation criteria for genes.

Gene	DepMap Score			Enzyme	Druggable	Previously worked in MPM
	H2052	H2452	H28			
ATG9A	-0.139	-0.630	-0.359	No	No	No
BUB1	-1.110	-0.733	-0.812	Kinase	Yes	No
CDK2	-0.657	-0.551	-0.189	Kinase	Yes	Yes
TMEM41B	-0.314	-0.650	-0.439	No	No	No
VPS37A	-0.774	-0.618	-0.462	No	No	No

4.12. *BUB1* is a Common Cancer Essential Gene

To corroborate our CRISPR-Cas9 screen findings, the effect of BUB1 depletion on the survival of MPM cell lines was investigated using DepMap portal's CRISPR, RNAi and Achilles project

data. This analysis demonstrated that BUB1 depletion has negatively affected the survival of all available MPM cell lines (Figure 34A,B,D). More importantly, *BUB1* was identified as a common essential gene in the CRISPR project data of DepMap (Figure 34C).

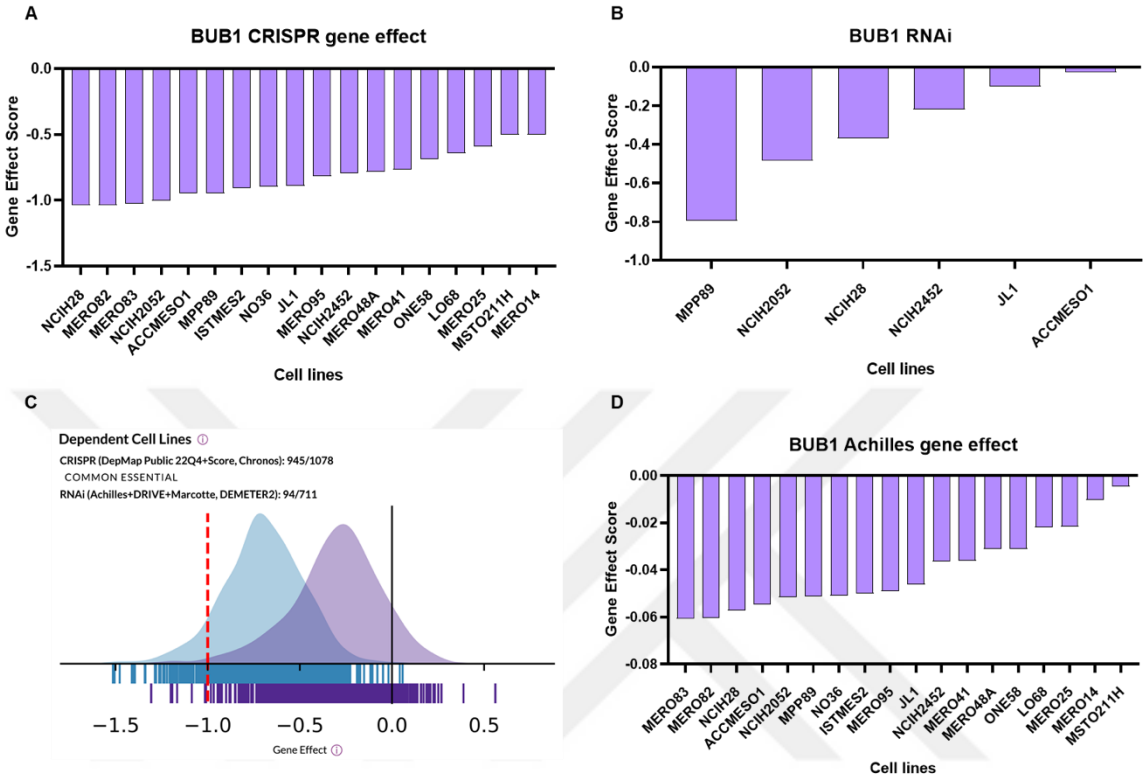


Figure 34. *BUB1* gene effect scores of different project data from DepMap portal.

To provide an initial assessment for the validity of *BUB1* selection in MPM, the levels of BUB1 expression were investigated in pan-cancer TCGA datasets by using GEPIA (159) (Figure 35). BUB1 expression was significantly increased in most of the tumor tissues compared with their matching normal samples. These results propose a critical role for *BUB1* in cancer.

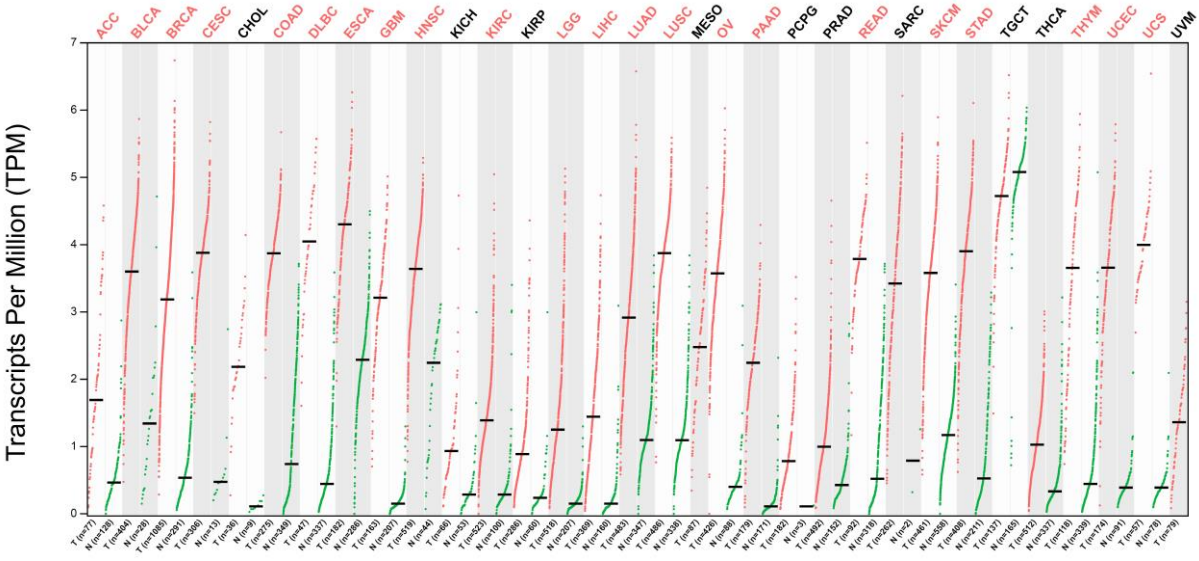


Figure 35. BUB1 expression levels of different tumor tissues compared with their matching normal samples. Data was extracted from GEPIA by using TCGA matched normal and GTEx data. ANOVA was used for statistical analysis (log2FC cutoff 1, q value cutoff 0.01).

To understand the level of BUB1 expression in MPM relative to other cancer types (Figure 36) as well as cancer cell lines (Figure 37), further analyses were conducted using GEPIA and Cancer Cell Line Encyclopedia (CCLE) RNA-Seq expression, respectively. The data showed that the levels of BUB1 in MPM was not above mean of several cancer types, yet it was not among the low-expression cancers either.

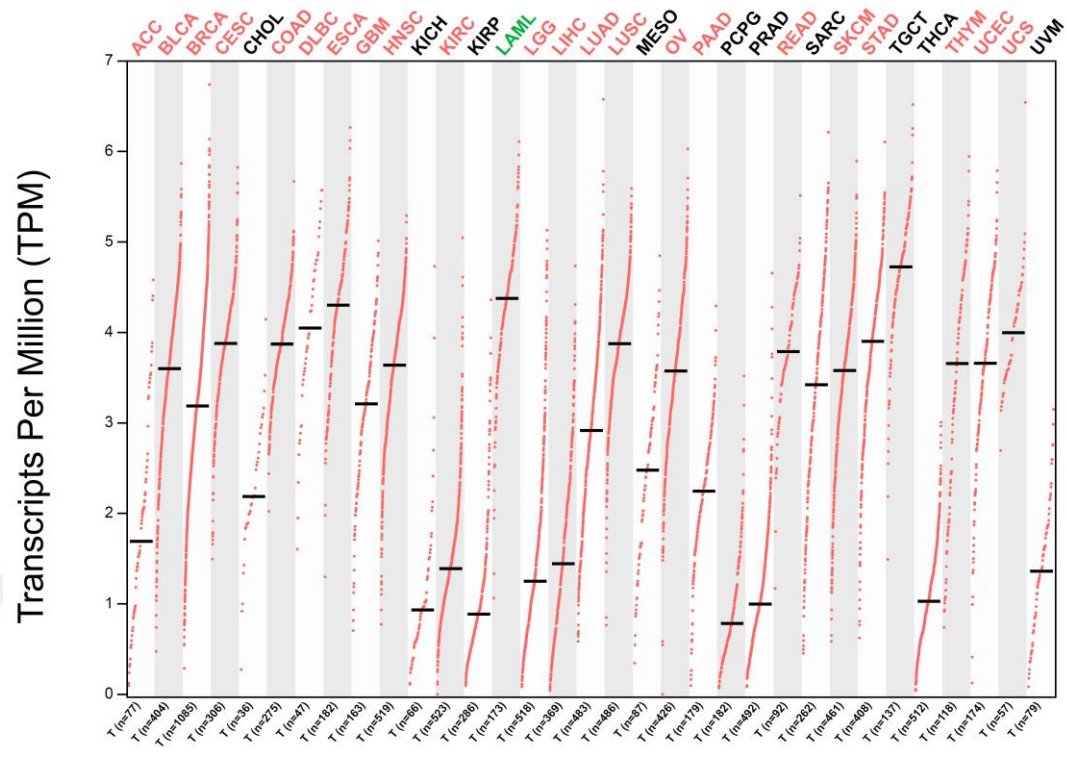


Figure 36. BUB1 expression levels of different tumor tissues along with mesothelioma. Data was extracted from GEPIA by using only tumor data. ANOVA was used for statistical analysis (log2FC cutoff 1, q-value cutoff 0.01).

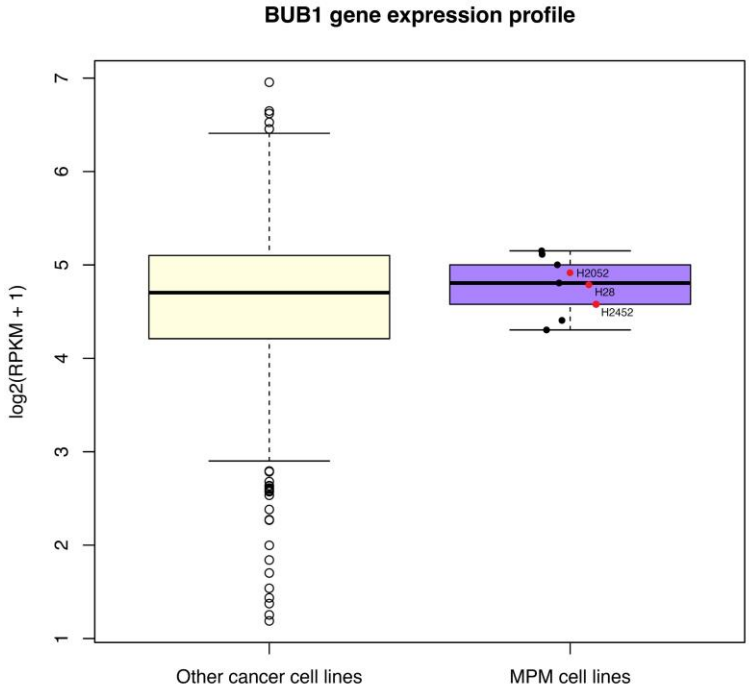


Figure 37. BUB1 expression levels of different cancer cell lines compared to MPM cell lines. Data was extracted from CCLE RNA-Seq expression data. (RPKM: reads per kilobase).

As shown in Figure 35, the MPM TCGA dataset is devoid of any matching normal samples. Therefore, to provide a comparative BUB1 expression analysis of tumor vs normal tissues in the MPM setting, several Gene Expression Omnibus (GEO) datasets were extracted and interrogated. The analyses of GSE2549, GSE42977, GSE51024, and GSE117668 revealed that BUB1 expression was significantly elevated in MPM tissues compared to normal mesothelial tissues in all datasets analyzed (Figure 38).

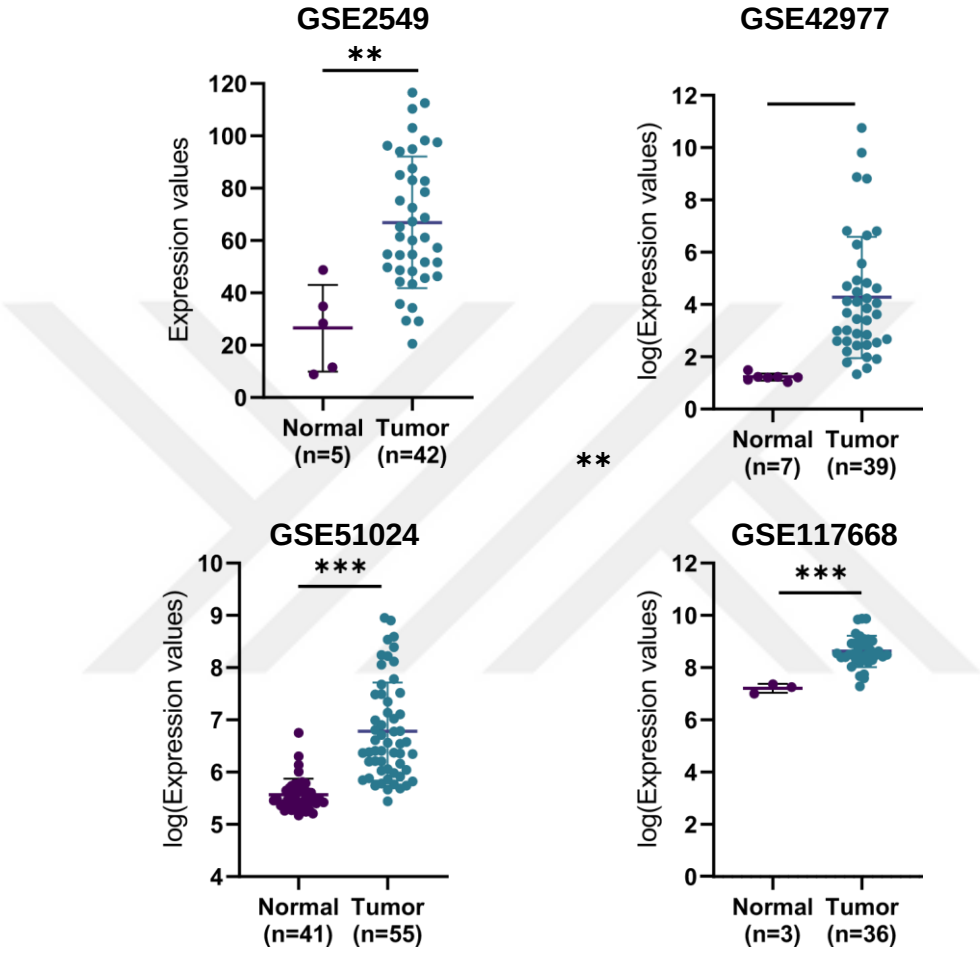


Figure 38. BUB1 expression levels of tumor tissues from different GSE datasets compared with their matching normal samples. Data was extracted from GEO dataset. **p<0.01, ***p<0.001, Student's t-test.

Before conducting the cellular and molecular studies on BUB1 significance in MPM, an extended competition assay targeting the *BUB1* gene with four different gRNAs was performed in H2052, H2452 and H28 cell lines. To this aim, gRNA1 and gRNA3, which are numbered according to the gRNA order in the library contents file provided by Addgene, from the Brunello library and two additional gRNAs, one from each of the GeCKO (160) and Sabatini

(161) libraries, were selected. The two new gRNAs were named as gRNA5 and gRNA6, respectively, and were cloned separately into the pECPV vector. In line with our earlier findings, the extended competition assay further confirmed that BUB1 depletion attenuates MPM cell survival (Figure 39).

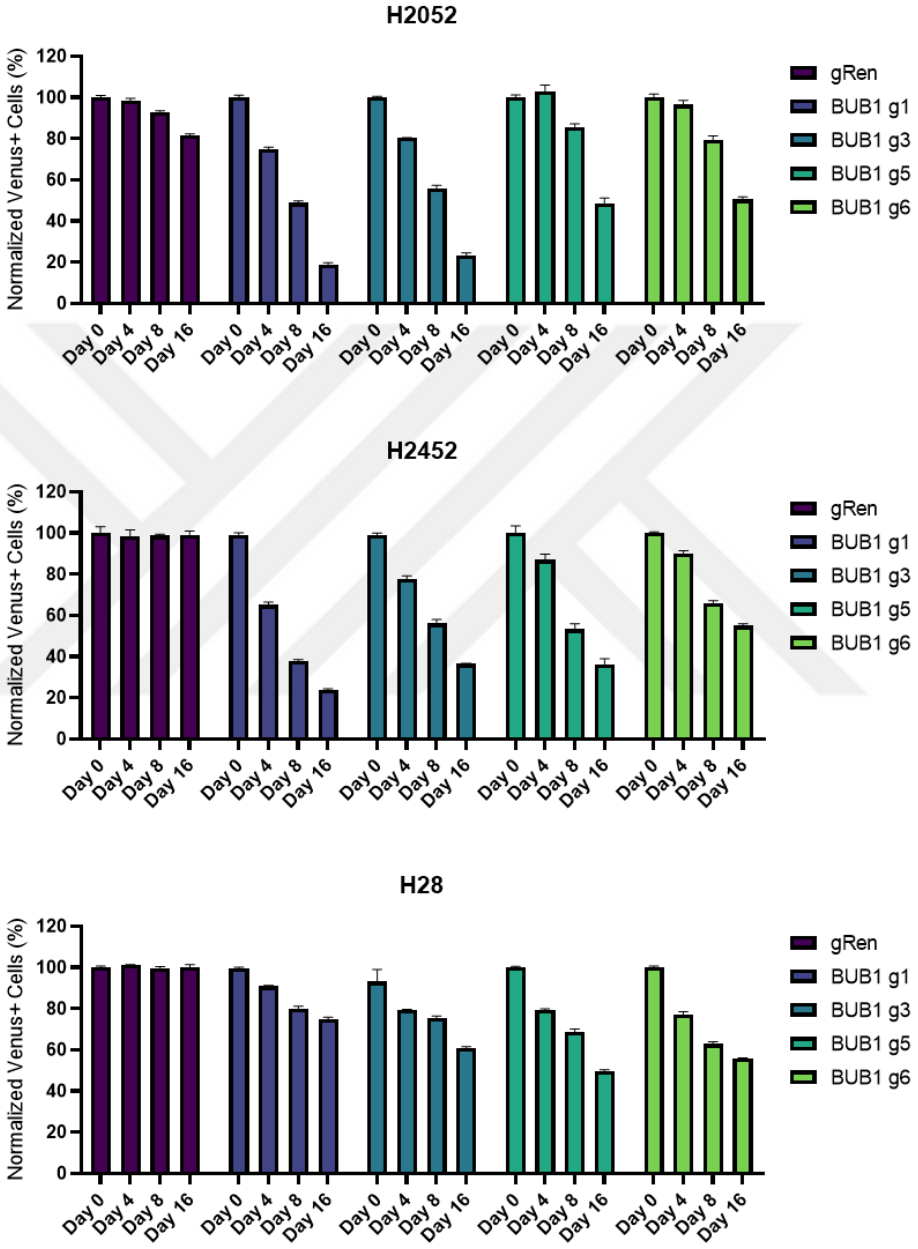


Figure 39. Competition assay results of H2052, H2452, and H28 cells. While percentage of Venus positive cells infected with gRen showed slight changes, this value decreased over time in cells infected with BUB1 gRNAs. The percentage of Venus positivity of Day 0 samples of each group was normalized to 100 and percentage of other days were normalized accordingly.

4.13. Generation of Polyclonal *BUB1* Knockout Cells

To gain primary insights into the molecular role of *BUB1* in MPM cell survival, the proliferation and 2D colony formation patterns were analyzed in BUB1 depleted and negative control cells. These experiments were performed with relevant gRNAs that were cloned into the lentiCRISPRv2 vector. Furthermore, the H2052, H2452, and H28 cell lines were infected with lentiviral particles and selected with puromycin to generate *BUB1* knockout cells with polyclonal nature. The level of BUB1 depletion was confirmed by western blot (Figure 40). Based on these results, gRNA3 and gRNA5 with the highest knockout effect were selected for further experiments.

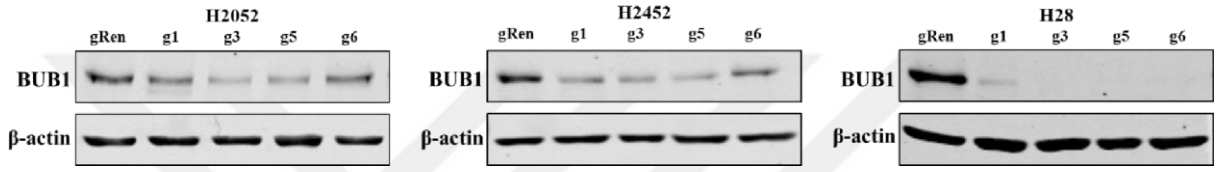


Figure 40. Western blot results of control and *BUB1* knockout H2052, H2452, and H28 cell lines.

Immunofluorescence staining of *BUB1* targeted cells further confirmed the polyclonality of knockout cells. As expected, as reported in the literature, BUB1 was localized in both the cytoplasm and the nucleus in gRen targeted cells, yet BUB1 depleted cells displayed diminished staining patterns (Figure 41).

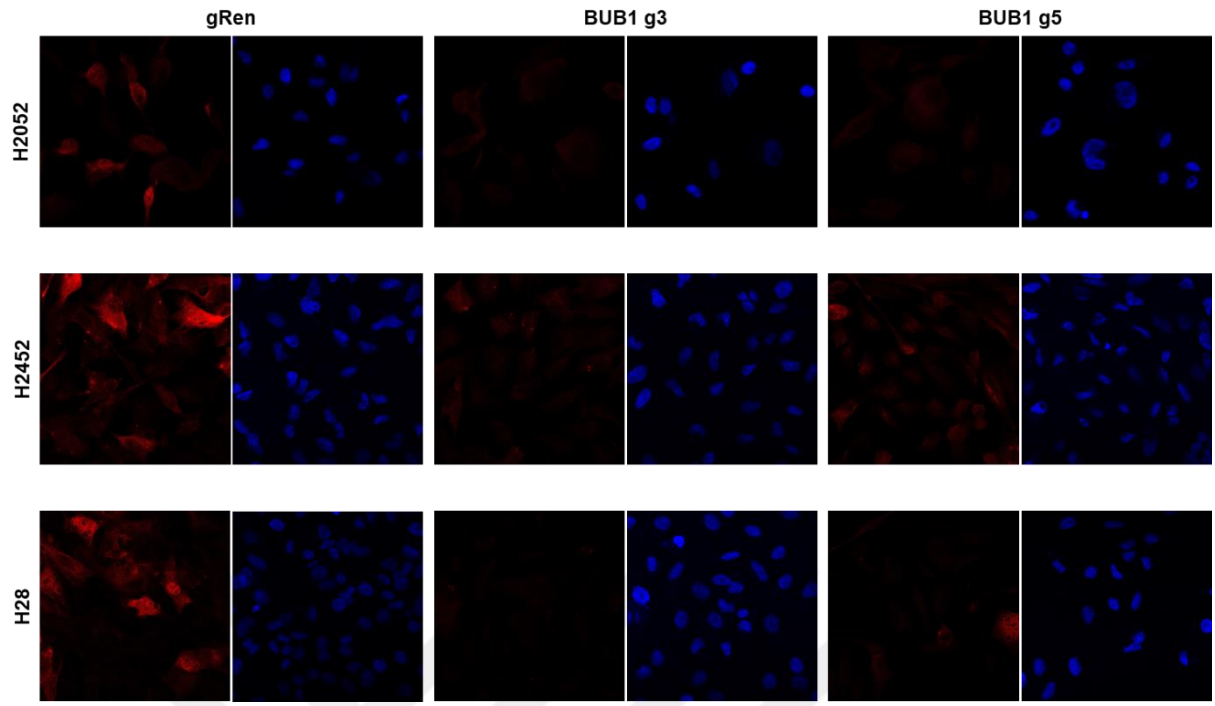


Figure 41. Immunofluorescence (IF) staining of control and BUB1 in knockout H2052, H2452, and H28 cell lines (40X magnification).

4.14. *BUB1* Knockout Attenuates MPM Cell Proliferation and 2D Colony Formation

To determine the impact of *BUB1* knockout on cell proliferation, three experimental strategies were followed. It is of particular importance to mention here that our earliest findings (both competition assays and experimental optimization studies) indicated that *BUB1* gene was critically important for the survival of MPM cells and the growth of BUB1 depleted cells decreased over time. Based on these primary observations, the experiments were carried out within 2-3 weeks of clone generation. To start with, MTT assay was performed. Cells were seeded into four 96-well plates and MTT measurements were performed every 2 days. As shown in Figure 42, BUB1 depleted cells displayed significantly reduced proliferation rates when compared to that of gRen control cells.

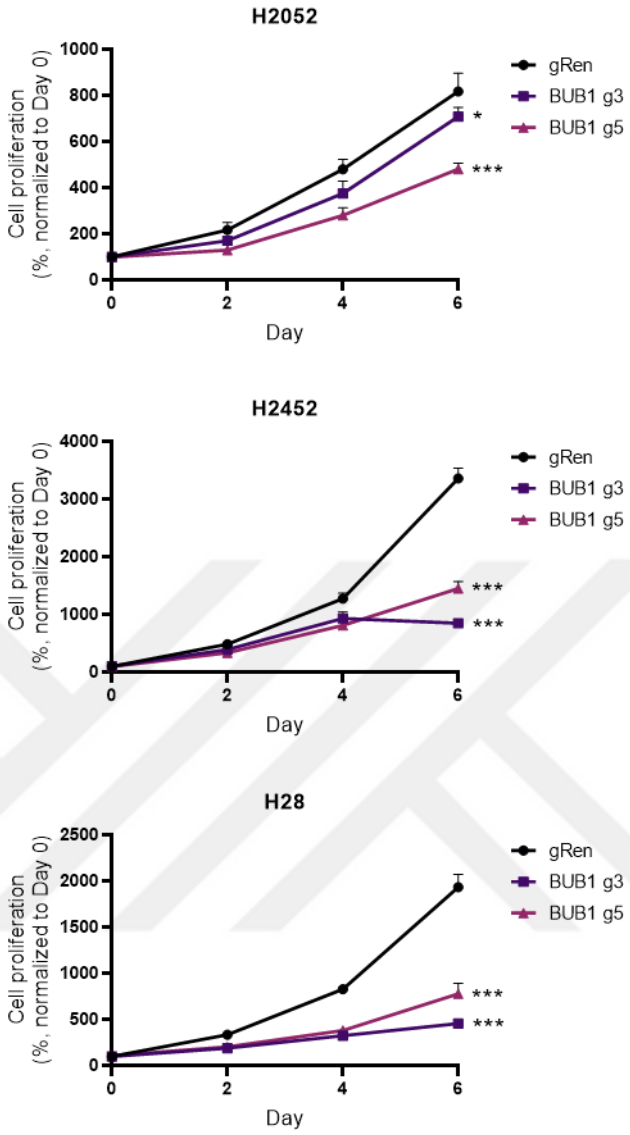


Figure 42. Cell proliferation profiles of control and *BUB1* knockout H2052, H2452, and H28 cell lines. MTT measurements were performed every 2 days starting 2 days after cell seeding (Day 0). Day 0 measurements were normalized to 100 and percentage of other days were normalized accordingly. Mean ±SD, n=4, ***p<0.001, Student's t-test.

Next, the effect of BUB1 depletion in proliferative index was determined by BrdU incorporation assay. BrdU (bromodeoxy uridine) is a synthetic thymidine analog which incorporates into replicating DNA during the S-phase of the cell cycle. BrdU positivity of proliferating cells is detected via immunocytochemical staining procedures (162). Following cell seeding on cover slips, cells were labelled with BrdU for 12 h. In agreement with the MTT results, the proliferation rate of BUB1 depleted cells was significantly decreased when compared to gRen cells (Figure 43).

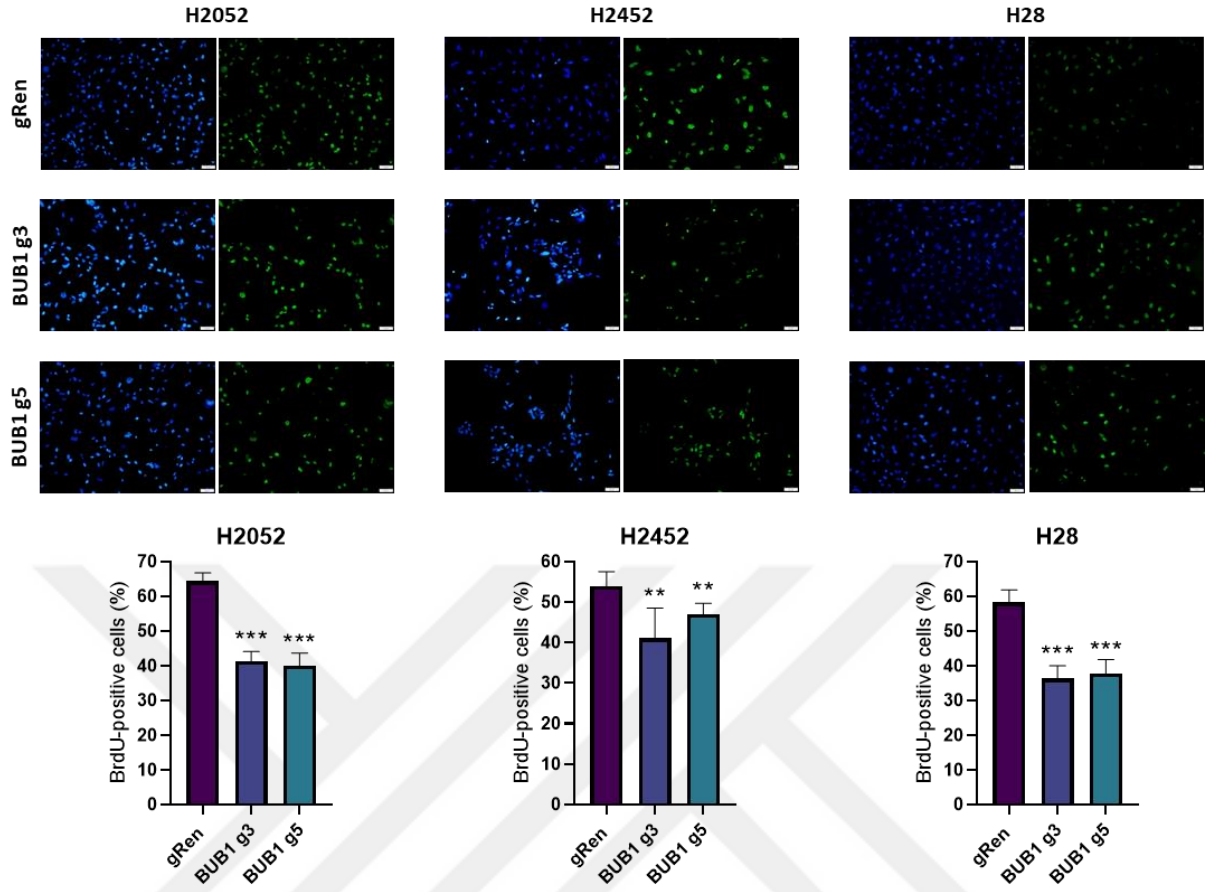


Figure 43. BrdU incorporation of control and *BUB1* knockout H2052, H2452, and H28 cell lines. DAPI and BrdU stained cells were counted and the percentage of BrdU-positive cells was calculated by proportioning the number of cells stained with BrdU to the number of cells stained with DAPI. 20X magnification, scale bar represents 50 µm. Mean ±SD, n=6, **p<0.01, ***p<0.001, Student's t-test.

Thirdly, a 2D colony formation assay was performed to assess how *BUB1* knockout affects colony-forming ability of MPM cells. For this purpose, 600 cells were seeded in each well of 12-well plates and allowed to form colonies for 10-14 days. When compared to gRen cells, *BUB1* knockout cells had a significantly lower 2D clonogenic capacity (Figure 44).

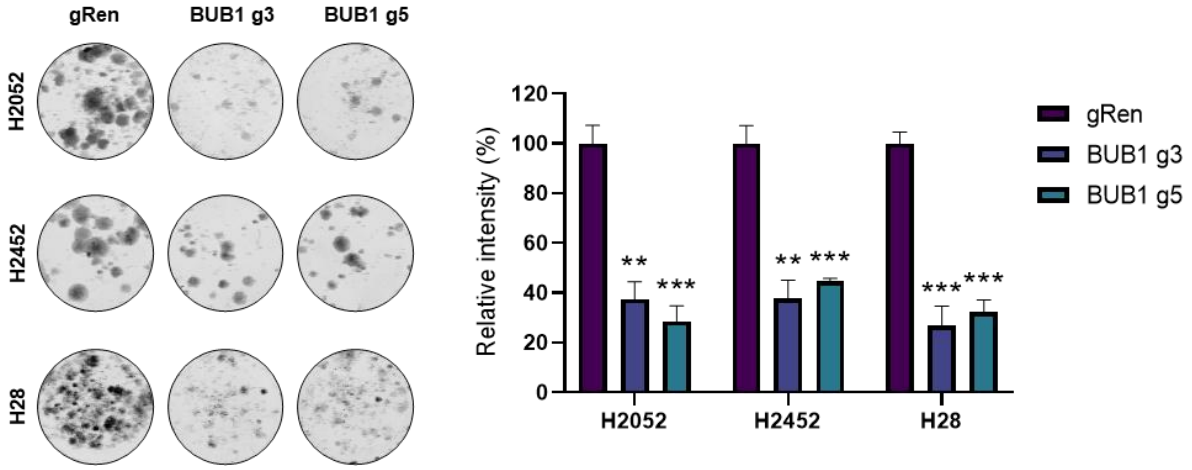


Figure 44. Colony formation assay results of *BUB1* knockout H2052, H2452, and H28 cell lines. Relative intensity was calculated by proportioning the intensities of knockout cells to gRen cells. Mean ±SD, n=3, **p<0.01, ***p<0.001, Student's t-test.

4.15. *BUB1* Knockout Decreases 3D Anchorage Independent Growth of MPM Cells

Having studied the phenotypes on 2D cell growth, the effect of BUB1 depletion on 3D anchorage independent growth was evaluated using a soft agar colony formation assay. Cells were seeded in 12-well plates in 0.3% noble agar and allowed to form colonies for 21 days. Then, colonies were imaged using light microscopy and the colony sizes were quantified using ImageJ. Colonies with diameter greater than 35 µm were counted. In conclusion, *BUB1* deficient cells had considerably reduced 3D colony-forming potential as compared to gRen cells (Figure 45).

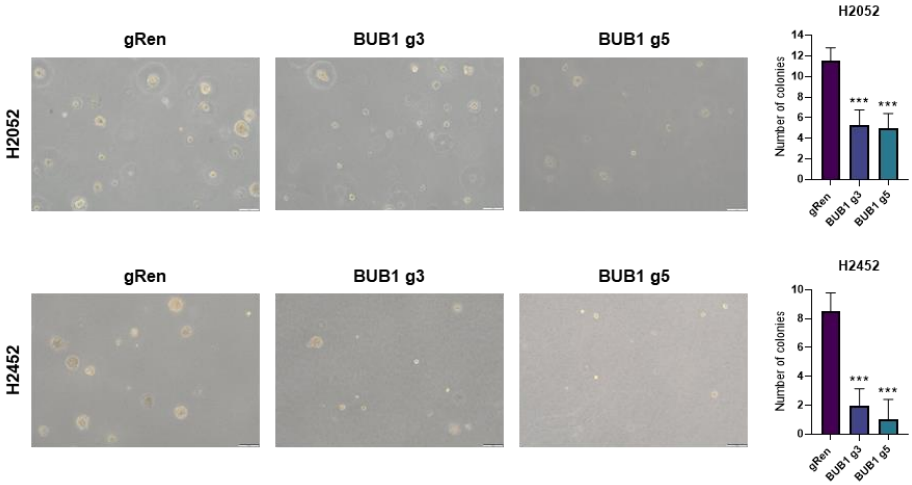


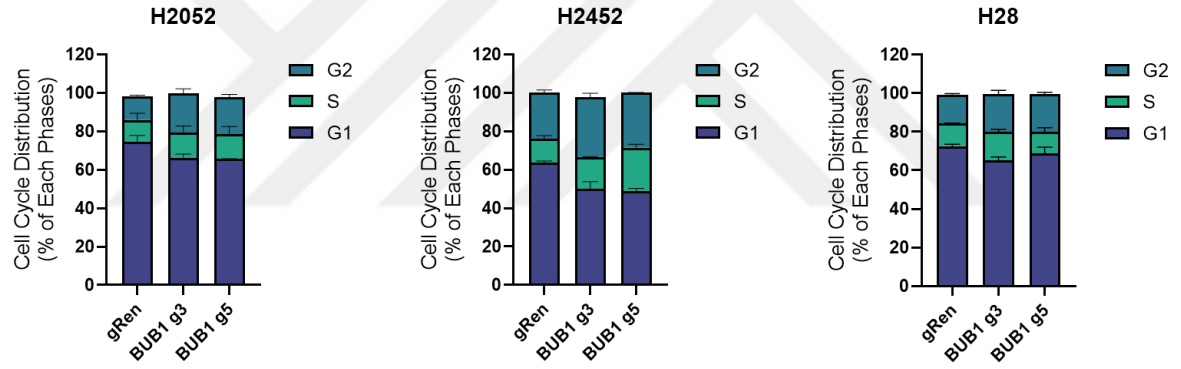
Figure 45. Soft agar images showing the effect of *BUB1* knockout on 3D anchorage independent growth of H2052, H2452, and H28 cells. Colonies with diameter greater than 35 µm were

counted. 10X magnification, scale bar represents 100 µm. Mean±SD, n=4, ***p<0.001, Student's t-test.

4.16. Multiple Mechanisms Underlie the Proliferation Reduction upon *BUB1* Knockout

4.16.1. BUB1 Knockout Causes Cell Cycle Arrest in the G2 Phase

To functionally dissect the cellular and molecular mechanisms underlying the effects of *BUB1* knockout on cell proliferation and growth, further experiments were conducted. First, the cell cycle profiles were examined. To achieve this, cells that were pre-seeded into 6-well plates were stained with propidium iodide (PI). Notably, PI is a fluorescence probe and a DNA intercalating agent that is commonly employed in various techniques to stain DNA (162). As shown in Figure 46, *BUB1* deficient MPM cells displayed significant cell cycle arrest in the G2 phase. In addition, H2452 BUB1 depleted cells had considerably higher cell populations in the S phase of cell cycle.



	gRen	BUB1 g3	BUB1 g5
G1	74.6±2.7	66±1.7	67.7±3.2
S	11.47±2.8	13.3±2.8	13.1±3.1
G2	12.35±0.4	20.7±1.7	19.2±1.2

	gRen	BUB1 g3	BUB1 g5
G1	63.6±0.7	49.99±3.1	51.9±1.2
S	12.43±1.3	18.9±0.2	20.87±1.4
G2	23.97±1.2	31.11±1.7	27.23±0.2

	gRen	BUB1 g3	BUB1 g5
G1	73.12±0.6	65.33±1.1	69.2±2.4
S	11.83±0.2	15.1±1	11.23±1.7
G2	15.05±0.3	19.57±1.5	19.57±0.7

Figure 46. Cell cycle distribution of *BUB1* knockout H2052, H2452, and H28 cells. Mean ±SD, n=3, two-way ANOVA multiple comparison.

These results suggested that BUB1 expression may be associated with increased expression of genes involved in the cell cycle. To investigate this, BUB1 mRNA levels were compared with gene sets from three GEO datasets. Results showed low BUB1 expression is correlated with low expressions of the important transcription factors for the G1/S transition, E2F and MYC (Figure 47).

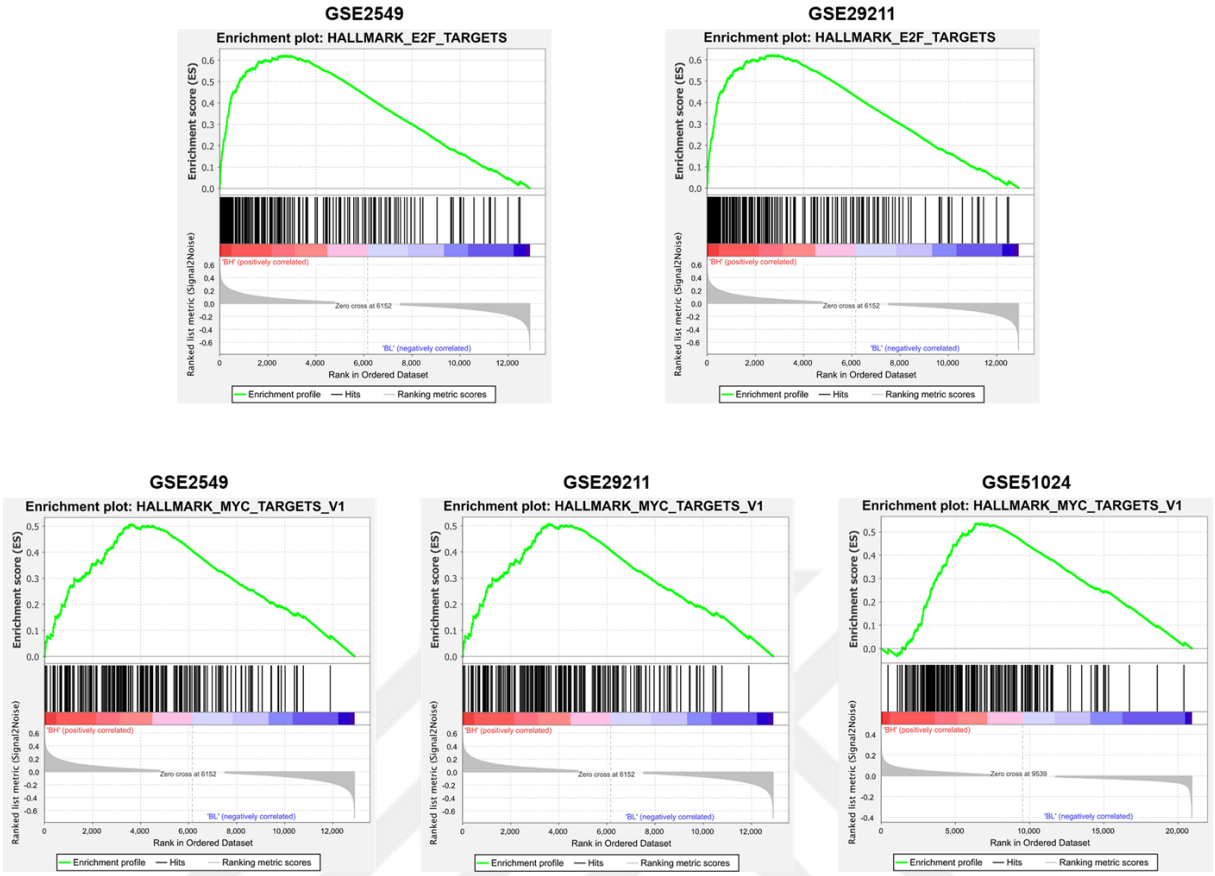


Figure 47. Gene set enrichment analysis of transcription factors important for the G1/S transition, E2F and MYC, in BUB1 low and high MPM samples.

4.16.2. BUB1 Knockout Increases Cellular Senescence

Cellular senescence is considered as an irreversible withdrawal from the cell cycle (163). Given the changes in cell cycle profiles, we wondered whether BUB1 depletion causes cellular senescence in MPM cells. To accomplish this goal, the senescence-associated betagalactosidase (SA-β-Gal) activity, an enzymatic biomarker of senescent cells, was quantified. Cells that were pre-seeded into 12 well plates were stained with SA-β-Gal staining solution for 12 h. As illustrated in Figure 48, *BUB1* knockout resulted in a significant increase in the cellular senescence phenotype (blue staining). It is important to note, however, that the mean increase in the number of senescent cells was minimal, implying that the overall contribution of this phenotype to growth suppression is rather modest and that other phenotypes may be implicated in this process.

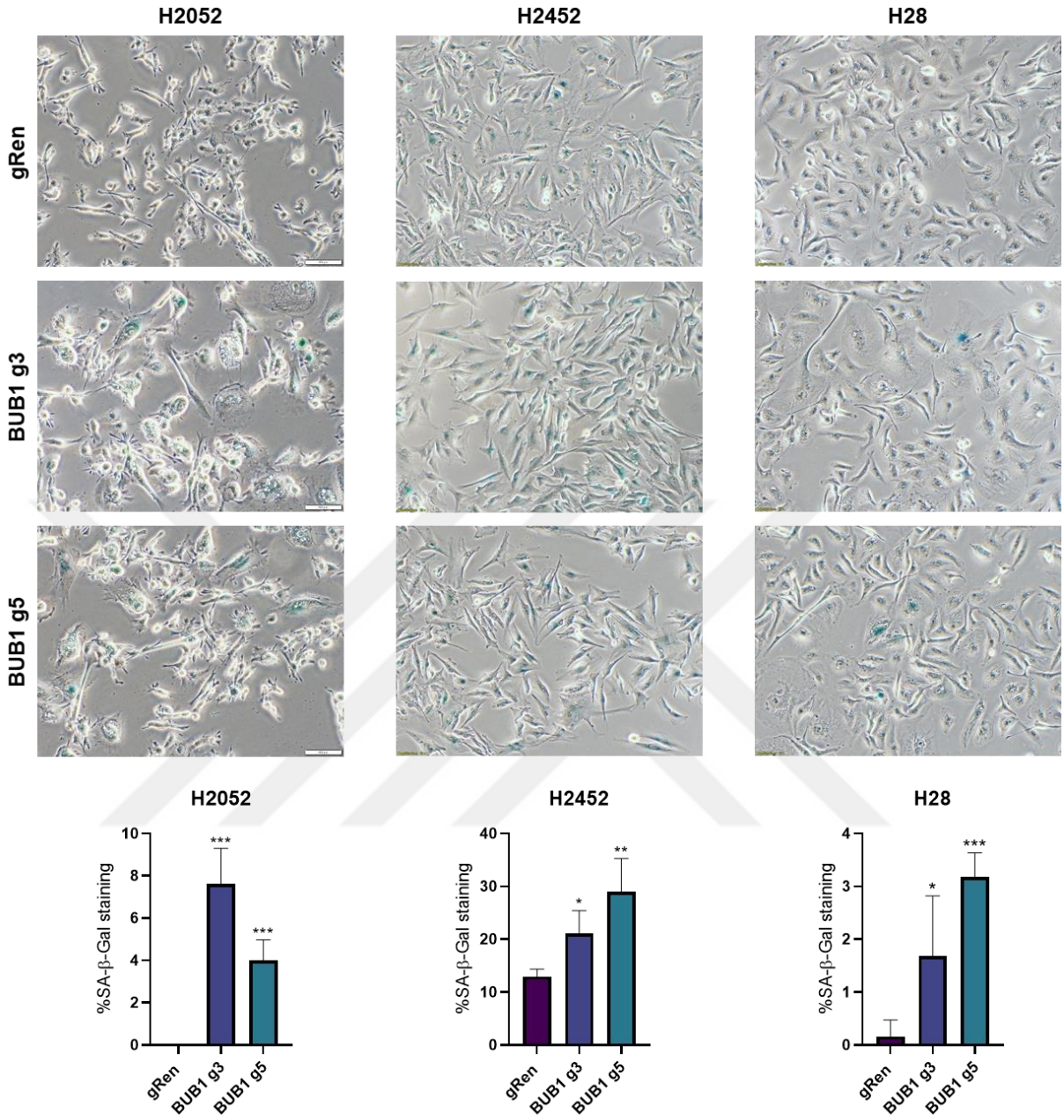


Figure 48. SA-β-Gal staining results of control and *BUB1* knockout H2052, H2452, and H28 cells. All cell population as well as SA-β-Gal stained cells were counted and the percentage of SA-β-Gal staining was calculated by proportioning the number of stained cells to the total number of cells. 10X magnification, scale bar represents 100 µm. Mean ±SD, n=5, *p<0.05, **p<0.01, ***p<0.001, Student's t-test.

4.16.3. *BUB1 Knockout Increases Apoptosis*

Because BUB1 deletion causes a strong depletion in cell populations, the apoptotic cell death phenotype was also investigated. To this end, cells were stained and examined for apoptosis

using the Annexin V/propidium iodide kit. As a result, with the exception of H28 BUB1 g5 cells, all cell lines displayed a modest but significant increase in apoptosis when compared to gRen cells (Figure 49).

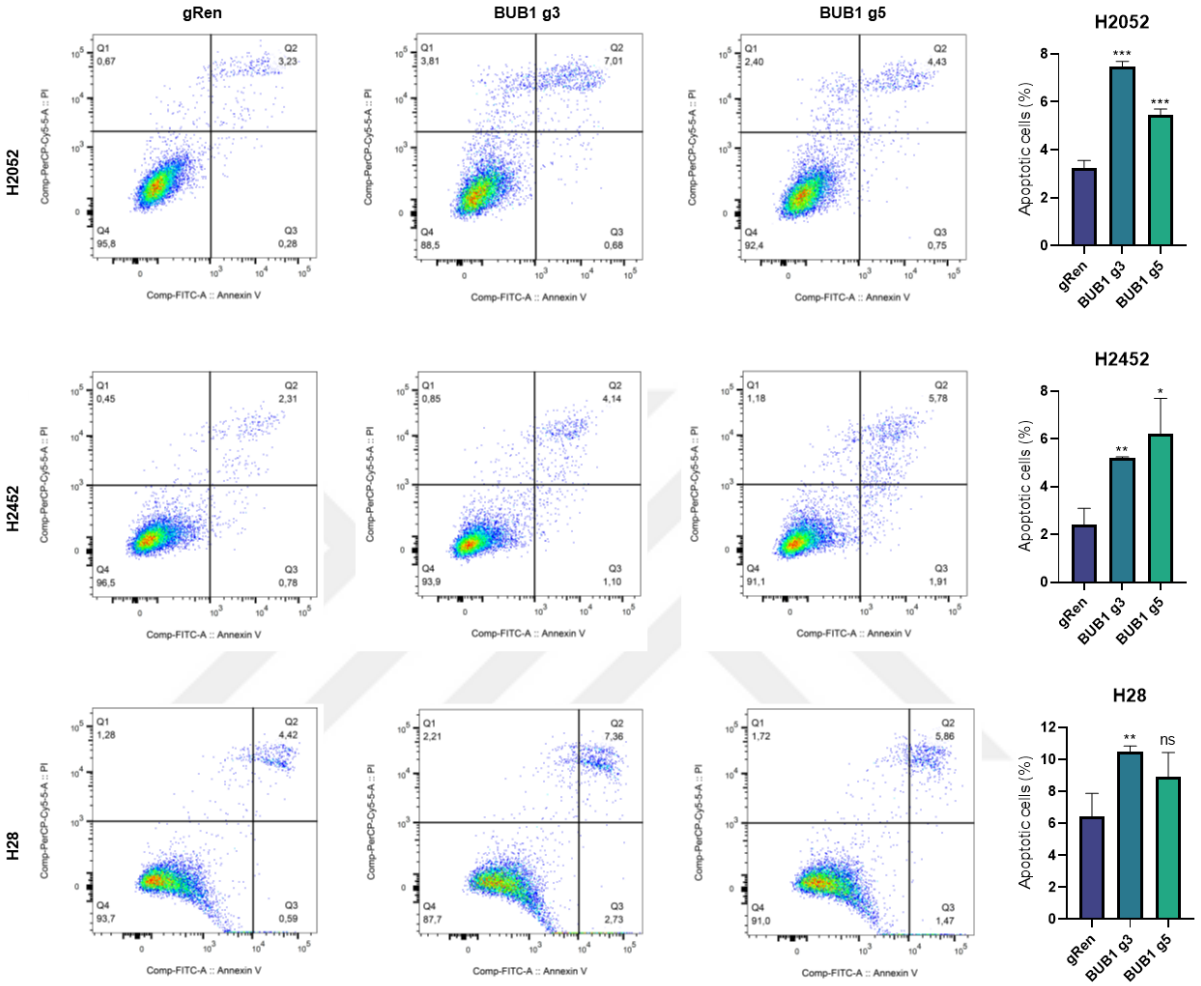


Figure 49. Flow cytometry analysis of apoptosis of control and *BUB1* knockout H2052, H2452, and H28 cells. Percentage of apoptotic cells was calculated as the sum of early (Q3) and late (Q2) apoptosis. The images that best represent the average are given. Mean ±SD, n=3, *p<0.05, **p<0.01, ***p<0.001, ns: not significant, Student's t-test.

4.17. *BUB1* Knockout Decreases Migration and Invasion Capacity of MPM Cells

Having demonstrated that *BUB1* knockout suppresses MPM cell survival and growth, we then investigated whether its deletion has an effect on other aggressive cancer cell phenotypes, in particular, migration and invasion. To this end, the rates of migration and invasion of *BUB1* deficient cells were studied. For these assays, cells were seeded into matrigel-free or matrigelcoated transwell inserts to assess their migration and invasion potentials, respectively.

After 48 h of seeding, cells were stained with crystal violet and migrated or invaded cells were quantified by manual counting. In conclusion, BUB1 depletion was found to dramatically attenuate MPM cell migration (Figure 50) and invasion (Figure 51).

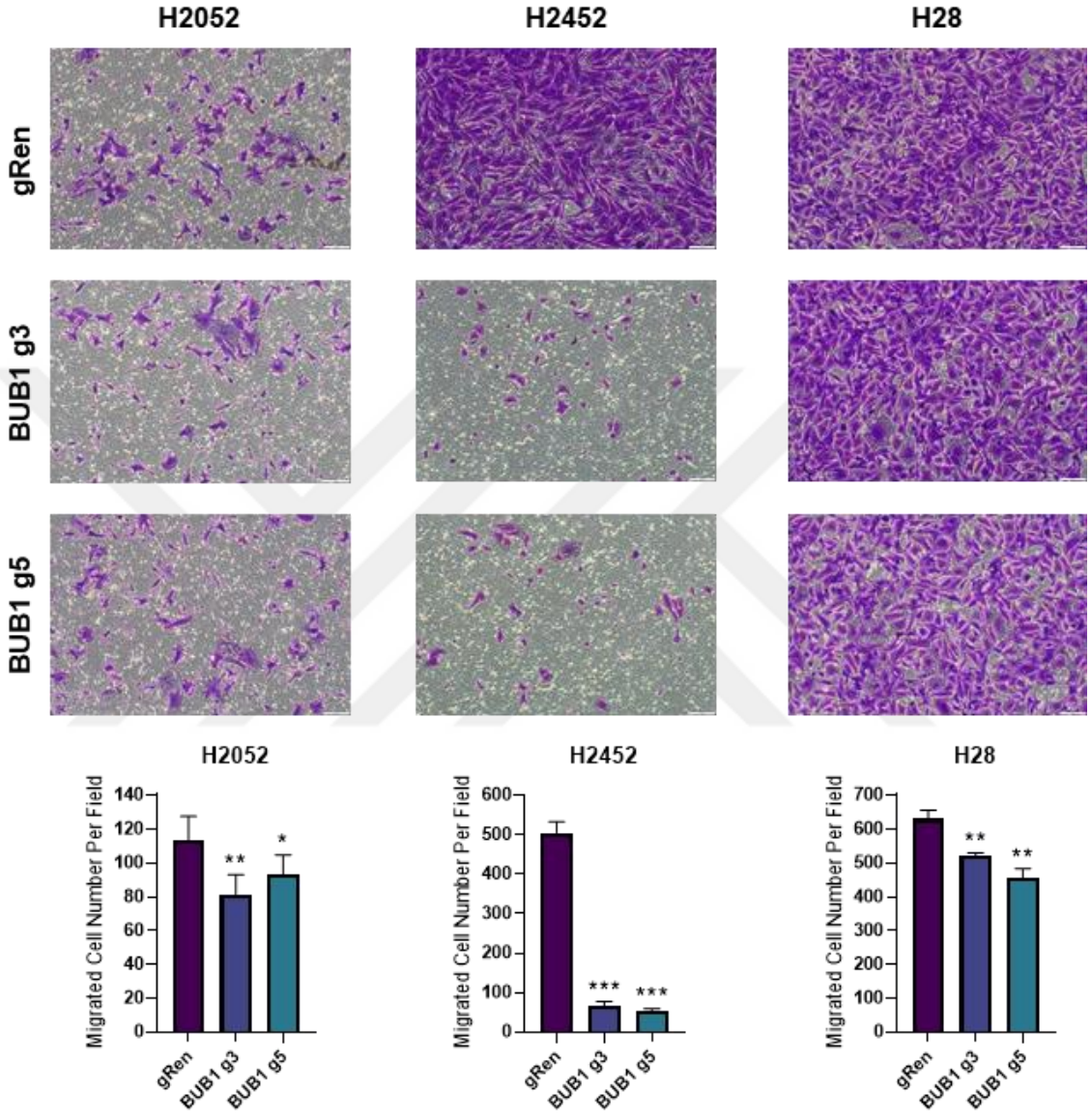


Figure 50. Migration assay results of control and *BUB1* knockout H2052, H2452, and H28 cells. 10X magnification, scale bar represents 100 µm. The data is presented as mean ±SD (n=6). *p<0.05, **p<0.01, ***p<0.001, Student's t-test.

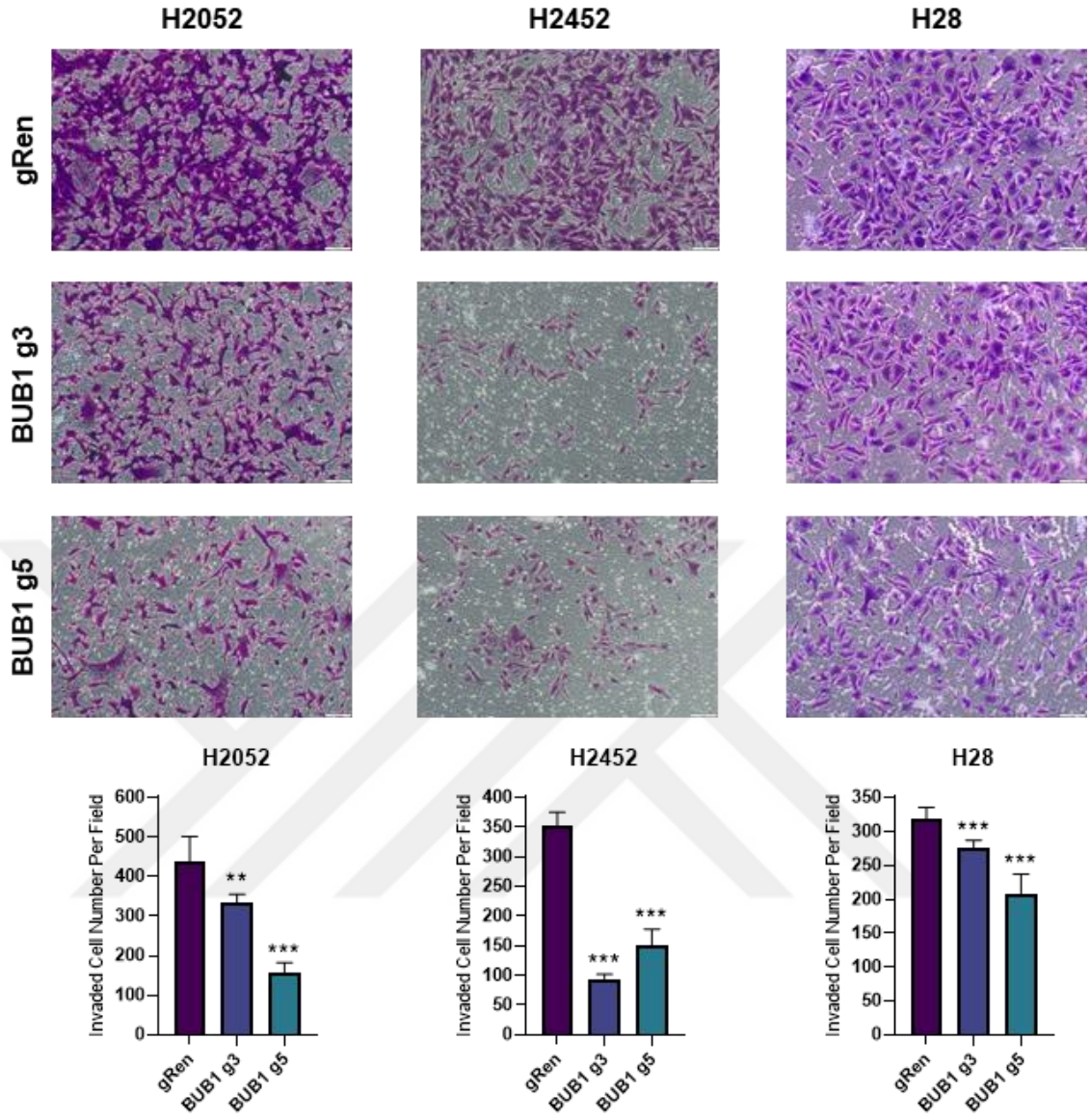


Figure 51. Invasion assay results of control and *BUB1* knockout H2052, H2452, and H28 cells. 10X magnification, scale bar represents 100 µm. Mean ±SD, n=6, **p<0.01, ***p<0.001, Student's t-test.

4.18. *BUB1* Knockout Reduces *In vivo* Tumor Engraftment Potential of MPM Cells

To investigate the significance of BUB1 deficiency on tumorigenesis, H2052 cells infected with gRen and BUB1 g3 gRNAs were transplanted subcutaneously into the right flanks of six athymic nude (NU/J) mice. Cells bearing *BUB1* deletion tended to form tumors in fewer animals than gRen cells (Table 33). Additionally, protein isolation was performed and *BUB1* knockout of tumor samples was confirmed by western blot (Figure 52).

Table 33. Tumor formation capacity of H2052 gRen and BUB1 g3 cells.

Group	Number of Animals with Palpable Tumors	Mean tumor volume (mm^3)
gRen	5/6	87.8
BUB1 g3	2/6	76.8

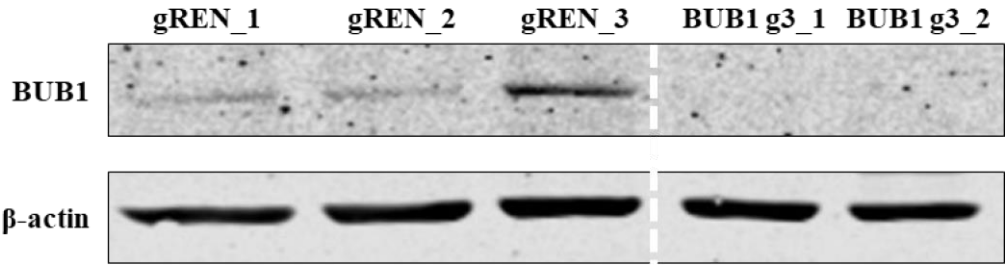


Figure 52. Western blot results of excised tumor samples. gRen and BUB1 g3 samples were run on nonconsecutive lanes.

4.19. BUB1 Overexpression Increases Proliferation and 2D Colony Formation Capacity of MPM Cells

After demonstrating that *BUB1* knockout attenuates the proliferation, growth, and aggressive cancer characteristics of MPM cells, we aimed to corroborate these results by overexpressing the *BUB1* gene in H2052 and H2452 cell lines. For this aim, *BUB1* coding sequence obtained from pBI-GFP-Bub1-wt vector was cloned into the pHIV-ZsGreen backbone. After lentiviral packaging of control (i.e., Empty) and BUB1 expressing (i.e. BUB1) vectors, H2052 and H2452 cell lines were infected and enriched against ZsGreen positivity by FACS sorting. Protein isolation was performed and BUB1 overexpression was confirmed by western blot (Figure 53).

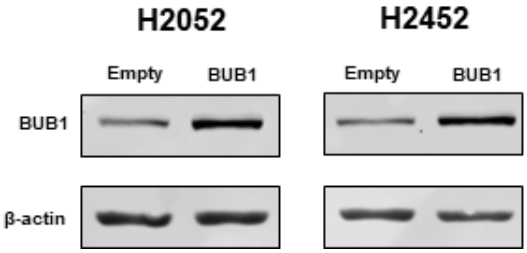


Figure 53. Western blot results of control (empty vector) and BUB1 overexpressing H2052, and H2452 cell lines.

To assess the effect of BUB1 overexpression on proliferative index, BrdU labeling assay was performed. The proliferation rate of BUB1 overexpressing cells was significantly higher compared to control cells with Empty vector (Figure 54).

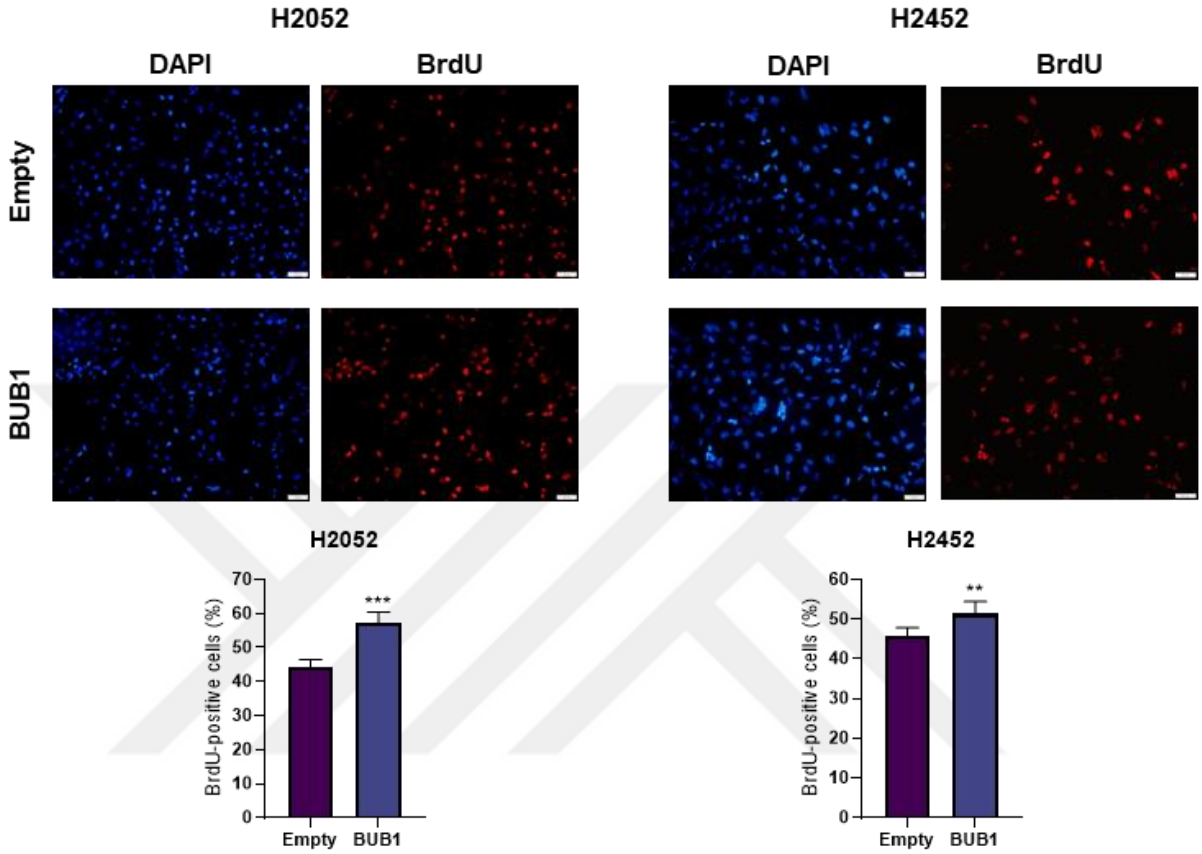


Figure 54. BrdU incorporation of control and BUB1 overexpressing H2052, and H2452 cells. DAPI and BrdU stained cells were counted, and the percentage of BrdU-positive cells was calculated by proportioning the number of cells stained with BrdU to the number of cells stained with DAPI. 20X magnification, scale bar represents 50 μm. Mean ±SD, n=6, **p<0.01, ***p<0.001, Student's t-test.

Similarly, BUB1 overexpression increased 2D colony-forming capacity of H2052 and H2452 MPM cells (Figure 55).

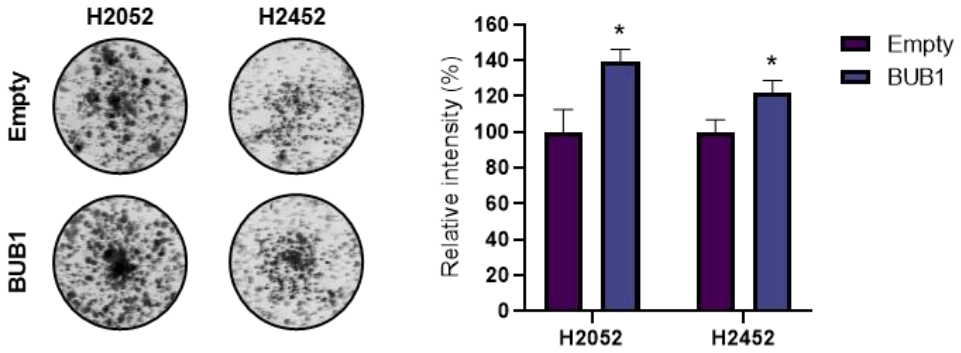


Figure 55. Colony formation assay results of control and BUB1 overexpressing H2052, and H2452 cells. Relative intensity was calculated by proportioning the intensities of overexpression cells to Empty cells. Mean ±SD, n=3, *p<0.05, Student's t-test.

4.20. BUB1 Overexpression Increases 3D Anchorage Independent Growth of MPM Cells

After showing the effects of BUB1 overexpression on 2D cell growth, its effect on 3D colony formation was tested using soft agar colony formation assay. Much like the effects on 2D cell growth, BUB1 overexpression increased 3D colony-forming capacity of MPM cells (Figure 56).

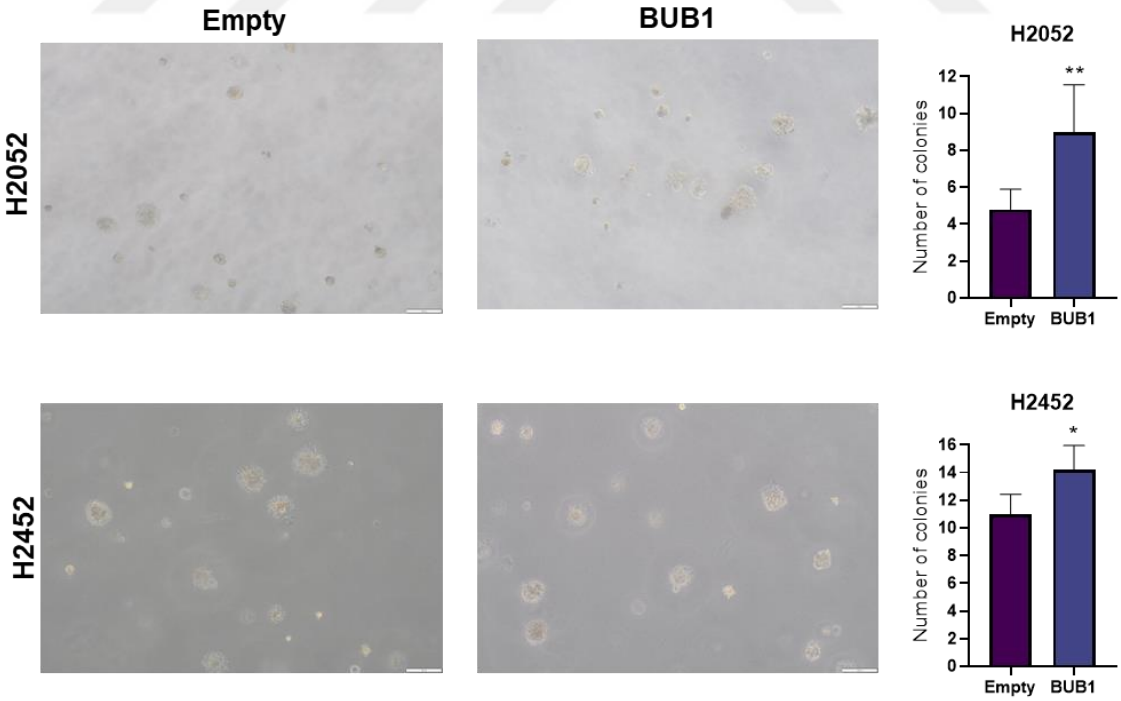


Figure 56. Soft agar images showing the effect of BUB1 overexpression on 3D anchorage independent growth of H2052, and H2452 cells. Colonies with diameter greater than 35 μm

were counted. 10X magnification, scale bar represents 100 µm. Mean ±SD, n=4, *p<0.05, **p<0.01, Student's t-test.

4.21. BUB1 Overexpression Enhances Motility and Migration Capacity of MPM Cells

Next, we compared the aggressive cancer cell behaviors of MPM cells with endogenous and forced BUB1 expression. Cell motility and migration rates of these cells were examined. First, cells were seeded into 6-well plates to be nearly confluent 24 h after seeding. Medium of cells was replaced with fresh medium containing %2 FBS. After 24 h, a wound area was created by using 200 µl pipette tip. Wound areas were measured at T0 and different time points and the % closure was calculated relative to T0. The results showed that BUB1 overexpression increased cell motility of MPM cells (Figure 57).

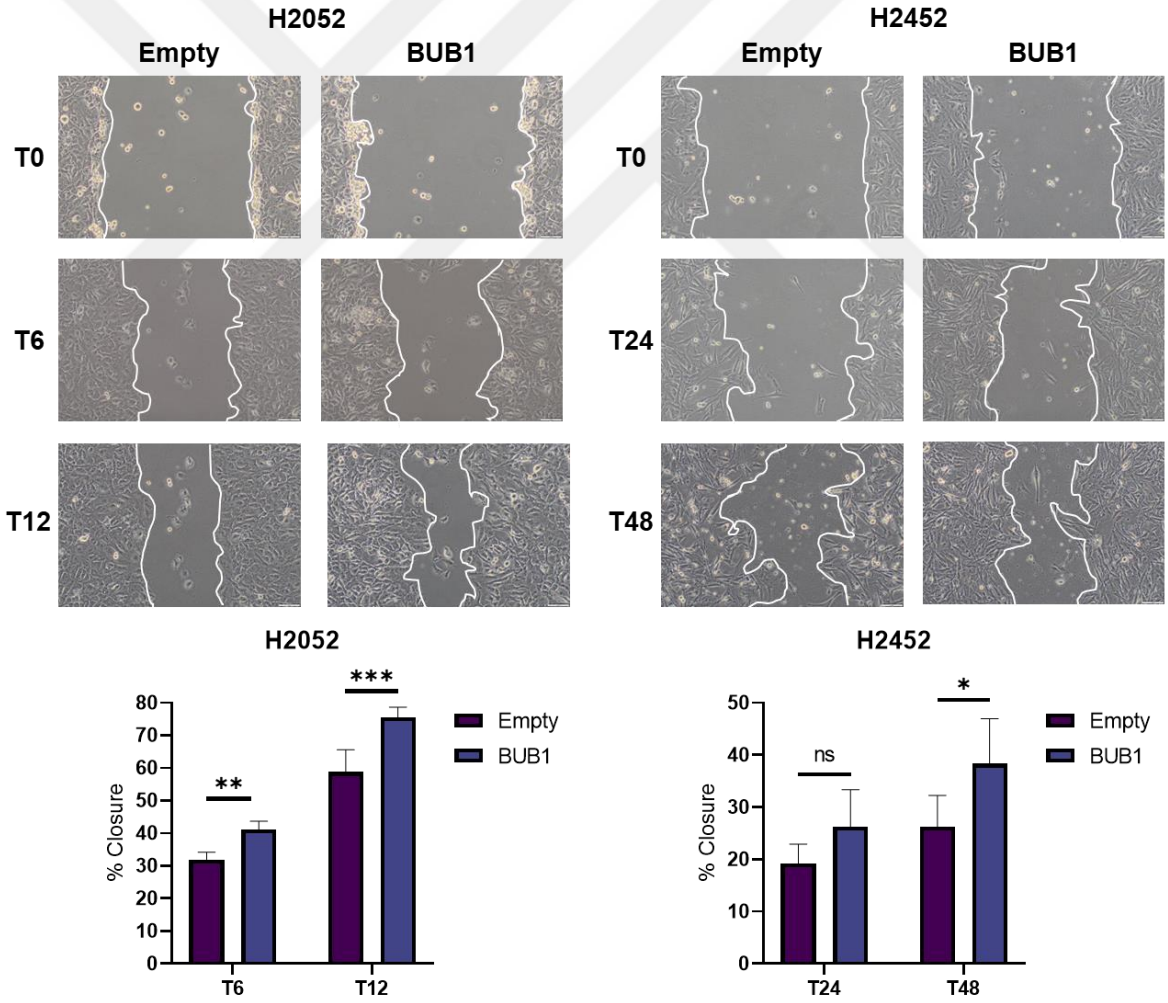


Figure 57. Wound healing assay results of control and BUB1 overexpressing H2052, and H2452 cells. Wound areas were imaged and measured at T0 and different time points and the % closure

was calculated relative to T0. 10X magnification, scale bar represents 100 µm. Mean ±SD, n=6, *p<0.05, **p<0.01, ***p<0.001, ns: not significant, two-way ANOVA multiple comparison.

Similarly, transwell assays revealed that the migration capacity of BUB1 overexpressing cells were increased significantly (Figure 58). Notably, the effect in H2452 cells was rather modest.

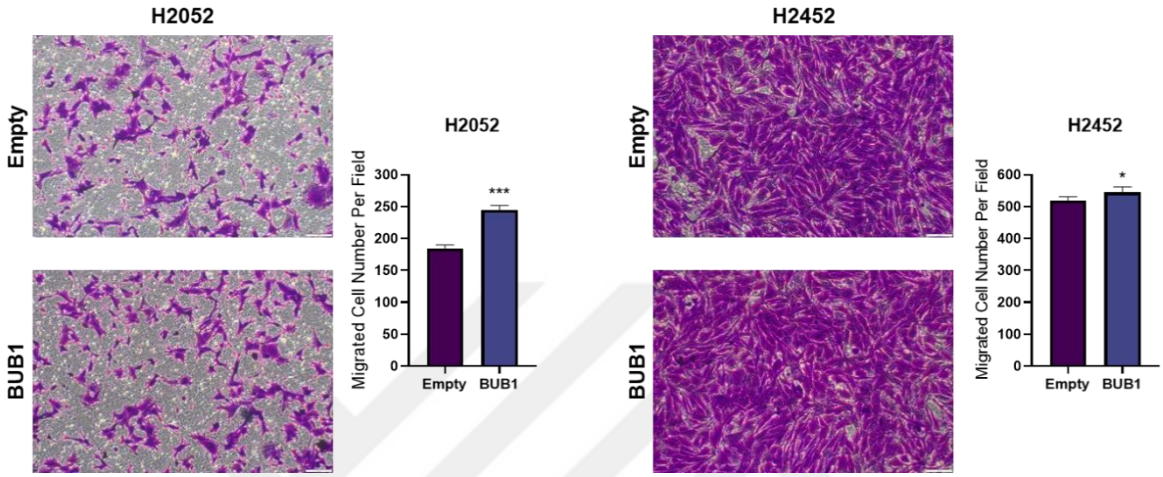


Figure 58. Migration assay results of control and BUB1 overexpressing H2052, and H2452 cells. 10X magnification, scale bar represents 100 µm. Mean ±SD, n=6, *p<0.05, ***p<0.001, Student's t-test.

Since increased migration and invasion rates are indicators of EMT, effect of *BUB1* knockout and overexpression on migration and invasion made us wonder whether BUB1 was associated with EMT. To investigate this, BUB1 mRNA levels were compared with gene sets from three GEO datasets. Results showed that, high BUB1 expression is correlated with EMT (Figure 59).

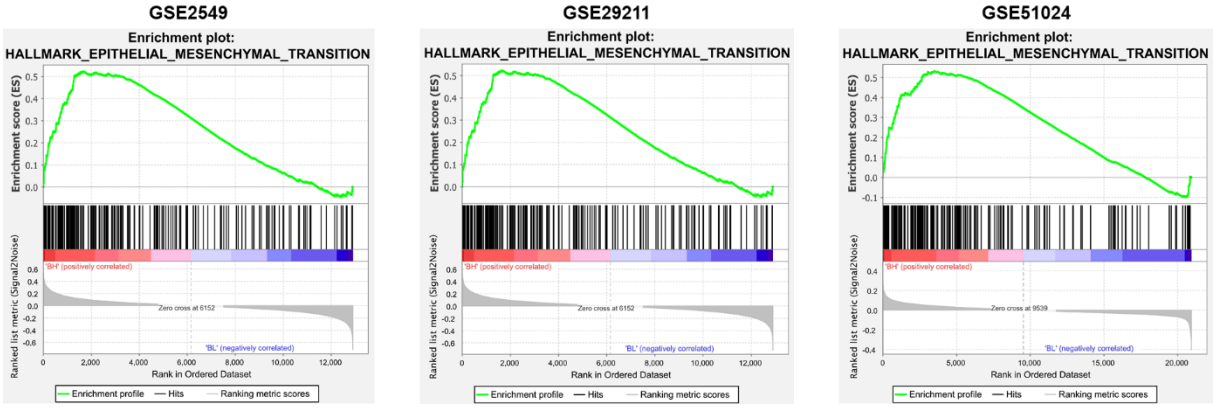


Figure 59. Gene set enrichment analysis of target genes regulating the EMT phenotype in BUB1 low and high MPM samples.

4.22. BAY-1816032 Inhibits Cell Proliferation

Small-molecule inhibitors are commonly used chemical drugs to block kinase functions. To provide preliminary insights into the druggability of BUB1 kinase, here, we employed BAY1816032, a potent inhibitor of BUB1 kinase activity, and evaluated how cell survival and growth are affected *in vitro*. MTT assay was performed first to determine IC50 (Figure 60). Cells were seeded into 96 well plates and treated with different doses of BAY-1816032 for 72 h. IC50 doses for H2052, H2452, and H28 cell lines were calculated as 1.2 µM, 2.8 µM, and 3.9 µM, respectively.

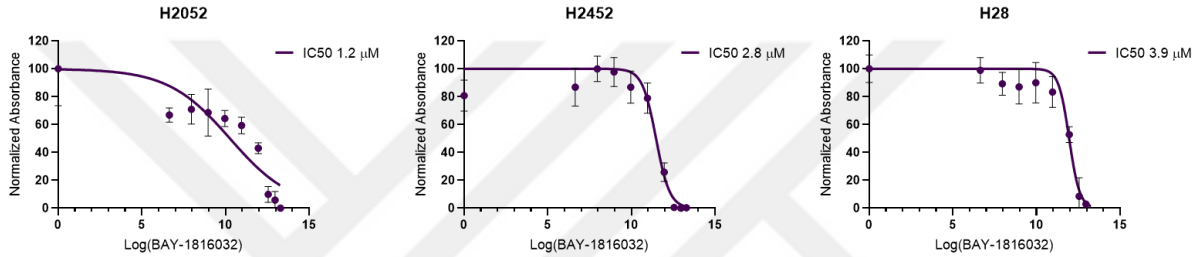


Figure 60. The 50% inhibitory concentrations (IC50) of BAY-1816032 in H2052, H2452, and H28 cell lines.

Then, the effect of BUB1 inhibition on colony-forming capacity of MPM cell lines was examined. Cells were seeded into 6 well plates and treated with IC50 dose and two different doses under IC50 dose for 72 h. Medium was replaced with fresh medium and cells were allowed to form colonies for 10-14 days. The inhibition of BUB1 kinase activity reduced colony formation capacity in a dose dependent manner (Figure 61).

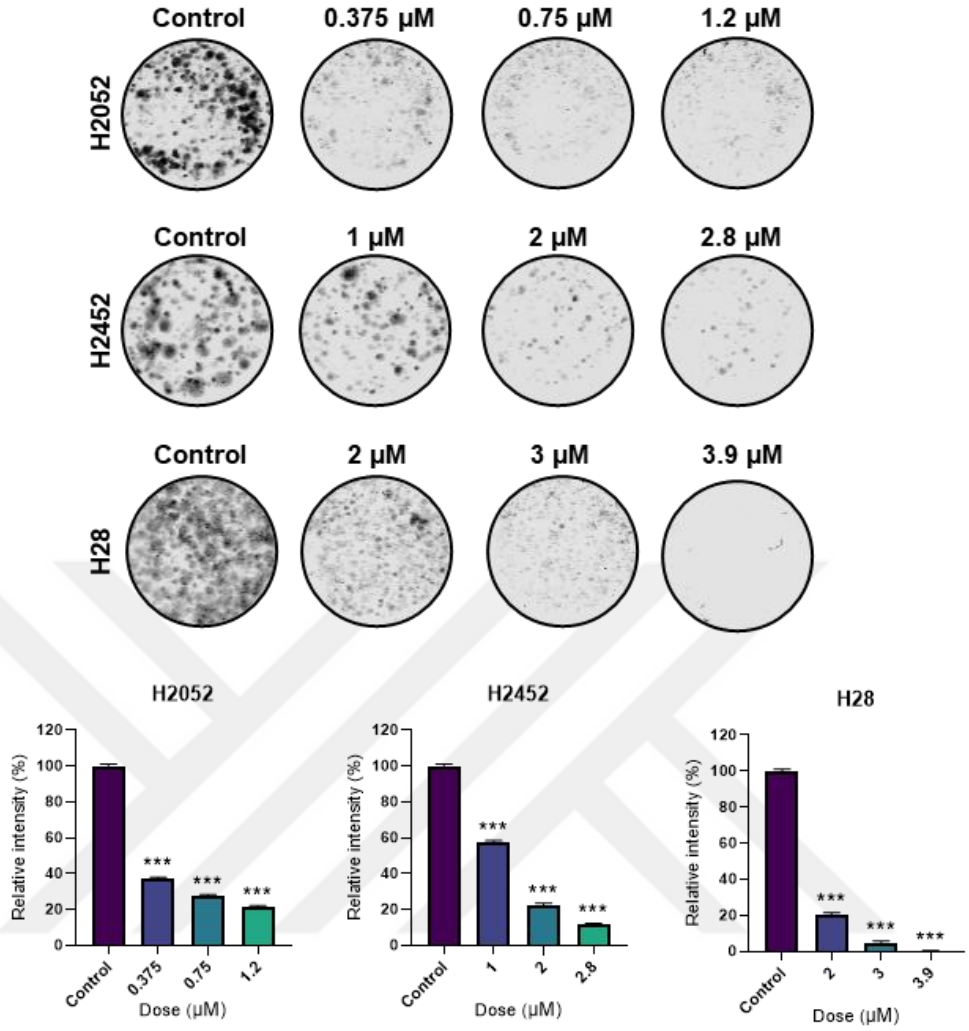


Figure 61. Colony formation assay results of control and BAY-1816032 treated H2052, H2452, and H28 cells. Relative intensity was calculated by proportioning the intensities of treated cells to control cells. Mean ±SD, n=3, ***p<0.001, Student's t-test.

Next, the effect of BAY-1816032 on 3D colony formation was tested using soft agar colony formation assay in H2452 cell line. Significant decrease in 3D anchorage independent colony growth was observed with all doses (Figure 62). These preliminary *in vitro* results suggest that BUB1 kinase activity may dictate its pro-tumorigenic functions, potentially placing this kinase as a druggable target in MPM.

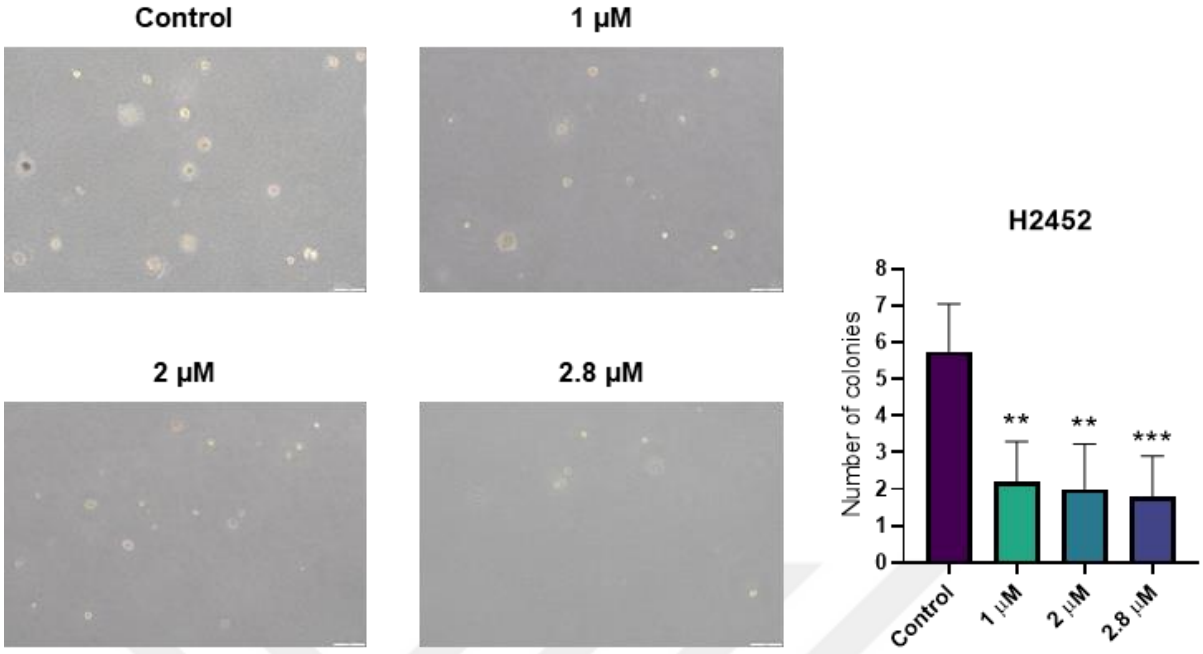
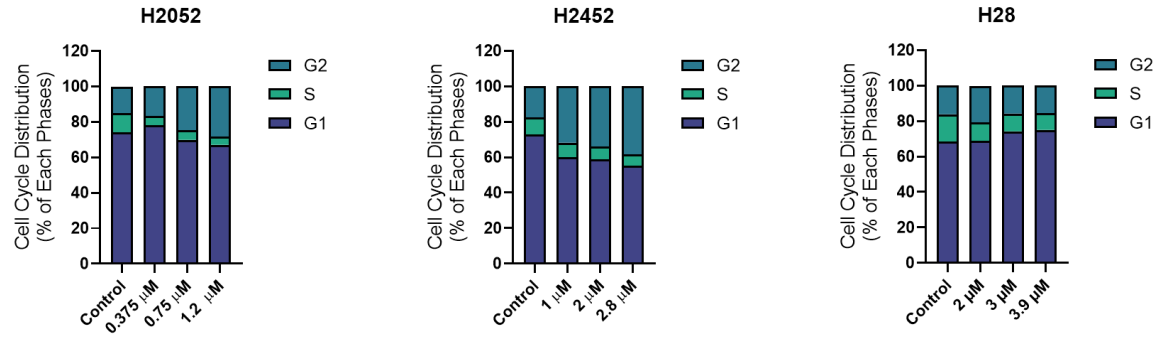


Figure 62. Soft agar images showing the effect of BAY-1816032 on 3D anchorage independent growth of H2452 cells. Colonies with diameter greater than 35 µm were counted. 10X magnification, scale bar represents 100 µm. Mean ±SD, n=4, **p<0.01, ***p<0.001, Student's t-test.

Similar to the knockout experiments, the cell cycle and apoptotic profiles were examined to functionally dissect the cellular mechanisms underlying the effects of BUB1 inhibitor on cell proliferation and growth. As shown in Figure 63, BUB1 inhibition displayed cell cycle arrest in the G2 phase in a dose dependent manner in H2052 an H2452 cells. On the other hand, G1 arrest was observed in H28 cell line.



	Control	0.375 µM	0.75 µM	1.2 µM
G1	74.15	78.1	69.84	67
S	10.6	5.2	5.26	4.6
G2	15.2	16.7	24.9	28.4

	Control	1 µM	2 µM	2.8 µM
G1	72.84	60.04	58.75	55.23
S	9.46	8.16	7.15	6.47
G2	17.7	31.8	34.1	38.3

	Control	2 µM	3 µM	3.9 µM
G1	68.5	68.9	74.2	75
S	15.3	10.5	10	9.4
G2	16.2	20.6	15.8	15.6

Figure 63. Cell cycle distribution of H2052, H2452, and H28 cells treated with BUB1 inhibitor.

Also, in line with the knockout results, inhibitor treatment caused a slight increase in apoptosis (Figure 64).

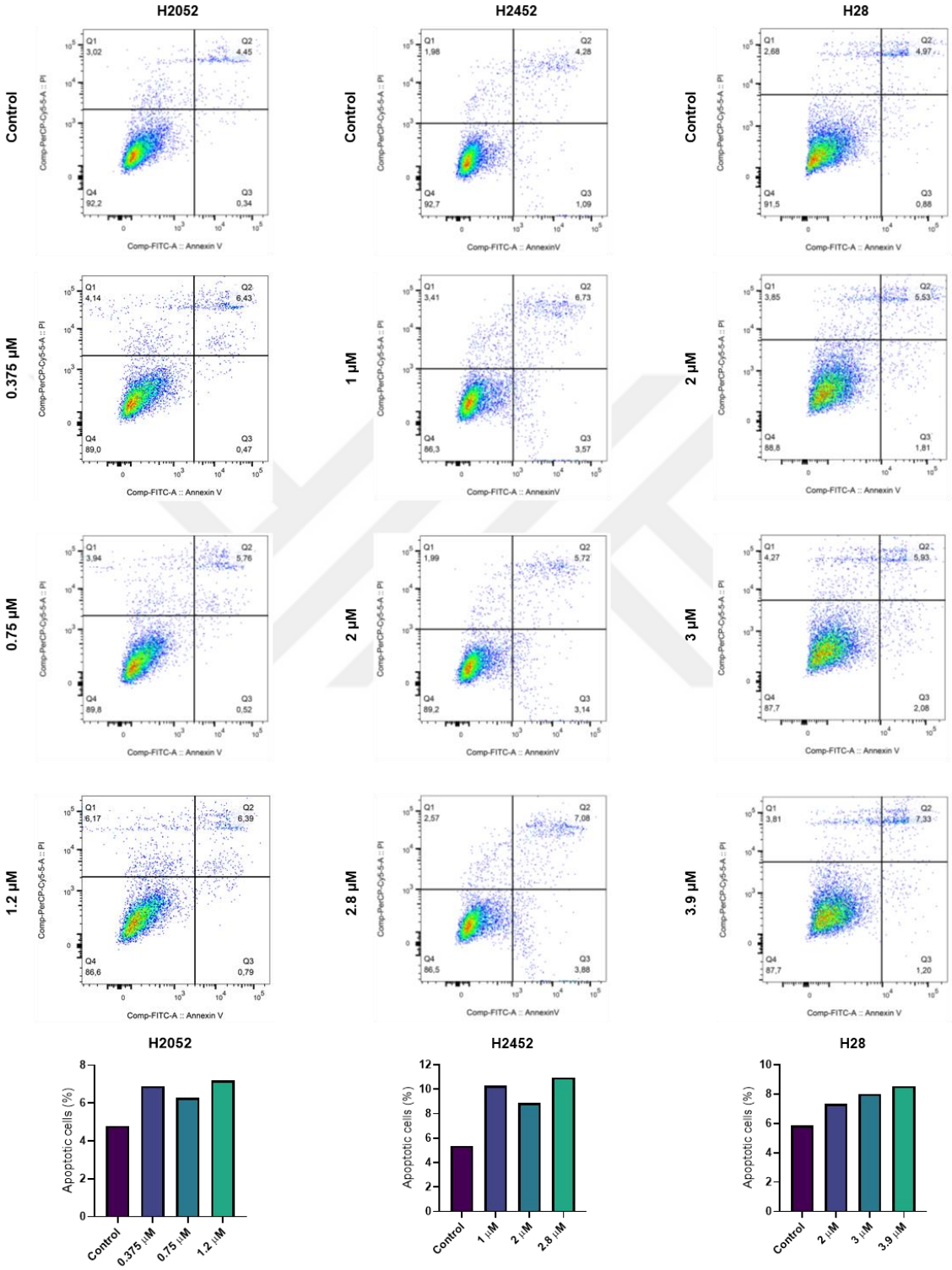


Figure 64. Flow cytometry analysis of apoptosis of control and BUB1 inhibitor treated H2052, H2452, and H28 cells. Percentage of apoptotic cells was calculated as the sum of early (Q3).

5. DISCUSSION

Malignant pleural mesothelioma (MPM) is a type of cancer that arises from the mesothelial cells that line the pleural cavity. MPM is primarily caused by exposure to asbestos. Although rare, MPM is an aggressive cancer that has a poor prognosis. The median survival rate for patients with MPM is approximately one year (12). MPM is a challenging cancer to treat, and currently available treatment modalities have limited efficacy in providing long-term survival (4). While targeted therapies have shown promise in treatment of several other types of cancers, there is no defined target for MPM therapy by clinical guidelines. Therefore, it is necessary to have a deeper understanding of the cellular and molecular mechanisms that underlie the disease as well as the indicators of poor clinical results to identify new targets and develop precise and efficient treatments for MPM. New developments in genomics and functional genomics have offered important understanding into the genetic and molecular features of MPM and the genetic alterations that drive the disease. However, further investigation is still required to fully understand the complex mechanisms behind MPM and develop targeted therapies that can improve patient outcomes.

In this thesis project, we aimed to target the whole genome with the CRISPR/Cas9 screen and to investigate the essential genes and/or gene families that contribute to the survival of MPM cells in high-throughput manner and to validate and characterize the selected gene/genes in the gene-function-phenotype axis. For this purpose, clonal Cas9 expression was successfully achieved in three MPM cell lines and one non-tumorigenic cell line. Different levels of Cas9 expression were observed in various clones and clones with Cas9 function compatible with the highest Cas9 expression for each cell line were selected for further studies. Then, the lentivirus plasmid-based whole genome gRNA library was successfully amplified, and clonal cells were infected with a MOI of ~0.3 and whole genome negative selection screening was started. After infection, T0 samples were collected following puromycin selection, and the remaining cells were divided into three groups and the screening process was continued with three replicates. Although different for each cell line, screening processes were completed to provide at least 250X representation. The 14 doubling times (T14), which is the time determined for the completion of the screening process, varies for each cell line. After the infection, the proliferation of some cell lines slowed down and the T14 times determined before the screening were extended for these cell lines by following the cell numbers.

After deep sequencing following screening, gRNAs producing negative scores according to log2 value were listed. This list includes high-score target genes for all four gRNAs, but these genes also score for the MeT-5A cell line. MeT-5A cell line is an immortalized cell line transformed with the SV40 T antigen and adapted to growth in a two-dimensional cell culture medium. Moreover, it carries various karyotypic changes. For example, according to the study of Ke et al (164), modal chromosome numbers 41-43 were found to be hypodiploid in the MeT5A cell line. In addition, according to the same study, chromosome breaks, acentric and dicentric chromosome structures, minute, and double-minute and random chromosomal rearrangements common in cell lines transformed with SV40 T antigen are also observed in MeT-5A cell lines. These rearrangements are especially found in chromosomes 5, 6, 7 and 13. Therefore, MeT-5A cell line cannot be expected to provide an absolutely accurate model for segregating cancer-specific depletion genes. Consistently, our deep sequencing results confirm this. Therefore, it was not surprising that genes that did not show depletion or alteration in the MeT-5A cell line, although depleted in MPM cell lines, were not obtained. For this reason, as a result of our analyzes, we focused on the genes in which gRNA and gene scores showed depletion in MPM cell lines but showed minimal effect in MeT-5A cell line. Finally, a list of nine genes was obtained (i.e., *ATG9A, BUB1, CCND1, CDK2, NPIPA5, PIKFYVE, TMEM41B, USP17L25*, and *VPS37A*). High expression of five of these genes (*ATG9A, VPS37A, TMEM41B, BUB1* and *CDK2*) was found to be associated with poor survival in MPM.

CCND1 (cyclin D1), a member of D cyclins family, is a regulatory protein that plays a key role in the cell cycle, specifically in the transition from the G1 to the S phase. It forms a complex with CDK4 or CDK6, which then phosphorylates the retinoblastoma protein (Rb), leading to the release of transcription factors and driving cell cycle progression. Overexpression of CCND1 was shown in multiple cancers including non-small cell lung carcinoma, melanoma, and breast cancer (165).

Although there is no publication demonstrating the function of *NPIPA5* (nuclear pore complex interacting protein family member A5), its mutations were shown to be related with poor radiotherapy prognosis in esophageal squamous cell carcinoma (166) and sensitivity to the STING inhibitor H-151 in Diffuse large B-cell lymphoma (167).

PIKFYVE (phosphoinositide kinase, FYVE-type zinc finger containing) encodes an enzyme which exhibits both lipid kinase and protein kinase activity (168) and functions in membrane homeostasis of endosomal system, endocytic-vacuolar pathway, lysosomal trafficking, nuclear

transport, transcriptional regulation, and cell cycle progression (169). PIKfyve inhibitor, YM201636, was shown to suppressed the tumorigenicity of liver cancer (170) and NSCLC cells (171).

There is no literature data on *USP17L25* (Ubiquitin Specific Peptidase 17 Like Family Member 25).

Among the five genes associated with poor survival in MPM, *ATG9A*, *VPS37A* and *TMEM41B* emerge as autophagy-related genes (172). As known, autophagy is a cellular process that degrades and recycles cellular components, including proteins and organelles, by sequestering them into double-membrane vesicles called autophagosomes. The autophagosomes then merge with lysosomes, which contain enzymes that degrade and break down the contents of the autophagosomes for recycling. Autophagy can be activated by various stress signals, such as nutrient deprivation, oxidative stress, and accumulation of damaged organelles or protein aggregates, to help maintain cellular homeostasis. The formation of autophagosomes is initiated by the activation of a complex molecular machinery that involves various autophagy-related (ATG) proteins (173). ATG9A (Autophagy Related 9A) is the only known multispan transmembrane autophagy protein among other ATG proteins. It is present in the trans-Golgi network under basal conditions. After the intiation of autophagy, ATG9A localizes to the cell periphery, co-localizing with phagophore markers and autophagosomes, and supports autophagosome formation (174). Increased ATG9A expression was shown to be associated with increased risk of recurrence and reduced survival rates in patients with oral squamous cell carcinoma (175). Additionally, ATG9A expression was found to be increased in triple negative breast cancer and its *in vitro* silencing inhibited cancer phenotypes (176).

The literature information on *VPS37A* (VPS37A subunit of ESCRT-I) gene, also known as *HCRP1*, is partially limited. As far as is known, this gene supports phagophore closure and completed autophagosome formation by directing the ESCRT (endosomal sorting complex required for transport) mechanism (177). Contrary to the inverse relationship with survival we found in MPM, studies in colon cancer, non-small cell lung cancer and gastric cancer have shown that the expression of this gene is decreased and this situation positively regulates cell proliferation, drug and anoikis resistance (178–180). This highlights the possibility that VPS37A may have a different molecular role in MPM carcinogenesis.

The relationship of the *TMEM41B* (transmembrane protein 41B) gene with the autophagy pathway has only recently been shown. TMEM41B, recently identified as a novel ATG protein,

is a multispan membrane protein localized in the endoplasmic reticulum (ER) and works in conjunction with the VMP1 protein. Specifically, deficiency in TMEM41B blocks the early stage of autophagosome formation, leading to the accumulation of ATG proteins (181). Additionally, TMEM41B deficiency has been shown to trigger abnormal accumulation of intracellular lipid droplets (182). As a result, it functions in cooperation with VMP1 in autophagosome formation and also in maintaining lipid homeostasis. There are no studies on the role of TMEM41B in cancer.

The *CDK2* (cyclin dependent kinase 2) gene encodes a serine-threonine protein kinase which plays a critical role in cell cycle regulation. This protein forms the catalytic subunit of the cyclin-dependent protein kinase complex, which facilitates progression through the cell cycle. The enzymatic activity of CDK2 is particularly important during the G1 to S phase transition. Cyclin A or E is combined with and regulated by other subunits of the complex, including the CDK inhibitor $p21^{Cip1}$ (encoded by the *CDKN1A* gene) and $p27^{Kip1}$ (encoded by the *CDKN1B* gene) (183). CDK2 is also involved in multiple biological processes beyond cell cycle regulation, including DNA repair and transcription, RNA processing and splicing, as well as protein transport and degradation. CDK2 regulation is impaired in many human cancers, and inhibition of CDK2 is known to have antitumor activity in some cancers (184). The molecular role of CDK2 in MPM is not yet known.

As alluded to earlier, BUB1 is a druggable kinase, our CRISPR-Cas9 screen findings are verifiable with the DepMap data, and its role in MPM has not been shown in the literature, making this kinase a unique avenue to be explored in the context of MPM.

BUB1 gene encodes the enzyme-structured serine-threonine kinase protein that functions at the mitotic checkpoint in the cell cycle. This kinase shows peak expression in the G2/M phase of the cell cycle. BUB1 is known to phosphorylate protein members in the mitotic checkpoint complex and activate spindle control and signaling during cell division (122). Thus, it controls the correct alignment of chromosomes during mitosis.

Complete deletion of *BUB1* was shown to cause prenatal lethality in mice (185). BUB1 has either tumor suppressor or oncogenic functions depending on critically changing expression levels (185–187). Both BUB1 hypomorphic (185,186) or overexpressed (187) mice showed increased spontaneous tumorigenesis following chromosomal missegregation and aneuploidy.

BUB1 expression was shown to be increased in patients with pancreatic ductal adenocarcinoma, which is associated with increased tumor size and shorter survival (129). High expression of BUB1 is also associated with poor prognosis in lung adenocarcinoma (188). In addition, BUB1 expression was found to be associated with poor prognosis in breast cancer patients and its *in vitro* inhibition reduced cancer stem cell potential and xenograft formation in breast cancer and pancreatic ductal adenocarcinoma (128,129). Although there is an early publication in the literature suggesting that BUB1 expression may be associated with poor prognosis in MPM (28), there is no study on its molecular role in MPM.

As detailed in the results section, we aimed to characterize molecular role of *BUB1* in MPM. To this end, the *BUB1* gene was silenced by targeting with two gRNAs (i.e. g3 and g5) cloned into the lentiCRISPRv2 vector separately. Then, effects of BUB1 depletion on growth and migration and invasion of MPM cells were investigated. MTT analysis, BrdU assay and colony formation assay showed that BUB1 depletion attenuates growth of MPM cells. Besides, soft agar assay confirmed this effect on 3D anchorage independent growth of MPM cells. In line with these results, cell cycle analysis showed that BUB1 depleted MPM cells displayed arrest in G2 phase, as well as S phase in H2452 cells. This result was supported by the GEO datasets showing correlation of low BUB1 expression with low expression of the transcription factors E2F and MYC, which are important in the G1/S transition. In parallel, limited but significant increase was detected in senescence arrest. Likewise, slight but significant increase in apoptosis was observed in all cell lines except H28 BUB1 g5. Next, we sought to investigate effect of BUB1 depletion on aggressive cancer phenotypes and showed that BUB1 depletion decreases migration and invasion capacity of MPM cells. Finally, to explore the role of BUB1 depletion on tumor growth we employed mouse xenograft model by injecting *BUB1* knockout cells into right flanks of six NU/J mice. Results showed that *BUB1* knockout reduces tumor growth.

In addition to gene silencing, we also examined the effect of BUB1 kinase inhibitor on MPM cells. For this aim, we chose BAY-1816032 because of its tolerable pharmacokinetic properties compared to other BUB1 inhibitors. IC50 dose and two different doses under IC50 dose were used for all set ups. Consistent with gene silencing, BUB1 inhibition reduced 2D as well as 3D anchorage independent colony formation capacity of MPM cells. Besides, H2052 and H2452 cells displayed arrest in G2 phase, while H28 cells displayed arrest in G1 phase upon inhibitor treatment.

After demonstrating the negative effect of BUB1 depletion/inhibition on cell growth and/or aggressive cancer phenotypes, we wondered if BUB1 overexpression augments these phenotypes. For this aim, we generated BUB1 overexpressing H2052 and H2452 cells. We followed a similar experimental flow with *BUB1* knockout studies. Accordingly, we showed that BUB1 over expression increases proliferation index and 2D as well as 3D anchorage independent colony formation capacity of MPM cells. In addition, wound healing and transwell migration assays revealed that BUB1 overexpression enhances motility and migration capacity of MPM cells. This result was supported by the GEO datasets showing correlation of high BUB1 expression with EMT.

High-throughput functional genomics studies such as RNAi and CRISPR screen gave rise to identification of numerous cancer related genes. Since RNAi system doesn't project complete loss-of-function due to hypomorphic phenotypes and has higher off-target effects (189) and CRISPR screens are more efficient in identifying essential genes due to its ability to perturb genes expressed at low levels (190), we employed whole genome CRISPR screen to identify genes that are essential for MPM cell survival. After bioinformatic analyses, the *BUB1* gene emerged as the gene that showed minimal depletion in the MeT-5A cell line, while it showed depletion in all three MPM cell lines. *BUB1* was identified as a common essential gene in the DepMap CRISPR project data and we showed that BUB1 depletion decreases 2D and 3D cell growth, aggressive cancer phenotypes, and *in vivo* tumor engraftment potential in line with the literature data conducted on different cancer lines. Corroborating these results, overexpression of BUB1 increased 2D and 3D cell growth and aggressive cancer phenotypes. Additionally, to evaluate targetability of *BUB1* in MPM with small molecule kinase inhibitor, we treated cells with different doses of BAY-1816032. Although the inhibitor reduced 2D and 3D cell growth, the IC50 values were in the micromolar range. This was consistent with the limited effect of kinase activity of BUB1. Taken together, these results suggested that *BUB1* might be a potential therapeutic target for MPM treatment. However, since BUB1 inhibitors have limited effect on cell proliferation, and BUB1 inhibition, albeit minimal, also has an effect on the MeT-5A cell line, targeted delivery of inhibitor to the tumor site emerge as a need for enhanced efficacy. Besides, further studies should be conducted to elucidate its moleculer role in MPM cells.

6. CONCLUSION AND FUTURE PERSPECTIVES

The aim of this thesis project was to use CRISPR/Cas9 whole genome negative-selection screening method in order to interrogate, identify and functionally characterize essential genes

and/or gene families playing a role in MPM cell survival. In line with this aim, we identified nine genes that might be essential for MPM cell survival. Among these genes, we characterized role of BUB1 in MPM cell growth and/or aggressive cancer phenotypes both by silencing/inhibition or overexpression.

However, a gene family or pathway could not be identified in our study. This is not surprising since MPM is a type of cancer that progresses not by oncogenic changes but rather by cumulative inactivation of tumor suppressor genes.

As one of our future perspectives, in the process of converting this project into an article, we aim to show relationship of BUB1 with EMT, E2F, and MYC by performing qPCR and Western Blot. In addition, to show the specificity of the effect of *BUB1* knock out we are planning to obtain gRNA resistant clones and conduct colony formation assay. Finally, we are planning to develop 3D cell line organoid models to further show the effect of BUB1 depletion on 3D culture and adapted tumor models in mice to overcome the limited growth of cells after injection into the mice.

The molecular role of the *BUB1* gene in MPM, which has been shown to be an essential gene for MPM cell survival in our study and whose increased expression is known to be negatively related to survival in various cancers, is not yet known. Therefore, we proposed a TÜSEB project to further examine the effect of *BUB1* on MPM cells and elucidate the molecular mechanisms underlying this effect. Our goals and objectives in this project are:

- To obtain monoclonal *BUB1* knockout cell lines, if possible, and to further test the effects of BUB1 on cell growth and aggressive cancer phenotypes in these cells.
- To investigate the molecular mechanisms of the above effect of the *BUB1* gene by comparative RNA sequencing and investigating the effect of *BUB1* knockout on cell cycle and DNA replication, SAC process and chromosome alignment, and phosphorylation profiles of known BUB1 protein kinase targets.
- Finally, to evaluate the pharmacological targetability of *BUB1* in MPM with preliminary *in vitro* and *in vivo* experiments.

7. REFERENCES

1. Sung H, Ferlay J, Siegel RL, Laversanne M, Soerjomataram I, Jemal A, et al. Global Cancer Statistics 2020: GLOBOCAN Estimates of Incidence and Mortality Worldwide for 36 Cancers in 185 Countries. CA Cancer J Clin. 2021 May;71(3):209–49.

2. Beebe-Dimmer JL, Fryzek JP, Yee CL, Dalvi TB, Garabrant DH, Schwartz AG, et al. Mesothelioma in the United States: a Surveillance, Epidemiology, and End Results (SEER)-Medicare investigation of treatment patterns and overall survival. Clin Epidemiol. 2016;8:743–50.

3. Baas P, Fennell D, Kerr KM, Van Schil PE, Haas RL, Peters S, et al. Malignant pleural mesothelioma: ESMO Clinical Practice Guidelines for diagnosis, treatment and followup. Ann Oncol. 2015 Sep;26 Suppl 5:v31-39.

4. Cinausero M, Rihawi K, Cortiula F, Follador A, Fasola G, Ardizzoni A. Emerging therapies in malignant pleural mesothelioma. Crit Rev Oncol Hematol. 2019 Dec;144:102815.

5. Cakiroglu E, Senturk S. Genomics and Functional Genomics of Malignant Pleural Mesothelioma. Int J Mol Sci. 2020 Sep 1;21(17):6342.

6. Tsao AS, Wistuba I, Roth JA, Kindler HL. Malignant pleural mesothelioma. J Clin Oncol. 2009 Apr 20;27(12):2081–90.

7. Roushdy-Hammady I, Siegel J, Emri S, Testa JR, Carbone M. Genetic-susceptibility factor and malignant mesothelioma in the Cappadocian region of Turkey. Lancet. 2001 Feb 10;357(9254):444–5.

8. Dogan AU, Baris YI, Dogan M, Emri S, Steele I, Elmishad AG, et al. Genetic predisposition to fiber carcinogenesis causes a mesothelioma epidemic in Turkey. Cancer Res. 2006 May 15;66(10):5063–8.

9. Testa JR, Cheung M, Pei J, Below JE, Tan Y, Sementino E, et al. Germline BAP1 mutations predispose to malignant mesothelioma. Nat Genet. 2011 Aug 28;43(10):1022–5.

10. Carbone M, Adusumilli PS, Alexander HR, Baas P, Bardelli F, Bononi A, et al. Mesothelioma: Scientific clues for prevention, diagnosis, and therapy. CA Cancer J Clin. 2019 Sep;69(5):402–29.

11. Blyth KG, Murphy DJ. Progress and challenges in Mesothelioma: From bench to bedside. Respir Med. 2018 Jan;134:31–41.

12. Ahmadzada T, Reid G, Kao S. Biomarkers in malignant pleural mesothelioma: current status and future directions. J Thorac Dis. 2018 Apr;10(Suppl 9):S1003–7.

13. Scherpereel A, Wallyn F, Albelda SM, Munck C. Novel therapies for malignant pleural mesothelioma. Lancet Oncol. 2018 Mar;19(3):e161–72.

14. Takuwa T, Hasegawa S. Current surgical strategies for malignant pleural mesothelioma. Surg Today. 2016 Aug;46(8):887–94.

15. Nakajima EC, Vellanki PJ, Larkins E, Chatterjee S, Mishra-Kalyani PS, Bi Y, et al. FDA Approval Summary: Nivolumab in Combination with Ipilimumab for the Treatment of

Unresectable Malignant Pleural Mesothelioma. Clin Cancer Res. 2022 Feb 1;28(3):446–51.

16. Bronte G, Incorvaia L, Rizzo S, Passiglia F, Galvano A, Rizzo F, et al. The resistance related to targeted therapy in malignant pleural mesothelioma: Why has not the target been hit yet? Crit Rev Oncol Hematol. 2016 Nov;107:20–32.

17. Nicolini F, Bocchini M, Bronte G, Delmonte A, Guidoboni M, Crinò L, et al. Malignant Pleural Mesothelioma: State-of-the-Art on Current Therapies and Promises for the Future. Front Oncol. 2019;9:1519.

18. Hassan R, Thomas A, Alewine C, Le DT, Jaffee EM, Pastan I. Mesothelin Immunotherapy for Cancer: Ready for Prime Time? J Clin Oncol. 2016 Dec;34(34):4171–9.

19. Khanna S, Thomas A, Abate-Daga D, Zhang J, Morrow B, Steinberg SM, et al. Malignant Mesothelioma Effusions Are Infiltrated by CD3+ T Cells Highly Expressing PD-L1 and the PD-L1+ Tumor Cells within These Effusions Are Susceptible to ADCC by the AntiPD-L1 Antibody Avelumab. J Thorac Oncol. 2016 Nov;11(11):1993–2005.

20. Guazzelli A, Hussain M, Krstic-Demonacos M, Mutti L. Tremelimumab for the treatment of malignant mesothelioma. Expert Opin Biol Ther. 2015;15(12):1819–29.

21. Clinical trials [Internet]. [cited 2023 Jan 20]. Available from: https://clinicaltrials.gov/ct2/results?cond=Malignant+Pleural+Mesothelioma&Search=Apply&recrs=a&recrs=d&age_v=&gndr=&type=&rslt=

22. Tsao AS, Miao J, Wistuba II, Vogelzang NJ, Heymach JV, Fossella FV, et al. Phase II Trial of Cediranib in Combination With Cisplatin and Pemetrexed in ChemotherapyNaïve Patients With Unresectable Malignant Pleural Mesothelioma (SWOG S0905). J Clin Oncol. 2019 Oct 1;37(28):2537–47.

23. Thurneysen C, Opitz I, Kurtz S, Weder W, Stahel RA, Felley-Bosco E. Functional inactivation of NF2/merlin in human mesothelioma. Lung Cancer. 2009 May;64(2):140–7.

24. Illei PB, Rusch VW, Zakowski MF, Ladanyi M. Homozygous deletion of CDKN2A and codeletion of the methylthioadenosine phosphorylase gene in the majority of pleural mesotheliomas. Clin Cancer Res. 2003 Jun;9(6):2108–13.

25. Bott M, Brevet M, Taylor BS, Shimizu S, Ito T, Wang L, et al. The nuclear deubiquitinase BAP1 is commonly inactivated by somatic mutations and 3p21.1 losses in malignant pleural mesothelioma. Nat Genet. 2011 Jun 5;43(7):668–72.

26. de Reyniès A, Jaurand MC, Renier A, Couchy G, Hysi I, Elarouci N, et al. Molecular classification of malignant pleural mesothelioma: identification of a poor prognosis subgroup linked to the epithelial-to-mesenchymal transition. Clin Cancer Res. 2014 Mar 1;20(5):1323–34.

27. Lindholm PM, Salmenkivi K, Vauhkonen H, Nicholson AG, Anttila S, Kinnula VL, et al. Gene copy number analysis in malignant pleural mesothelioma using oligonucleotide array CGH. Cytogenet Genome Res. 2007;119(1–2):46–52.

28. Jean D, Daubriac J, Le Pimpec-Barthes F, Galateau-Salle F, Jaurand MC. Molecular changes in mesothelioma with an impact on prognosis and treatment. Arch Pathol Lab Med. 2012 Mar;136(3):277–93.

29. Sato T, Sekido Y. NF2/Merlin Inactivation and Potential Therapeutic Targets in Mesothelioma. Int J Mol Sci. 2018 Mar 26;19(4):988.

30. Nasu M, Emi M, Pastorino S, Tanji M, Powers A, Luk H, et al. High Incidence of Somatic BAP1 alterations in sporadic malignant mesothelioma. J Thorac Oncol. 2015 Apr;10(4):565–76.

31. Chen P, Wang H, Zhang W, Chen Y, Lv Y, Wu D, et al. Loss of BAP1 Results in Growth Inhibition and Enhances Mesenchymal-Epithelial Transition in Kidney Tumor Cells. Mol Cell Proteomics. 2019 Jul;18(7):1320–9.

32. Affar EB, Carbone M. BAP1 regulates different mechanisms of cell death. Cell Death Dis. 2018 Nov 19;9(12):1151.

33. Bononi A, Yang H, Giorgi C, Patergnani S, Pellegrini L, Su M, et al. Germline BAP1 mutations induce a Warburg effect. Cell Death Differ. 2017 Oct;24(10):1694–704.

34. Zhang Y, Shi J, Liu X, Feng L, Gong Z, Koppula P, et al. BAP1 links metabolic regulation of ferroptosis to tumour suppression. Nat Cell Biol. 2018 Oct;20(10):1181–92.

35. Harbour JW, Onken MD, Roberson EDO, Duan S, Cao L, Worley LA, et al. Frequent mutation of BAP1 in metastasizing uveal melanomas. Science. 2010 Dec 3;330(6009):1410–3.

36. Zhang N, Chen S, Jiang G, Wu Y, Shao J, Liu W, et al. The study on copy number alteration of clear cell renal cancer in Chinese population. J Cancer. 2020;11(1):16–24.

37. Rai K, Pilarski R, Boru G, Rehman M, Saqr AH, Massengill JB, et al. Germline BAP1 alterations in familial uveal melanoma. Genes Chromosomes Cancer. 2017 Feb;56(2):168–74.

38. Njauw CNJ, Kim I, Piris A, Gabree M, Taylor M, Lane AM, et al. Germline BAP1 inactivation is preferentially associated with metastatic ocular melanoma and cutaneousocular melanoma families. PLoS One. 2012;7(4):e35295.

39. Carbone M, Ferris LK, Baumann F, Napolitano A, Lum CA, Flores EG, et al. BAP1 cancer syndrome: malignant mesothelioma, uveal and cutaneous melanoma, and MBAITs. J Transl Med. 2012 Aug 30;10:179.

40. Haugh AM, Njauw CN, Bubley JA, Verzì AE, Zhang B, Kudalkar E, et al. Genotypic and Phenotypic Features of BAP1 Cancer Syndrome: A Report of 8 New Families and Review of Cases in the Literature. JAMA Dermatol. 2017 Oct 1;153(10):999–1006.

41. Sherr CJ. Divorcing ARF and p53: an unsettled case. Nat Rev Cancer. 2006 Sep;6(9):663–73.

42. Knudsen ES, Witkiewicz AK. The Strange Case of CDK4/6 Inhibitors: Mechanisms, Resistance, and Combination Strategies. Trends Cancer. 2017 Jan;3(1):39–55.

43. Sobhani N, Corona SP, Zanconati F, Generali D. Cyclin dependent kinase 4 and 6 inhibitors as novel therapeutic agents for targeted treatment of malignant mesothelioma. Genes Cancer. 2017 Mar;8(3–4):495–6.

44. Bonelli MA, Digiacomo G, Fumarola C, Alfieri R, Quaini F, Falco A, et al. Combined Inhibition of CDK4/6 and PI3K/AKT/mTOR Pathways Induces a Synergistic Anti-Tumor Effect in Malignant Pleural Mesothelioma Cells. Neoplasia. 2017 Aug;19(8):637–48.

45. Facchetti G, Petrella F, Spaggiari L, Rimoldi I. Malignant Pleural Mesothelioma: State of the art and advanced cell therapy. Eur J Med Chem. 2017 Dec 15;142:266–70.

46. Poulikakos PI, Xiao GH, Gallagher R, Jablonski S, Jhanwar SC, Testa JR. Re-expression of the tumor suppressor NF2/merlin inhibits invasiveness in mesothelioma cells and negatively regulates FAK. Oncogene. 2006 Sep 28;25(44):5960–8.

47. Shapiro IM, Kolev VN, Vidal CM, Kadariya Y, Ring JE, Wright Q, et al. Merlin deficiency predicts FAK inhibitor sensitivity: a synthetic lethal relationship. Sci Transl Med. 2014 May 21;6(237):237ra68.

48. Hmeljak J, Sanchez-Vega F, Hoadley KA, Shih J, Stewart C, Heiman D, et al. Integrative Molecular Characterization of Malignant Pleural Mesothelioma. Cancer Discov. 2018 Dec;8(12):1548–65.

49. Tranchant R, Quetel L, Tallet A, Meiller C, Renier A, de Koning L, et al. Co-occurring Mutations of Tumor Suppressor Genes, LATS2 and NF2, in Malignant Pleural Mesothelioma. Clin Cancer Res. 2017 Jun 15;23(12):3191–202.

50. Bueno R, Stawiski EW, Goldstein LD, Durinck S, De Rienzo A, Modrusan Z, et al. Comprehensive genomic analysis of malignant pleural mesothelioma identifies recurrent mutations, gene fusions and splicing alterations. Nat Genet. 2016 Apr;48(4):407–16.

51. Hylebos M, Van Camp G, Vandeweyer G, Fransen E, Beyens M, Cornelissen R, et al. Large-scale copy number analysis reveals variations in genes not previously associated with malignant pleural mesothelioma. Oncotarget. 2017 Dec 26;8(69):113673–86.

52. Park IY, Powell RT, Tripathi DN, Dere R, Ho TH, Blasius TL, et al. Dual Chromatin and Cytoskeletal Remodeling by SETD2. Cell. 2016 Aug 11;166(4):950–62.

53. Shibata T, Sasaki K, Sakamoto Y, Takahashi N. Quantitative chamber angle measurement utilizing image-processing techniques. Ophthalmic Res. 1990;22 Suppl 1:81–4.

54. Tallet A, Nault JC, Renier A, Hysi I, Galateau-Sallé F, Cazes A, et al. Overexpression and promoter mutation of the TERT gene in malignant pleural mesothelioma. Oncogene. 2014 Jul 10;33(28):3748–52.

55. Kato S, Tomson BN, Buys TPH, Elkin SK, Carter JL, Kurzrock R. Genomic Landscape of Malignant Mesotheliomas. Mol Cancer Ther. 2016 Oct;15(10):2498–507.

56. Sneddon S, Patch AM, Dick IM, Kazakoff S, Pearson JV, Waddell N, et al. Whole exome sequencing of an asbestos-induced wild-type murine model of malignant mesothelioma. BMC Cancer. 2017 Jun 2;17(1):396.

57. Tate JG, Bamford S, Jubb HC, Sondka Z, Beare DM, Bindal N, et al. COSMIC: the Catalogue Of Somatic Mutations In Cancer. Nucleic Acids Res. 2019 Jan 8;47(D1):D941–7.

58. ICGC/TCGA Pan-Cancer Analysis of Whole Genomes Consortium. Pan-cancer analysis of whole genomes. Nature. 2020 Feb;578(7793):82–93.

59. Zhang J, Bajari R, Andric D, Gerthoffert F, Lepsa A, Nahal-Bose H, et al. The International Cancer Genome Consortium Data Portal. Nat Biotechnol. 2019 Apr;37(4):367–9.

60. Christou CM, Kyriacou K. BRCA1 and Its Network of Interacting Partners. Biology (Basel). 2013 Jan 2;2(1):40–63.

61. Carbone M, Emri S, Dogan AU, Steele I, Tuncer M, Pass HI, et al. A mesothelioma epidemic in Cappadocia: scientific developments and unexpected social outcomes. Nat Rev Cancer. 2007 Feb;7(2):147–54.

62. Guo G, Chmielecki J, Goparaju C, Heguy A, Dolgalev I, Carbone M, et al. Whole-exome sequencing reveals frequent genetic alterations in BAP1, NF2, CDKN2A, and CUL1 in malignant pleural mesothelioma. Cancer Res. 2015 Jan 15;75(2):264–9.

63. Lo Iacono M, Monica V, Righi L, Grosso F, Libener R, Vatrano S, et al. Targeted nextgeneration sequencing of cancer genes in advanced stage malignant pleural mesothelioma: a retrospective study. J Thorac Oncol. 2015 Mar;10(3):492–9.

64. Borczuk AC, Pei J, Taub RN, Levy B, Nahum O, Chen J, et al. Genome-wide analysis of abdominal and pleural malignant mesothelioma with DNA arrays reveals both common and distinct regions of copy number alteration. Cancer Biol Ther. 2016;17(3):328–35.

65. Quetel L, Meiller C, Assié JB, Blum Y, Imbeaud S, Montagne F, et al. Genetic alterations of malignant pleural mesothelioma: association with tumor heterogeneity and overall survival. Mol Oncol. 2020 Jun;14(6):1207–23.

66. Mäki-Nevala S, Sarhadi VK, Knuuttila A, Scheinin I, Ellonen P, Lagström S, et al. Driver Gene and Novel Mutations in Asbestos-Exposed Lung Adenocarcinoma and Malignant Mesothelioma Detected by Exome Sequencing. Lung. 2016 Feb;194(1):125–35.

67. Imielinski M, Berger AH, Hammerman PS, Hernandez B, Pugh TJ, Hodis E, et al. Mapping the hallmarks of lung adenocarcinoma with massively parallel sequencing. Cell. 2012 Sep 14;150(6):1107–20.

68. Ugurluer G, Chang K, Gamez ME, Arnett AL, Jayakrishnan R, Miller RC, et al. Genomebased Mutational Analysis by Next Generation Sequencing in Patients with Malignant Pleural and Peritoneal Mesothelioma. Anticancer Res. 2016 May;36(5):2331–8.

69. Ding L, Getz G, Wheeler DA, Mardis ER, McLellan MD, Cibulskis K, et al. Somatic mutations affect key pathways in lung adenocarcinoma. Nature. 2008 Oct 23;455(7216):1069–75.

70. Huang D, Sun W, Zhou Y, Li P, Chen F, Chen H, et al. Mutations of key driver genes in colorectal cancer progression and metastasis. Cancer Metastasis Rev. 2018 Mar;37(1):173–87.

71. Zimmer K, Puccini A, Xiu J, Baca Y, Spizzo G, Lenz HJ, et al. WRN-Mutated Colorectal Cancer Is Characterized by a Distinct Genetic Phenotype. Cancers (Basel). 2020 May 22;12(5):1319.

72. Mathot L, Kundu S, Ljungström V, Svedlund J, Moens L, Adlerteg T, et al. Somatic Ephrin Receptor Mutations Are Associated with Metastasis in Primary Colorectal Cancer. Cancer Res. 2017 Apr 1;77(7):1730–40.

73. Kim JE, Kim KK, Kim SY, Lee J, Park SH, Park JO, et al. MAP2K1 Mutation in Colorectal Cancer Patients: Therapeutic Challenge Using Patient-Derived Tumor Cell Lines. J Cancer. 2017;8(12):2263–8.

74. Shiovitz S, Korde LA. Genetics of breast cancer: a topic in evolution. Ann Oncol. 2015 Jul;26(7):1291–9.

75. Zhou S, Liu L, Li H, Eilers G, Kuang Y, Shi S, et al. Multipoint targeting of the PI3K/mTOR pathway in mesothelioma. Br J Cancer. 2014 May 13;110(10):2479–88.

76. El-Hosainy A, Hosny H, Gabal S, Ahmed S, El-Hinnawy Y. Role of epidermal growth factor receptor in malignant pleural mesothelioma and its value for successful chemical pleurodesis. Egyptian Journal of Chest Diseases and Tuberculosis. 2014 Oct;63(4):873–81.

77. Suzuki Y, Murakami H, Kawaguchi K, Tanigushi T, Fujii M, Shinjo K, et al. Activation of the PI3K-AKT pathway in human malignant mesothelioma cells. Mol Med Rep. 2009;2(2):181–8.

78. Cedrés S, Montero MA, Martinez P, Martinez A, Rodríguez-Freixinós V, Torrejon D, et al. Exploratory analysis of activation of PTEN-PI3K pathway and downstream proteins in malignant pleural mesothelioma (MPM). Lung Cancer. 2012 Jul;77(1):192–8.

79. Agarwal V, Campbell A, Beaumont KL, Cawkwell L, Lind MJ. PTEN protein expression in malignant pleural mesothelioma. Tumour Biol. 2013 Apr;34(2):847–51.

80. Ou WB, Hubert C, Corson JM, Bueno R, Flynn DL, Sugarbaker DJ, et al. Targeted inhibition of multiple receptor tyrosine kinases in mesothelioma. Neoplasia. 2011 Jan;13(1):12–22.

81. Vintman L, Nielsen S, Berner A, Reich R, Davidson B. Mitogen-activated protein kinase expression and activation does not differentiate benign from malignant mesothelial cells. Cancer. 2005 Jun 1;103(11):2427–33.

82. Dazzi H, Hasleton PS, Thatcher N, Wilkes S, Swindell R, Chatterjee AK. Malignant pleural mesothelioma and epidermal growth factor receptor (EGF-R). Relationship of EGF-R with histology and survival using fixed paraffin embedded tissue and the F4, monoclonal antibody. Br J Cancer. 1990 Jun;61(6):924–6.

83. Mezzapelle R, Miglio U, Rena O, Paganotti A, Allegrini S, Antona J, et al. Mutation analysis of the EGFR gene and downstream signalling pathway in histologic samples of malignant pleural mesothelioma. Br J Cancer. 2013 Apr 30;108(8):1743–9.

84. Pasello G, Favaretto A. Molecular targets in malignant pleural mesothelioma treatment. Curr Drug Targets. 2009 Dec;10(12):1235–44.

85. Govindan R, Kratzke RA, Herndon JE, Niehans GA, Vollmer R, Watson D, et al. Gefitinib in patients with malignant mesothelioma: a phase II study by the Cancer and Leukemia Group B. Clin Cancer Res. 2005 Mar 15;11(6):2300–4.

86. Garland LL, Rankin C, Gandara DR, Rivkin SE, Scott KM, Nagle RB, et al. Phase II study of erlotinib in patients with malignant pleural mesothelioma: a Southwest Oncology Group Study. J Clin Oncol. 2007 Jun 10;25(17):2406–13.

87. Hanahan D, Weinberg RA. Hallmarks of cancer: the next generation. Cell. 2011 Mar 4;144(5):646–74.

88. Edwards JG, Cox G, Andi A, Jones JL, Walker RA, Waller DA, et al. Angiogenesis is an independent prognostic factor in malignant mesothelioma. Br J Cancer. 2001 Sep 14;85(6):863–8.

89. Zalcman G, Mazieres J, Margery J, Greillier L, Audigier-Valette C, Moro-Sibilot D, et al. Bevacizumab for newly diagnosed pleural mesothelioma in the Mesothelioma Avastin Cisplatin Pemetrexed Study (MAPS): a randomised, controlled, open-label, phase 3 trial. Lancet. 2016 Apr 2;387(10026):1405–14.

90. Loganathan S, Kanteti R, Siddiqui SS, El-Hashani E, Tretiakova M, Vigneswaran H, et al. Role of protein kinase C β and vascular endothelial growth factor receptor in malignant pleural mesothelioma: Therapeutic implications and the usefulness of Caenorhabditis elegans model organism. J Carcinog. 2011 Mar 3;10:4.

91. Albonici L, Palumbo C, Manzari V. Role of Inflammation and Angiogenic Growth Factors in Malignant Mesothelioma. In: Belli C, editor. Malignant Mesothelioma [Internet]. InTech; 2012 [cited 2023 Jan 20]. Available from: http://www.intechopen.com/books/malignant-mesothelioma/role-of-inflammation-andangiogenic-growth-factors-in-malignant-mesothelioma

92. Saunders WS, Hoyt MA. Kinesin-related proteins required for structural integrity of the mitotic spindle. Cell. 1992 Aug 7;70(3):451–8.

93. Musacchio A. The Molecular Biology of Spindle Assembly Checkpoint Signaling Dynamics. Curr Biol. 2015 Oct 19;25(20):R1002-1018.

94. Lamothe R, Costantino L, Koshland DE. The spatial regulation of condensin activity in chromosome condensation. Genes Dev. 2020 Jun 1;34(11–12):819–31.

95. Clute P, Pines J. Temporal and spatial control of cyclin B1 destruction in metaphase. Nat Cell Biol. 1999 Jun;1(2):82–7.

96. Crispi S, Calogero RA, Santini M, Mellone P, Vincenzi B, Citro G, et al. Global gene expression profiling of human pleural mesotheliomas: identification of matrix metalloproteinase 14 (MMP-14) as potential tumour target. PLoS One. 2009 Sep 15;4(9):e7016.

97. Suraokar MB, Nunez MI, Diao L, Chow CW, Kim D, Behrens C, et al. Expression profiling stratifies mesothelioma tumors and signifies deregulation of spindle checkpoint pathway and microtubule network with therapeutic implications. Ann Oncol. 2014 Jun;25(6):1184–92.

98. Ou WB, Corson JM, Flynn DL, Lu WP, Wise SC, Bueno R, et al. AXL regulates mesothelioma proliferation and invasiveness. Oncogene. 2011 Apr 7;30(14):1643–52.

99. Goparaju C, Donington JS, Hsu T, Harrington R, Hirsch N, Pass HI. Overexpression of EPH receptor B2 in malignant mesothelioma correlates with oncogenic behavior. J Thorac Oncol. 2013 Sep;8(9):1203–11.

100. Wang J, Mirzapoiazova T, Carol Tan YH, Pang KM, Pozhitkov A, Wang Y, et al. Inhibiting crosstalk between MET signaling and mitochondrial dynamics and morphology: a novel therapeutic approach for lung cancer and mesothelioma. Cancer Biol Ther. 2018;19(11):1023–32.

101. Hoda MA, Münzker J, Ghanim B, Schelch K, Klikovits T, Laszlo V, et al. Suppression of activin A signals inhibits growth of malignant pleural mesothelioma cells. Br J Cancer. 2012 Dec 4;107(12):1978–86.

102. Horio M, Sato M, Takeyama Y, Elshazley M, Yamashita R, Hase T, et al. Transient but not stable ZEB1 knockdown dramatically inhibits growth of malignant pleural mesothelioma cells. Ann Surg Oncol. 2012 Jul;19 Suppl 3(Suppl 3):S634-645.

103. Pinton G, Thomas W, Bellini P, Manente AG, Favoni RE, Harvey BJ, et al. Estrogen receptor β exerts tumor repressive functions in human malignant pleural mesothelioma via EGFR inactivation and affects response to gefitinib. PLoS One. 2010 Nov 29;5(11):e14110.

104. Rao M, Atay SM, Shukla V, Hong Y, Upham T, Ripley RT, et al. Mithramycin Depletes Specificity Protein 1 and Activates p53 to Mediate Senescence and Apoptosis of Malignant Pleural Mesothelioma Cells. Clin Cancer Res. 2016 Mar 1;22(5):1197–210.

105. Plönes T, Fischer M, Höhne K, Sato H, Müller-Quernheim J, Zissel G. Turning back the Wheel: Inducing Mesenchymal to Epithelial Transition via Wilms Tumor 1 Knockdown in Human Mesothelioma Cell Lines to Influence Proliferation, Invasiveness, and Chemotaxis. Pathol Oncol Res. 2017 Oct;23(4):723–30.

106. He X, Wang L, Riedel H, Wang K, Yang Y, Dinu CZ, et al. Mesothelin promotes epithelial-to-mesenchymal transition and tumorigenicity of human lung cancer and mesothelioma cells. Mol Cancer. 2017 Mar 14;16(1):63.

107. Zhang WQ, Dai YY, Hsu PC, Wang H, Cheng L, Yang YL, et al. Targeting YAP in malignant pleural mesothelioma. J Cell Mol Med. 2017 Nov;21(11):2663–76.

108. Calvet L, Dos-Santos O, Spanakis E, Jean-Baptiste V, Le Bail JC, Buzy A, et al. YAP1 is essential for malignant mesothelioma tumor maintenance. BMC Cancer. 2022 Jun 10;22(1):639.

109. Huang J, Tabata S, Kakiuchi S, The Van T, Goto H, Hanibuchi M, et al. Identification of pregnancy-associated plasma protein A as a migration-promoting gene in malignant pleural mesothelioma cells: a potential therapeutic target. Oncotarget. 2013 Aug;4(8):1172–84.

110. Hariharan A, Qi W, Rehrauer H, Wu L, Ronner M, Wipplinger M, et al. Heterogeneous RNA editing and influence of ADAR2 on mesothelioma chemoresistance and the tumor microenvironment. Mol Oncol. 2022 Dec;16(22):3949–74.

111. Suzuki K, Tange M, Yamagishi R, Hanada H, Mukai S, Sato T, et al. SMG6 regulates DNA damage and cell survival in Hippo pathway kinase LATS2-inactivated malignant mesothelioma. Cell Death Discov. 2022 Nov 5;8(1):446.

112. Pandey SK, Machlof-Cohen R, Santhanam M, Shteinfer-Kuzmine A, Shoshan-Barmatz V. Silencing VDAC1 to Treat Mesothelioma Cancer: Tumor Reprograming and Altering Tumor Hallmarks. Biomolecules. 2022 Jun 27;12(7):895.

113. Kambara T, Amatya VJ, Kushitani K, Fujii Y, Endo I, Takeshima Y. Downregulation of FTL decreases proliferation of malignant mesothelioma cells by inducing G1 cell cycle arrest. Oncol Lett. 2022 Jun;23(6):174.

114. Endo I, Amatya VJ, Kushitani K, Kambara T, Nakagiri T, Fujii Y, et al. Insulin-Like Growth Factor 2 mRNA Binding Protein 3 Promotes Cell Proliferation of Malignant Mesothelioma Cells by Downregulating p27Kip1. Front Oncol. 2021;11:795467.

115. Sato T, Mukai S, Ikeda H, Mishiro-Sato E, Akao K, Kobayashi T, et al. Silencing of SmgGDS, a Novel mTORC1 Inducer That Binds to RHEBs, Inhibits Malignant Mesothelioma Cell Proliferation. Mol Cancer Res. 2021 May;19(5):921–31.

116. Sudo H, Tsuji AB, Sugyo A, Kohda M, Sogawa C, Yoshida C, et al. Knockdown of COPA, identified by loss-of-function screen, induces apoptosis and suppresses tumor growth in mesothelioma mouse model. Genomics. 2010 Apr;95(4):210–6.

117. Linton A, Cheng YY, Griggs K, Schedlich L, Kirschner MB, Gattani S, et al. An RNAibased screen reveals PLK1, CDK1 and NDC80 as potential therapeutic targets in malignant pleural mesothelioma. Br J Cancer. 2014 Jan 21;110(2):510–9.

118. Okonska A, Bühler S, Rao V, Ronner M, Blijlevens M, van der Meulen-Muileman IH, et al. Functional Genomic Screen in Mesothelioma Reveals that Loss of Function of BRCA1-Associated Protein 1 Induces Chemoresistance to Ribonucleotide Reductase Inhibition. Mol Cancer Ther. 2020 Feb;19(2):552–63.

119. Dell'Anno I, Barbarino M, Barone E, Giordano A, Luzzi L, Bottaro M, et al. EIF4G1 and RAN as Possible Drivers for Malignant Pleural Mesothelioma. Int J Mol Sci. 2020 Jul 9;21(14):4856.

120. Xu D, Liang SQ, Yang H, Bruggmann R, Berezowska S, Yang Z, et al. CRISPR Screening Identifies WEE1 as a Combination Target for Standard Chemotherapy in Malignant Pleural Mesothelioma. Mol Cancer Ther. 2020 Feb;19(2):661–72.

121. Lorenzini E, Torricelli F, Zamponi R, Donati B, Manicardi V, Sauta E, et al. KAP1 is a new non-genetic vulnerability of malignant pleural mesothelioma (MPM). NAR Cancer. 2022 Sep;4(3):zcac024.

122. Kim T, Gartner A. Bub1 kinase in the regulation of mitosis. Anim Cells Syst (Seoul). 2021 Feb 17;25(1):1–10.

123. Bolanos-Garcia VM, Blundell TL. BUB1 and BUBR1: multifaceted kinases of the cell cycle. Trends Biochem Sci. 2011 Mar;36(3):141–50.

124. Yu H, Tang Z. Bub1 multitasking in mitosis. Cell Cycle. 2005 Feb;4(2):262–5.

125. Siemeister G, Mengel A, Fernández-Montalván AE, Bone W, Schröder J, Zitzmann-Kolbe S, et al. Inhibition of BUB1 Kinase by BAY 1816032 Sensitizes Tumor Cells toward Taxanes, ATR, and PARP Inhibitors In Vitro and In Vivo. Clin Cancer Res. 2019 Feb 15;25(4):1404–14.

126. Yang C, Wang H, Xu Y, Brinkman KL, Ishiyama H, Wong STC, et al. The kinetochore protein Bub1 participates in the DNA damage response. DNA Repair (Amst). 2012 Feb 1;11(2):185–91.

127. Zhu LJ, Pan Y, Chen XY, Hou PF. BUB1 promotes proliferation of liver cancer cells by activating SMAD2 phosphorylation. Oncol Lett. 2020 May;19(5):3506–12.

128. Han JY, Han YK, Park GY, Kim SD, Lee CG. Bub1 is required for maintaining cancer stem cells in breast cancer cell lines. Sci Rep. 2015 Nov 2;5:15993.

129. Piao J, Zhu L, Sun J, Li N, Dong B, Yang Y, et al. High expression of CDK1 and BUB1 predicts poor prognosis of pancreatic ductal adenocarcinoma. Gene. 2019 Jun 15;701:15–22.

130. Huang Z, Wang S, Wei H, Chen H, Shen R, Lin R, et al. Inhibition of BUB1 suppresses tumorigenesis of osteosarcoma via blocking of PI3K/Akt and ERK pathways. J Cell Mol Med. 2021 Sep;25(17):8442–53.

131. Baron AP, von Schubert C, Cubizolles F, Siemeister G, Hitchcock M, Mengel A, et al. Probing the catalytic functions of Bub1 kinase using the small molecule inhibitors BAY320 and BAY-524. Elife. 2016 Feb 17;5:e12187.

132. Kang J, Yang M, Li B, Qi W, Zhang C, Shokat KM, et al. Structure and substrate recruitment of the human spindle checkpoint kinase Bub1. Mol Cell. 2008 Nov 7;32(3):394–405.

133. Jiang N, Liao Y, Wang M, Wang Y, Wang K, Guo J, et al. BUB1 drives the occurrence and development of bladder cancer by mediating the STAT3 signaling pathway. J Exp Clin Cancer Res. 2021 Dec 1;40(1):378.

134. Korkmaz T, Aygenli F, Emisoglu H, Ozcelik G, Canturk A, Yilmaz S, et al. Opposite Carcinogenic Effects of Circadian Clock Gene BMAL1. Sci Rep. 2018 Oct 30;8(1):16023.

135. Senturk S, Shirole NH, Nowak DG, Corbo V, Pal D, Vaughan A, et al. Rapid and tunable method to temporally control gene editing based on conditional Cas9 stabilization. Nat Commun. 2017 Feb 22;8:14370.

136. Sa'id Ameen Z, Cakiroglu E, Senturk S, Ibrahhim AU, Ozsoz M. CRISPR/Cas9 Gene Editing in Mammalian Cells Using LentiCRISPRv2/LentiGuide-Puro Vectors. In: Islam MT, Molla KA, editors. CRISPR-Cas Methods [Internet]. New York, NY: Springer US; 2021 [cited 2023 Feb 21]. p. 281–99. (Springer Protocols Handbooks). Available from: https://link.springer.com/10.1007/978-1-0716-1657-4_18

137. Doench JG, Fusi N, Sullender M, Hegde M, Vaimberg EW, Donovan KF, et al. Optimized sgRNA design to maximize activity and minimize off-target effects of CRISPR-Cas9. Nat Biotechnol. 2016 Feb;34(2):184–91.

138. addgene [Internet]. [cited 2023 Jan 20]. Available from: https://www.addgene.org/browse/article/16517/).

139. Hispeed plasmid maxi kit.

140. Joung J, Konermann S, Gootenberg JS, Abudayyeh OO, Platt RJ, Brigham MD, et al. Genome-scale CRISPR-Cas9 knockout and transcriptional activation screening. Nat Protoc. 2017 Apr;12(4):828–63.

141. Wang B, Wang M, Zhang W, Xiao T, Chen CH, Wu A, et al. Integrative analysis of pooled CRISPR genetic screens using MAGeCKFlute. Nat Protoc. 2019 Mar;14(3):756–80.

142. Nowak DG, Katsenelson KC, Watrud KE, Chen M, Mathew G, D'Andrea VD, et al. The PHLPP2 phosphatase is a druggable driver of prostate cancer progression. J Cell Biol. 2019 Jun 3;218(6):1943–57.

143. Bigenzahn JW, Collu GM, Kartnig F, Pieraks M, Vladimer GI, Heinz LX, et al. LZTR1 is a regulator of RAS ubiquitination and signaling. Science. 2018 Dec 7;362(6419):1171–7.

144. Ran FA, Hsu PD, Wright J, Agarwala V, Scott DA, Zhang F. Genome engineering using the CRISPR-Cas9 system. Nat Protoc. 2013 Nov;8(11):2281–308.

145. WB abcam.

146. geo [Internet]. [cited 2023 Jan 20]. Available from: https://www.ncbi.nlm.nih.gov/geo/

147. Zhang B, Metharom P, Jullie H, Ellem KA, Cleghorn G, West MJ, et al. The significance of controlled conditions in lentiviral vector titration and in the use of multiplicity of infection (MOI) for predicting gene transfer events. Genet Vaccines Ther. 2004 Aug 4;2(1):6.

148. Abrahams MR, Anderson JA, Giorgi EE, Seoighe C, Mlisana K, Ping LH, et al. Quantitating the multiplicity of infection with human immunodeficiency virus type 1 subtype C reveals a non-poisson distribution of transmitted variants. J Virol. 2009 Apr;83(8):3556–67.

149. Hart T, Brown KR, Sircoulomb F, Rottapel R, Moffat J. Measuring error rates in genomic perturbation screens: gold standards for human functional genomics. Mol Syst Biol. 2014 Jul 1;10(7):733.

150. Sun H, Wang Y, Jing HY, Yang XY, Shi XX, Zhang JH, et al. Chaperonin-Containing TCP1 Subunit 6A Is a Prognostic Potential Biomarker That Correlates With the Presence of Immune Infiltrates in Colorectal Cancer. Front Genet. 2021;12:629856.

151. Kodama M, Kodama T, Newberg JY, Katayama H, Kobayashi M, Hanash SM, et al. In vivo loss-of-function screens identify KPNB1 as a new druggable oncogene in epithelial ovarian cancer. Proc Natl Acad Sci U S A. 2017 Aug 29;114(35):E7301–10.

152. Chang YW, Chen HA, Tseng CF, Hong CC, Ma JT, Hung MC, et al. De-acetylation and degradation of HSPA5 is critical for E1A metastasis suppression in breast cancer cells. Oncotarget. 2014 Nov 15;5(21):10558–70.

153. Li L, Kong XA, Zang M, Dong J, Feng Y, Gui B, et al. Hsa_circ_0003732 promotes osteosarcoma cells proliferation via miR-545/CCNA2 axis. Biosci Rep. 2020 Jun 26;40(6):BSR20191552.

154. Xu JH, Hu SL, Shen GD, Shen G. Tumor suppressor genes and their underlying interactions in paclitaxel resistance in cancer therapy. Cancer Cell Int. 2016;16:13.

155. Tordjman J, Majumder M, Amiri M, Hasan A, Hess D, Lala PK. Tumor suppressor role of cytoplasmic polyadenylation element binding protein 2 (CPEB2) in human mammary epithelial cells. BMC Cancer. 2019 Jun 11;19(1):561.

156. Wang T, Birsoy K, Hughes NW, Krupczak KM, Post Y, Wei JJ, et al. Identification and characterization of essential genes in the human genome. Science. 2015 Nov 27;350(6264):1096–101.

157. ualcan [Internet]. [cited 2023 Jan 20]. Available from: http://ualcan.path.uab.edu/

158. gepia [Internet]. [cited 2023 Jan 20]. Available from: http://gepia.cancer-pku.cn/veri

159. Tang Z, Li C, Kang B, Gao G, Li C, Zhang Z. GEPIA: a web server for cancer and normal gene expression profiling and interactive analyses. Nucleic Acids Res. 2017 Jul 3;45(W1):W98–102.

160. Sanjana NE, Shalem O, Zhang F. Improved vectors and genome-wide libraries for CRISPR screening. Nat Methods. 2014 Aug;11(8):783–4.

161. Park RJ, Wang T, Koundakjian D, Hultquist JF, Lamothe-Molina P, Monel B, et al. A genome-wide CRISPR screen identifies a restricted set of HIV host dependency factors. Nat Genet. 2017 Feb;49(2):193–203.

162. Senturk S, Mumcuoglu M, Gursoy-Yuzugullu O, Cingoz B, Akcali KC, Ozturk M. Transforming growth factor-beta induces senescence in hepatocellular carcinoma cells and inhibits tumor growth. Hepatology. 2010 Sep;52(3):966–74.

163. Demirci D, Dayanc B, Mazi FA, Senturk S. The Jekyll and Hyde of Cellular Senescence in Cancer. Cells. 2021 Jan 21;10(2):208.

164. Ke Y, Reddel RR, Gerwin BI, Reddel HK, Somers AN, McMenamin MG, et al. Establishment of a human in vitro mesothelial cell model system for investigating mechanisms of asbestos-induced mesothelioma. Am J Pathol. 1989 May;134(5):979–91.

165. Qie S, Diehl JA. Cyclin D1, cancer progression, and opportunities in cancer treatment. J Mol Med (Berl). 2016 Dec;94(12):1313–26.

166. Chen Z, Yao N, Zhang S, Song Y, Shao Q, Gu H, et al. Identification of critical radioresistance genes in esophageal squamous cell carcinoma by whole-exome sequencing. Ann Transl Med. 2020 Aug;8(16):998.

167. Jin H, Wang L, Wu Z, Lu X, Fan L, Gu D, et al. Functional Evaluation and Mechanism Study of Sting Inhibitor H-151 in Diffuse Large B-Cell Lymphoma. Blood. 2021 Nov 5;138(Supplement 1):2946–2946.

168. Rivero-Ríos P, Weisman LS. Roles of PIKfyve in multiple cellular pathways. Curr Opin Cell Biol. 2022 Jun;76:102086.

169. Shisheva A. PIKfyve and its Lipid products in health and in sickness. Curr Top Microbiol Immunol. 2012;362:127–62.

170. Hou JZ, Xi ZQ, Niu J, Li W, Wang X, Liang C, et al. Inhibition of PIKfyve using YM201636 suppresses the growth of liver cancer via the induction of autophagy. Oncol Rep. 2019 Mar;41(3):1971–9.

171. DoĞan E, DÜzgÜn Z, Yildirim Z, Özdİl B, AktuĞ H, Bozok ÇetİntaŞ V. The effects of PIKfyve inhibitor YM201636 on claudins and malignancy potential of nonsmall cell cancer cells. Turk J Biol. 2021;45(1):26–34.

172. Shoemaker CJ, Huang TQ, Weir NR, Polyakov NJ, Schultz SW, Denic V. CRISPR screening using an expanded toolkit of autophagy reporters identifies TMEM41B as a novel autophagy factor. PLoS Biol. 2019 Apr;17(4):e2007044.

173. Chun Y, Kim J. Autophagy: An Essential Degradation Program for Cellular Homeostasis and Life. Cells. 2018 Dec 19;7(12):278.

174. Nunes J, Zhang H, Angelopoulos N, Chhetri J, Osipo C, Grothey A, et al. ATG9A loss confers resistance to trastuzumab via c-Cbl mediated Her2 degradation. Oncotarget. 2016 May 10;7(19):27599–612.

175. Tang JY, Hsi E, Huang YC, Hsu NCH, Chen YK, Chu PY, et al. ATG9A overexpression is associated with disease recurrence and poor survival in patients with oral squamous cell carcinoma. Virchows Arch. 2013 Dec;463(6):737–42.

176. Claude-Taupin A, Fonderflick L, Gauthier T, Mansi L, Pallandre JR, Borg C, et al. ATG9A Is Overexpressed in Triple Negative Breast Cancer and Its In Vitro Extinction Leads to the Inhibition of Pro-Cancer Phenotypes. Cells. 2018 Dec 6;7(12):248.

177. Takahashi Y, Liang X, Hattori T, Tang Z, He H, Chen H, et al. VPS37A directs ESCRT recruitment for phagophore closure. J Cell Biol. 2019 Oct 7;218(10):3336–54.

178. Chen F, Zhang L, Wu J, Huo F, Ren X, Zheng J, et al. HCRP-1 regulates EGFR-AKTBIM-mediated anoikis resistance and serves as a prognostic marker in human colon cancer. Cell Death Dis. 2018 Dec 5;9(12):1176.

179. Du Y, Wang P, Sun H, Yang J, Lang X, Wang Z, et al. HCRP1 is downregulated in nonsmall cell lung cancer and regulates proliferation, invasion, and drug resistance. Tumour Biol. 2016 Oct 13;

180. Xu H, Miao ZF, Wang ZN, Zhao TT, Xu YY, Song YX, et al. HCRP1 downregulation confers poor prognosis and induces chemoresistance through regulation of EGFR-AKT pathway in human gastric cancer. Virchows Arch. 2017 Dec;471(6):743–51.

181. Morita K, Hama Y, Izume T, Tamura N, Ueno T, Yamashita Y, et al. Genome-wide CRISPR screen identifies TMEM41B as a gene required for autophagosome formation. J Cell Biol. 2018 Nov 5;217(11):3817–28.

182. Moretti F, Bergman P, Dodgson S, Marcellin D, Claerr I, Goodwin JM, et al. TMEM41B is a novel regulator of autophagy and lipid mobilization. EMBO Rep. 2018 Sep;19(9):e45889.

183. Kaldis P, Aleem E. Cell cycle sibling rivalry: Cdc2 vs. Cdk2. Cell Cycle. 2005 Nov;4(11):1491–4.

184. Tadesse S, Anshabo AT, Portman N, Lim E, Tilley W, Caldon CE, et al. Targeting CDK2 in cancer: challenges and opportunities for therapy. Drug Discov Today. 2020 Feb;25(2):406–13.

185. Jeganathan K, Malureanu L, Baker DJ, Abraham SC, van Deursen JM. Bub1 mediates cell death in response to chromosome missegregation and acts to suppress spontaneous tumorigenesis. J Cell Biol. 2007 Oct 22;179(2):255–67.

186. Schliekelman M, Cowley DO, O'Quinn R, Oliver TG, Lu L, Salmon ED, et al. Impaired Bub1 function in vivo compromises tension-dependent checkpoint function leading to aneuploidy and tumorigenesis. Cancer Res. 2009 Jan 1;69(1):45–54.

187. Ricke RM, Jeganathan KB, van Deursen JM. Bub1 overexpression induces aneuploidy and tumor formation through Aurora B kinase hyperactivation. J Cell Biol. 2011 Jun 13;193(6):1049–64.

188. Long HP, Liu JQ, Yu YY, Qiao Q, Li G. PKMYT1 as a Potential Target to Improve the Radiosensitivity of Lung Adenocarcinoma. Front Genet. 2020;11:376.

189. Boettcher M, McManus MT. Choosing the Right Tool for the Job: RNAi, TALEN, or CRISPR. Mol Cell. 2015 May 21;58(4):575–85.

190. Morgens DW, Deans RM, Li A, Bassik MC. Systematic comparison of CRISPR/Cas9 and RNAi screens for essential genes. Nat Biotechnol. 2016 Jun;34(6):634–6.

8. APPENDIX

İZMİR BİYOTIP VE GENOM MERKEZİ
GİRİŞİMSEL OLMAYAN ARAŞTIRMALAR ETİK KURULU (İBG-GOEK)
KARARI

Toplantı Tarihi	: 24/01/2023	**Toplantı Günü**	: Salı
Toplantı Sayısı	: 1	**Toplantı Saati**	: 10:30

Sayın Doç. Dr. Şerif ŞENTÜRK,

2023-005 Protokol No'lu; sorumlusu olduğunuz "MALİGN PLEVRAL MEZOTELYOMA GELİŞİMİNDE ROL OYNAYAN ESANSİYEL GENLERİN CRISPR/CAS9 BAZLI NEGATİF SEÇİLİM TARAMA YÖNTEMİYLE TANIMLANMASI" başlıklı araştırmanın uygulanmasında etik açıdan sakınca olmadığına oy birliği ile karar verilmiştir.

Bilgilerinizi ve gereğini rica ederiz.

Prof. Dr. H. Alper BAĞRIYANIK **Başkan**	**Prof. Dr. Hilmi ORHAN** **Başkan Yardımcısı**
Prof. Dr. Sedef AKGÜNGÖR **Üye** (Katılmadı)	**Prof. Dr. Gülgün OKTAY** **Üye**
Dr. Serap ERKEK ÖZHAN **Üye** (Katılmadı)	**Prof. Dr. Şermin GENÇ** **Üye**
Doç. Dr. Canan Aslı YILDIRIM **Üye** (Katılmadı)	**Doç. Dr. Can KÜÇÜK** **Üye**
Dr. Öğr. Üyesi Yavuz OKTAY **Üye**	

İZMİR BİYOTIP VE GENOM MERKEZİ
HAYVAN DENEYLERİ YEREL ETİK KURULU (İBG-HADYEK)
KARARI

Toplantı Tarihi	: 13/04/2022	**Toplantı Günü**	: Çarşamba
Toplantı Sayısı	: 6	**Toplantı Saati**	: 15:30

Sayın Doç. Dr. Şerif ŞENTÜRK,

2022-015 Protokol No'lu; yürütücüsü olduğunuz "Malign Plevral Mezotelyoma'da BUB1 Geninin Moleküler Rolünün Araştırılması" başlıklı projenin uygulanmasında etik açıdan sakınca olmadığına oy birliği ile karar verilmiştir.

Bilgilerinizi ve gereğini rica ederiz.

Dr. Gülçin ÇAKAN AKDOĞAN **Başkan**	**Vet. Hek. Kerem ESMEN** **Başkan Yardımcısı**
Prof. Dr. Ensari GÜNELİ **Üye**	**Doç. Dr. Güneş ÖZHAN** **Üye**
Doç. Dr. Kasım DİRİL **Üye**	**Dr. Yavuz DOĞAN** **Üye**
Vet. Hek. Umur KELEŞ **Üye**	**Vet. Hek. Ceren ÜLKER** **Üye**
Vet. Hek. Gizem ARALAN **Üye**	**İrem KARADAŞ** **Üye**



ECE ÇAKIROĞLU

Personal Information

Contact Information

Contact Address	İzmir Biyotıp Ve Genom Merkezi, Dokuz Eylül Üniversitesi İnciraltı Yerleşkesi
Telephone	
Email	
Web Page	

Education Information

15 February 2017 - Now (6 Year 1 Month)
Doktora, Doktora, DOKUZ EYLÜL ÜNİVERSİTESİ, TÜRKİYE
İZMİR ULUSLARARASI BİYOTIP VE GENOM ENSTİTÜSÜ, MOLEKÜLER BİYOLOJİ VE GENETİK (DR) (İNGİLİZCE)
Diploma Number: -
Cumulative Grade Point Average: 3.17 / 4.0

11 February 2014 - 11 January 2017 (3 Year)
Yüksek Lisans, Tezli Program, DOKUZ EYLÜL ÜNİVERSİTESİ, TÜRKİYE
SAĞLIK BİLİMLERİ ENSTİTÜSÜ, TEMEL ONKOLOJİ (YL) (TEZLİ)
Diploma Number: 201700121
Cumulative Grade Point Average: 3.59 / 4.0

01 September 2009 - 13 September 2013 (4 Year 1 Month)
Lisans, Anadal/Normal Öğretim, EGE ÜNİVERSİTESİ, TÜRKİYE
BİYOLOJİ BÖLÜMÜ, BİYOLOJİ PR.
Diploma Number: 2012/04/0761
Cumulative Grade Point Average: 2.6 / 4.0

Foreign Language Information

İNGİLİZCE (Reading: İyi, Writing: İyi, Speaking: İyi)

Scientific Technological Activity Fields

Keywords

Mezotelyoma

CRISPR

Moleküler Kanser Biyolojisi

R&D Competency

Books

Z. S. AMEEN, E. ÇAKIROĞLU, Ş. ŞENTÜRK, A. U. IBRAHHİM & M. ÖZSÖZ, CRISPR/Cas9 Gene Editing in Mammalian Cells Using LentiCRISPRv2/LentiGuide-Puro Vectors, K. A. MOLLA & M. T. ISLAM [Editors], CRISPR-Cas Methods(281 - 299), ISBN: 978-1-0716-1656-7: Springer Protocols, 31 July 2021, Kitapta

Bölüm.

Articles

P. Y. GÜNERİ SÖZERİ, G. ÖZDEN YILMAZ, A. KISIM, E. ÇAKIROĞLU, A. ERAY, H. UZUNER, G. KARAKÜLAH, D. PESEN OKVUR, Ş. ŞENTÜRK & S. ERKEK ÖZHAN, FLI1 and FRA1 transcription factors drive the transcriptional regulatory networks characterizing muscle invasive bladder cancer, Communications Biology, 2023, 2399-3642, 6, 199, 1.

F. A. MAZI, E. ÇAKIROĞLU, M. UYSAL, M. KALYONCU, D. DEMİRCİ, P. Y. GÜNERİ SÖZERİ, G. ÖZDEN YILMAZ, S. ERKEK ÖZHAN & Ş. ŞENTÜRK, The paracaspase MALT1 is a downstream target of Smad3 and potentiates the crosstalk between TGF-ß and NF-kB signaling pathways in cancer cells, Cellular signalling, 2023, 0898-6568, 105, 110611, 1.

E. CAKİROGLU & S. SENTURK, Genomics and Functional Genomics of Malignant Pleural Mesothelioma, INTERNATIONAL JOURNAL OF MOLECULAR SCIENCES, 2020, 1422-0067, 21, 17.

E. ÇAKIROĞLU, T. UYSAL, G. ÇALIBAŞI KOÇAL, F. AYGENLİ, G. BARAN & Y. BAŞBINAR, The Role of Morus Nigra Extract and Its Active Compounds as Drug Candidate on Human Colorectal Adenocarcinoma Cell Line HT-29, International Journal of Clinical Oncology and Cancer Research, 2017, 2578-9511, 2, 1, 10-14.

G. ÇALIBAŞI KOÇAL, A. AMİRFALLAH, Y. K. DAĞDEVİREN, M. AKBARPOUR, T. UYSAL, E. ÇAKIROĞLU, Y. BAŞBINAR & H. ELLİDOKUZ, İnciraltı Kampüsünde Biyoistatistik ve Biyoinformatik Program Kullanım Sıklığı ve Farkındalığı, Dokuz Eylül Üniversitesi Tıp Fakültesi Dergisi, 2014, 1300-6622, 28, 2, 45-50.

Conference Papers

M. UYSAL, E. ÇAKIROĞLU, Ö. TUTCU, Ö. MUTLU & Ş. ŞENTÜRK, ATG9A Gene is Required for the Survival of Malignant Pleural Mesthelioma Cells, Poster Sunumu, TBS International Biochemistry Congress 2022 - 33rd National Biochemistry Congress, 26 October 2022, 30 October 2022.

M. Z. GÜNGÖR, E. ÇAKIROĞLU, B. AKDEMİR & Ş. ŞENTÜRK, The Molecular Role of RUVBL1 Gene on Cancer Cell Phenotypes in Malignant Pleural Mesothelioma, Poster Sunumu, TBS International Biochemistry Congress 2022 - 33rd National Biochemistry Congress, 26 October 2022, 30 October 2022.

B. ULUATA DAYANÇ, S. ERİŞ, E. ÇAKIROĞLU, F. A. MAZI, Ö. Ş. COŞKUN, D. DEMİRCİ, G. KARAKÜLAH & Ş. ŞENTÜRK, Investigating Partners in Crime: Osimertinib Resistance Mechanisms in Non-small Cell Lung Cancer Using Focused CRISPR Screen, Poster Sunumu, IASLC 2022 WCLC World Conference on Lung Cancer, 06 August 2022, 09 August 2022.

E. ÇAKIROĞLU, Ş. ŞENTÜRK & G. KARAKÜLAH, Genome-wide CRISPR screen identifies BUB1 as a cancer-dependency gene in malignant pleural mesothelioma, Özet Bildiri, IUBMB-FEBS-PABMB 2022 Congress (The Biochemistry Global Summit), 09 July 2022, 14 July 2022.

G. KOÇAK, E. ÇAKIROĞLU, C. A. YILDIRIM, Ş. ŞENTÜRK & S. GÜVEN, Role of Autophagy on Differentiation of Corneal Endothelial Cells from hiPSCs, Poster Sunumu, 8th International Congress of the Molecular Biology Association of Turkey, 09 June 2022, 12 June 2022.

E. BULUT ATALAY, E. ÇAKIROĞLU, Ş. ŞENTÜRK & H. AYAR KAYALI, Generation of cell models using CRISPR/Cas9-based gene therapy to study molecular functions of IDH in colorectal cancer, Özet Bildiri, BioTürkiye Uluslararası Biyoteknoloji Kongresi, 09 September 2021, 11 September 2021.

E. ÇAKIROĞLU, Ö. Ş. COŞKUN, G. KARAKÜLAH & Ş. ŞENTÜRK, Identification of Essential Genes in Malignant Pleural Mesothelioma Using Genome-Wide CRISPR/Cas9-Based Negative Selection Screen, Poster Sunumu, IASLC 2020

World Conference on Lung Cancer, 28 January 2021, 31 January 2021.

A. KURDEN PEKMEZCİ, Ö. Ş. COŞKUN, E. ÇAKIROĞLU, D. DEMİRCİ & Ş. ŞENTÜRK, Hepatoselüler karsinom hücre hatlarında Malt1 tükenmesinin büyüme baskılayıcı etkilerinin arastırılması, Özet Bildiri, Onkolojide İz Bırakanlar Zirvesi, 14 November 2019, 17 November 2019.

E. ÇAKIROĞLU, Ö. Ş. COŞKUN, A. KURDEN PEKMEZCİ & Ş. ŞENTÜRK, MALIGN PLEVRAL MEZOTELYOMA TÜMÖROGENEZ MEKANIZMALARININ CRISPR-CAS9 TARAMA ILE ARAŞTIRILMASI, Özet Bildiri, Onkolojide İz Bırakanlar Zirvesi, 14 November 2019, 17 November 2019.

F. A. MAZI, E. ÇAKIROĞLU, A. KURDEN PEKMEZCİ, D. DEMİRCİ & Ş. ŞENTÜRK, TGF-ß'ya baglı kanser hücre sekretomunun regülasyonunda Malt1'ın rolü, Özet Bildiri, Onkolojide Iz Bırakanlar Zirvesi, 14 November 2019, 17 November 2019.

E. ÇAKIROĞLU, Ö. Ş. COŞKUN & Ş. ŞENTÜRK, Genome-Wide CRISPR-Cas9 Screening for Identification of Cancer Essential Genes in Malignant Pleural Mesothelioma, Sözlü Sunum, XXVII. BALKAN CLINICAL LABORATORY FEDERATION MEETING BCLF 2019 and XXX. NATIONAL CONGRESS OF THE TURKISH BIOCHEMICAL SOCIETY TBS 2019, 27 October 2019, 31 October 2019, 41 - 41.

E. ÇAKIROĞLU, Ö. DUMRAL, Ö. Ş. COŞKUN & Ş. ŞENTÜRK, Engineering and Functional Validation of Clonal Cell Lines with Stable Cas9 Expression for Genome-Wide CRISPR Screen in Malignant Pleural Mesothelioma, Poster Sunumu, 6th International Congress of the Molecular Biology Association of Turkey, 05 September 2018, 08 September 2018, 140 - 140.

G. GENÇOĞLAN, E. ÇAKIROĞLU, G. ÇALIBAŞI KOÇAL, H. S. VATANSEVER & Y. BAŞBINAR, Malign Melanom Hücre Dizilerinde BRAF İnhibitörü Direncinin HIF-1 Regulasyonu ile İlişkisinin Araştrlması, Poster Sunumu, 22. Ulusal Kanser Kongresi, 19 April 2017, 23 April 2017, 217 - 217.

T. UYSAL, E. ÇAKIROĞLU, G. ÇALIBAŞI KOÇAL & Y. BAŞBINAR, 2D ve 3D Ko-Kültür Modelinde Hücreler Aras "Cross-Talk", Sözlü Sunum, 3nd International Medical Congress for Student and Young Doctors, 01 November 2016, 02 November 2016.

Y. BAŞBINAR, E. ÇAKIROĞLU, O. Ü. ÜNAL, Y. K. DAĞDEVİREN, T. UYSAL, G. ÇALIBAŞI KOÇAL, S. N. KAZAZ, H. ELLİDOKUZ & İ. ÖZTOP, EGFR mutation status is associated with clinicopathological features in Turkey elderly, female, never smokers with NSCLC, Poster Sunumu, 41st FEBS Congress on Molecular and Systems Biology for a Better Life, 03 September 2016, 08 September 2016.

TÜBİTAK Scholarships and Fundings

Project Info

214S334, Fiziksel Mikroçevrenin Bir Bileşeni Olarak Peritoneal Doğal Sıvı Akışının Over Kanserinin Periton Metastazındaki Rolü Ve Moleküler Mekanizması, Uluslararası, Burslu, Sonuçlandı, ARDEB, SBAG - Sağlık Bilimleri Araştırma Destek

Grubu, Project Participation/Leave Dates: 11/1/15 - 9/30/16, Project Start/End Dates: 5/1/15 - 5/1/18.
117Z227, Malign Plevral Mezotelyoma Gelişiminde Rol Oynayan Esansiyel Genlerin ve Hücresel Yolakların CRISPR/Cas9 Güdümlü Tüm Genom Negatif Seçilim Tarama Yöntemiyle Sistematik Olarak Sorgulanması, Aydınlatılması ve Moleküler Karakterizasyonu, 3501 - Kariyer, Burslu, Sonuçlandı, ARDEB, KBAG - Kimya Biyoloji Araştırma Destek Grubu, Project Participation/Leave Dates: 9/12/19 - 10/1/20, Project Start/End Dates: 10/1/17 - 10/1/20.

BIDEB Supports

ECE ÇAKIROĞLU, Etkinlik Destekleri ve Eğitim Bursları Müdürlüğü, 2224-A Yurt Dışı Bilimsel Etkinliklere Katılma Desteği Programı, Destekleniyor, 2022 - 2, 7/8/22 - 7/13/22.
ECE ÇAKIROĞLU, Etkinlik Destekleri ve Eğitim Bursları Müdürlüğü, 2211-C Öncelikli Alanlara Yönelik Yurt İçi Doktora Burs Programı, Destekleniyor, 2020 - 1, 3/1/20 - 2/28/23.

Number of Panelist/Observer/Reporter Jobs

Refereeing/Panelist/Outer Consultant Count	ARDEB/BİDEB 0	TEYDEB 0	Total 0
Number of Observer/Consultant Jobs	ARDEB/BİDEB 0	TEYDEB 0	Total 0
Number of Reporter Jobs	ARDEB/BİDEB 0	TEYDEB 0	Total 0